3193 75 ②

Lawrence
Livermore
National
Laboratory

INERTIAL CONFINEMENT FUSION

ICF Quarterly Report

April–June 1993
Volume 3, Number 3

Development of Large Aperture KDP Crystals

Inner-Shell Photo-Ionized X-Ray Lasers

X-Ray Radiographic Measurements in Solid Density Materials

Nodule Defects in Multilayer Coatings

Nova Equation-of-State Measurements

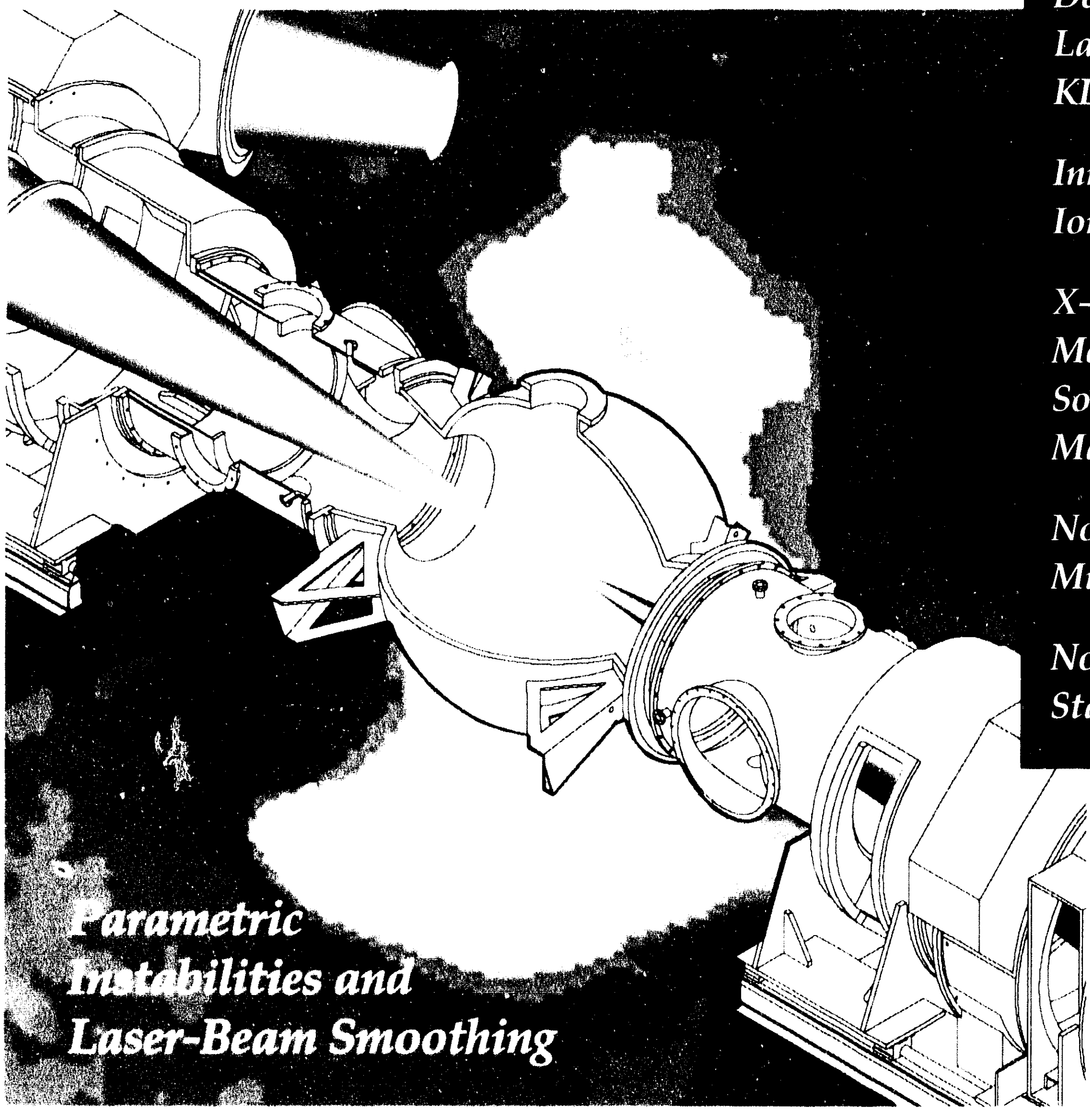

Parametric Instabilities and Laser-Beam Smoothing

UCRL-LR-105821-93-3

The *ICF Quarterly Report* is published four times each fiscal year by the Inertial Confinement Fusion Program at the Lawrence Livermore National Laboratory. The journal reports selected current research within the ICF Program. Major areas of investigation presented here include fusion target theory and design, target fabrication, target experiments, and laser and optical science and technology. Questions and comments relating to the technical content of the journal should be addressed to the ICF Program Office, Lawrence Livermore National Laboratory, P.O. Box 5508, Livermore, CA 94551.

The Cover: A schematic of the Nova Two Beam Target Chamber configured for laser-plasma interaction experiments is described in the article, "Parametric Instabilities and Laser-Beam Smoothing," page 137. The schematic is shown superimposed on a sample laser light spectrum recorded by the backscattering diagnostic station. This laser light is backscattered when one of the beams is incident on a large scalelength plasma. The plasma is produced by the opposite beam and mimics many of the characteristics of the plasmas surrounding ICF target capsules.

UCRL-LR-105821-93-3
Distribution Category UC-712
April - June 1993

Printed in the United States of America
Available from
National Technical Information Service
U.S. Department of Commerce
5285 Port Royal Road
Springfield, Virginia 22161
Price codes: printed copy A03, microfiche A01.

Work performed under the auspices of the U.S. Department of Energy by Lawrence Livermore National Laboratory under Contract W-7405-Eng-48.

INERTIAL CONFINEMENT FUSION

Quarterly Report

April – June 1993
Volume 3, Number 3

In this issue:

Foreword iii

Development of Large-Aperture KDP Crystals 103

We describe developments in the growth of large crystals to be used for frequency conversion and polarization control on the planned National Ignition Facility (NIF). Our plan is to meet the NIF cost and quality goals through the increased speed of crystal growth and better control of imperfections and strain in the crystals.

Inner-Shell Photo-Ionized X-Ray Lasers 112

This article describes the generation of population inversion and gain in materials pumped through photo-ionization by a short, intense burst of x rays. The short x-ray pulse is produced using a 100-fs duration laser to irradiate a neighboring high-Z target. This technique has the potential to allow x-ray lasers in the wavelength range 5–15 Å to be demonstrated.

X-Ray Radiographic Measurements of Radiation-Driven Shock and Interface Motion in Solid Density Materials 117

The first measurements of the propagation of radiation driven shock waves through solid density materials are described. These measurements were made as part of our continuing studies of hydrodynamic shock propagation, interface motion, and material mix in ICF implosions.

The Role of Nodule Defects in Laser-Induced Damage of Multilayer Optical Coatings 123

For high peak-power lasers, the system architecture and output fluence are dependent on the damage thresholds of multilayer dielectric-coated mirrors and polarizers. This article describes our continuing investigation of laser damage processes in such coatings using, for the first time, atomic force and scanning-probe microscopy to study localized defects in the coatings.

Techniques for Mbar to Near-Gbar Equation-of-State Measurements with the Nova Laser 131

Knowledge of the equation of state of a material at extremely high pressure is crucial to our understanding of the thermodynamics and hydrodynamics of a capsule target in the NIF. In this article, we describe our experiments to ascertain the equation of state from Hugoniot measurements. Using flyer foils driven by x-ray emission from Nova hohlraums, shock pressures of nearly 1 Gbar were observed.

Parametric Instabilities and Laser-Beam Smoothing 137

The long scalelength, low density plasma surrounding a fusion target provides ideal conditions for the growth of instabilities (stimulated Raman and Brillouin scattering, and filamentation). The resultant scattering of laser light by these instabilities can produce a significant loss of incident laser energy and, by modifying the light distribution around the target, can affect the symmetry of the implosion. We are studying the control of parametric instabilities through modification of the temporal and spatial coherence of the incident laser beams.

Facilities Report April–June 1993

Publications

Scientific Editor
Brian J. MacGowan

Editorial Staff
Marie Kotowski
Dabbie Schleich

Design Staff
Ellen L. Baldwin

Art Staff
TID Art Division

Foreword

This issue of the *ICF Quarterly* contains six articles describing recent advances in Lawrence Livermore National Laboratory's inertial confinement fusion (ICF) program. The current emphasis of the ICF program is in support of DOE's National Ignition Facility (NIF) initiative for demonstrating ignition and gain with a 1–2 MJ glass laser. The enclosed articles describe recent Nova experiments and investigations tailored towards enhancing our understanding of the key physics and technological issues for the NIF.

Two of the articles are devoted to improving the performance and affordability of optical components essential for the NIF. The article entitled "Development of Large Aperture KDP Crystals" describes developments in the growth of large crystals for frequency conversion and polarization control on the planned NIF. We plan to meet the cost and quality goals of the NIF frequency conversion requirements by increasing the speed of crystal growth and controlling imperfections and strain in the crystals. Imperfections and residual strain in the crystals affect laser performance by reducing the harmonic conversion efficiency and depolarizing the beam through stress induced birefringence. For high peak power lasers such as the NIF, the system architecture and output fluence are dependent on the damage thresholds of KDP conversion crystals and polarizers as well as multilayer dielectric coated mirrors and polarizers. The article "The Role of Nodule Defects in Laser-Induced Damage of Multilayer Optical Coatings" provides a summary of our continuing investigation of laser damage processes in such coatings, using, for the first time, atomic force and scanning-probe microscopy to study localized defects.

Two articles deal with shock wave propagation in plasmas. Knowledge of the equation of state of a material at extremely high pressure is crucial to our understanding of the thermodynamics and hydrodynamics of a capsule target. In "Techniques for Mbar to Near-Gbar Equation-of-State Measurements with the Nova Laser," elegant experiments are described which ascertain the equation of state from Hugoniot measurements. Using flyer foils driven by x-ray emission from Nova hohlraums, measured shock pressures of nearly 1 Gbar have been observed. The article "X-Ray Radiographic Measurements of Radiation-Driven Shock and Interface Motion in Solid Density Materials" presents the first measurements of the propagation of radiation driven shock waves through solid density materials.

The long scalelength, low density plasma surrounding a fusion target provides ideal conditions for the growth of instabilities (stimulated Raman and Brillouin scattering, and filamentation). The resultant scattering of laser light by such instabilities can produce a significant loss of incident laser energy and can modify the light distribution around the target affecting the symmetry of the implosion. Hence the study of parametric instabilities in laser plasmas is of vital importance for ICF. The article "Parametric Instabilities and Laser Beam Smoothing" describes our studies of the control of parametric instabilities through modification of the temporal and spatial coherence of the incident laser beams.

Finally the article "Inner-Shell Photo-Ionized X-Ray Lasers" describes a class of x-ray lasers that are pumped by the short pulse, high power lasers that have become available over the past few years. The authors present calculations of the generation of population inversion and gain in materials pumped through photo-ionization by a short, intense burst of x rays. The short x-ray pulse is produced using a 100-fs duration laser to irradiate a neighboring high-Z target. This technique has the potential to allow x-ray lasers in the wavelength range 5–15 Å to be demonstrated.

Brian J. MacGowan
Scientific Editor

DEVELOPMENT OF LARGE APERTURE KDP CRYSTALS

J. J. De Yoreo
J. Britten
R. Vital
K. Montgomery
N. P. Zaitseva
B. W. Woods
L. J. Atherton
C. A. Ebbers
Z. Rek

Introduction

We are pursuing an aggressive KDP development program to ensure the availability of KH_2PO_4 (KDP) and $K(D_xH_{1-x})_2PO_4$ (DKDP) crystals whose cost, size, and quality meet our goals for Nova's successor—the National Ignition Facility (NIF). To reduce costs without sacrificing performance, the KDP development plan will:

- optimize current technology,
- develop new technologies for fast growth and low D_2O (heavy water) use,
- reduce the level of strain in KDP crystals, and
- ensure that the damage threshold of KDP meets the NIF's requirements.

In this article, we describe the rationale, experimental plan, and results to date for the first three elements of this program. Our work on the fourth element, increasing the damage threshold of DKDP, will be described elsewhere.

DKDP crystals are widely used to control both the polarization and frequency of laser light through application of the first and second order electro-optic effects. DKDP crystals of extremely large cross section are required for ICF applications. This is because ICF lasers must be designed to deliver large amounts of power to a target while maintaining the intensity in the optical chain at a level that is below the damage threshold of the optics. The frequency conversion arrays on Nova, the world's largest laser, are constructed from 27 cm × 27 cm KDP crystals. The baseline design for the NIF incorporates 37 cm × 37 cm Pockels cell, doubler and tripler crystals.[1] Depending on the type of frequency conversion used in the NIF, the boules, which must be grown to yield crystals of this size, will be as large as 51 × 51 cm^2 in cross section and 110 cm in length, making them more than five times the size of the Nova boules.

In addition to size requirements for ICF applications, crystal quality is also important. Efficient operation of electro-optic devices, such as Pockels cells and frequency converters, requires crystals with a high degree of perfection. In particular, internal strains in the crystals generate spatial variations in the refractive index tensor through the stress-optic effect. The effect of refractive index variations is two-fold. Stress induced birefringence leads to beam depolarization while variations in the average refractive index generate distortions of the transmitted wavefront. Performance goals for the NIF laser require crystals with index variations of $<10^{-5}$ and anomalous birefringence of $<10^{-6}$.

Crystals that meet the size and performance specifications for the NIF can likely be grown using current commercial methods. However, the estimated cost of such crystals, with no further technological development, is three to four times the cost goal for the NIF. The cost of DKDP crystals is particularly high, exceeding that of even Pt and Au on a per gram basis. The primary contributions to the cost of DKDP are labor costs and heavy water lease and replacement costs. The high labor cost results from the slow growth rates (long growth cycles) required to obtain crystals that meet the performance requirements and the low yields of acceptable crystals. Because the major determining factor in yield is the level of internal strain, performance and cost are strongly linked through yield. The heavy water cost is almost entirely associated with the need to fill the growth tank with solution. The actual cost of the heavy water, which is incorporated into the crystal, is insignificant.

Current Growth Techniques

KDP crystals and their analogues grow with a pyramidal habit [Fig. 1(a)].[2] Growth occurs on both the prismatic faces {100} and the pyramidal faces {101}, and thus a cross section of the boule will, in general, contain eight growth sectors [Fig. 1(b)]. Because different bonds are exposed on the two types of faces, the segregation coefficient for impurities on the prismatic face differs from that on the pyramidal. As a result, the composition of the two sectors differs. This difference leads to a change in the refractive index across the pyramidal-prismatic boundary and introduces strain into the crystal. For this reason, growth on the {100} faces is considered undesirable and is easily inhibited either by the presence of impurities in the starting salt or by intentional doping with trivalent cations. Consequently, KDP growth is typically seeded with a z-cut plate (one cut perpendicular to the [001] direction) whose cross section is equal to that of the desired boule [Fig. 1(c)].

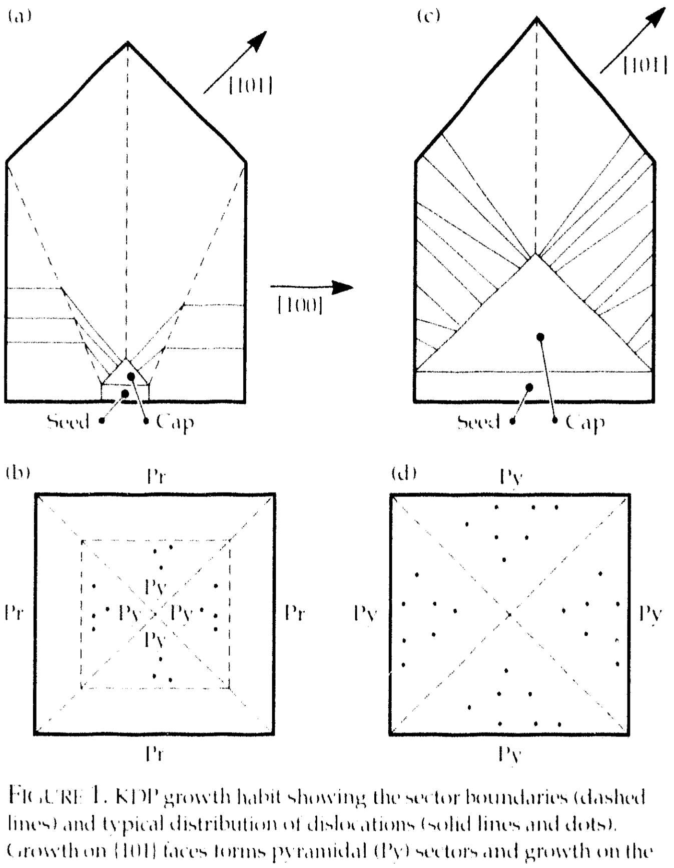

FIGURE 1. KDP growth habit showing the sector boundaries (dashed lines) and typical distribution of dislocations (solid lines and dots). Growth on {101} faces forms pyramidal (Py) sectors and growth on the {100} faces forms prismatic (Pr) sectors. (a) Boule grown from a small seed and exhibiting growth on all faces. (b) Cross section of an [001]- or z-plate cut from the crystal of (a) showing the eight growth sectors. (c) Boule grown from a full-size z-plate with no growth on the prismatic faces. (d) Cross section of a z-cut plate cut from the crystal of (c).

Growth then occurs primarily on the {101} faces leading to elongation along z and producing a crystal with only four growth sectors [Fig. 1(d)].

KDP crystals can be grown from an aqueous solution of KDP salt by either temperature drop or constant temperature methods:

- Temperature drop method—the temperature in a tank of KDP solution containing a seed crystal is lowered over time. Because the solubility of KDP in water decreases with decreasing temperature,[2] the solution becomes supersaturated and KDP precipitates out of solution causing the seed crystal to grow.
- Constant temperature method—the growth tank is maintained at constant temperature. A second tank, known as the saturator, containing water and undissolved KDP salt is held at a slightly higher temperature. The saturated solution from the saturator is fed to the cooler growth tank where it becomes supersaturated causing the seed crystal to grow.

The rate at which the crystal grows v_g is controlled by the degree of supersaturation σ, the temperature T, and the magnitude of the flow past the crystal. These quantities are related by:

$$v_g = f\sigma^n e^{-H/RT} \quad , \qquad (1)$$

where v_g is the growth rate of the crystal, f is a measure of the flow rate, H is an activation energy, R is the gas constant, and n is a number of order one. The supersaturation σ, is given by:

$$\sigma = \frac{C - C_e(T)}{C_e(T)} \quad , \qquad (2)$$

where C is the concentration of salt in the solution and $C_e(T)$ is the equilibrium solubility of the solution at T. In essence, σ provides the driving force for growth, T controls the surface kinetics, and f determines the rate at which solute is delivered to the crystal surface.

Increased growth rate can be achieved either by increasing flow until growth is kinetically limited or by increasing the supersaturation. However, as the supersaturation increases, the danger of generating extra crystals in the growth tank due to spontaneous nucleation also increases. These spurious crystals steal nutrient from the main crystal and can attach themselves to the main crystal causing strain and cracking. Consequently, to increase the growth rate we must focus on optimizing the flow and increasing the stability of the solution.

Crystal quality is synonymous with crystal uniformity. The degree to which ionic species are incorporated into the crystal is a function of temperature, flow rate, and supersaturation; therefore, variations in growth conditions will incorporate varying amounts of impurities and inhomogeneities in the deuterium concentration. These inhomogeneities will in turn generate spatial variations in the lattice parameters. As a result, the crystal becomes strained. Consequently, to increase crystal quality we must focus on maintaining constant growth conditions, particularly flow and supersaturation.

Improvements in Saturator Design and Operation

In our previous experiments, we used saturators, similar to those used in many standard crystallizers,[3] in constant-temperature, constant-supersaturation growth. These saturators consist of a vessel in which KDP salt rests in a bed at the bottom and liquid flows in and out of the clear space above the salt. In this configuration, replenishment of the solution is governed largely by inefficient diffusional transport from the salt bed. Replenishment is further hindered by the formation of a low-porosity crust that forms at the salt-bed/liquid interface. Thus, the concentration of KDP in solution leaving the saturator is typically less than that given by the equilibrium solubility at the saturator temperature, and it changes abruptly whenever fresh salt is added to the saturator. As a result, growth rates and their temporal stability are affected. We developed and fielded a slurry saturator, which provides intimate contact between crystallites and solution, and which is sized to ensure sufficient residence time and salt surface to maintain an accurate and constant concentration of dissolved solids. Such a system is vital to the successful extension of rapid growth techniques for temperature-drop crystallization to constant-temperature growth.

The slurry saturator (Fig. 2) is simply a vessel with an impeller placed at the bottom to agitate the salt bed. The solution is pumped from the top of a long thin tube that extends to the bottom of the vessel. The inside of the tube is protected from the turbulent flow in the vessel and serves as a clarifier to settle out salt particles that would become extra centers of growth in the crystallizer. The clarifier can reject crystallites down to a few micrometers in diameter, but colloidal suspended crystallites can remain in the outlet stream. The colloidal crystallites are dissolved by passing the outlet stream through a superheater downstream of the saturator. The supersaturated solution then passes through a 0.05 µm filter and a heat exchanger before entering the growth tank. The saturation loop is recharged from the growth tank by passive gravity feed.

Our slurry saturator, operated in batch mode, accurately measures solubility vs temperature of KDP salt and determines dissolution rates. We developed many time-temperature-concentration profiles by observing the change in dissolved salt concentration due to an abrupt temperature change. We measured the salt concentration by drying and weighing liquid aliquots taken at different time intervals. To do this, we raised and lowered the initial temperatures and examined the responses to any abrupt changes to a given final temperature. As a result, we verified that an equilibrium determined solely by temperature can be attained.

The saturator is essentially a continuous stirred tank reactor (CSTR). If a large excess of crystallite particles exists relative to the amount that is transferred to or from solution during a temperature change, the dissolution kinetics will be insensitive to that amount. The response of the dissolved solids fraction (X) in a CSTR to a change in temperature is given by:[4]

$$\frac{dX}{dt} = k\left[X - X_s(T)\right] \quad , \tag{3}$$

where k is a pseudo first-order rate constant including the dependence of the solid surface area and $X_s(T)$ is the temperature-dependent equilibrium solubility, which is a function of time in the above experiment. Figure 3 shows a typical concentration response curve for a case where the temperature was lowered from 33 to 30°C. If we adjust the above equation to fit this data then $k \approx 0.017\ \mathrm{s}^{-1}$. The same CSTR model written for the case of steady inflow and outflow is:

$$X_{\mathrm{out}} = \frac{X_{\mathrm{in}} + (kV/F)X_{\mathrm{sat}}}{1 + (kV/F)X_{\mathrm{sat}}} \tag{4}$$

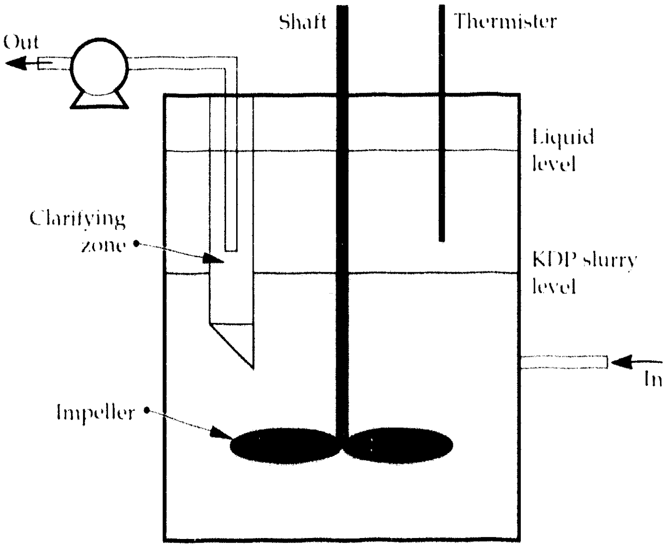

FIGURE 2. Schematic of the slurry saturator.

where X_{in} is the inlet mass fraction, and V and F are the saturator volume and volumetric flow rate, respectively. If $kV/F >> 1$, the outlet dissolved salt fraction becomes arbitrarily close to the saturation value, regardless of X_{in}.

Our experiments use a saturator volume of 8 l and a flow rate of 220 cc/min so that $kV/F \approx 35$, and thus the exit concentration is within 3% of equilibrium.

Experimental Crystallizer Designs

With present techniques and heavy water availability, up to 30% of the cost of DKDP plates for an NIF-sized order is in the leasing of heavy water. There are many options available for reducing the cost: (1) increasing the crystal growth rate and boule/plate yield to reduce the amount and/or time of the heavy water lease; (2) extending recently developed fast-growth methods for temperature-drop growth to constant-temperature, constant-supersaturation; and (3) reducing the specification for the deuteration level of the crystals to provide a straightforward cost reduction, at the possible expense of system performance.

We concentrated on developing crystallizer designs, which minimize the use of heavy water, by reducing the volume of the crystallizer. These designs also incorporate modifications, with varying degrees of associated risk, to improve mass transfer to the growing crystal surface. Figure 4 illustrates one crystallizer soon to be tested. This crystallizer is designed to grow boules with a cross section of 150 × 150 mm^2, and although it incorporates several untried design features, it is the most similar to classical constant-temperature crystallizers. It uses a saturator loop, based on the saturation system described previously. Another feature of this design is the cylindrical tube crystal holder with a diameter as large as the diagonal dimension of the crystal. This holder is retractable and can be raised to keep the point of the growing crystal in a constant vertical position to keep flow conditions constant as the crystal grows. The crystallizer uses a proven, adjustable cup seal around the shaft to isolate the growth tank from the external environment. When optimized for a full-scale crystallizer, the displacement volume of this shaft is sufficient to reduce the liquid-filled volume of the growth tank by as much as 60%. The experimental crystallizer (Fig. 4) is also fitted with a recirculating pumping loop in which a centrifugal immersion pump directs a stream through a nozzle near the tip of the growing crystal. This, along with reversible, variable-speed rotation of the crystal, provides the fluid movement necessary for effective mass transfer of solute to the growing crystal surface.

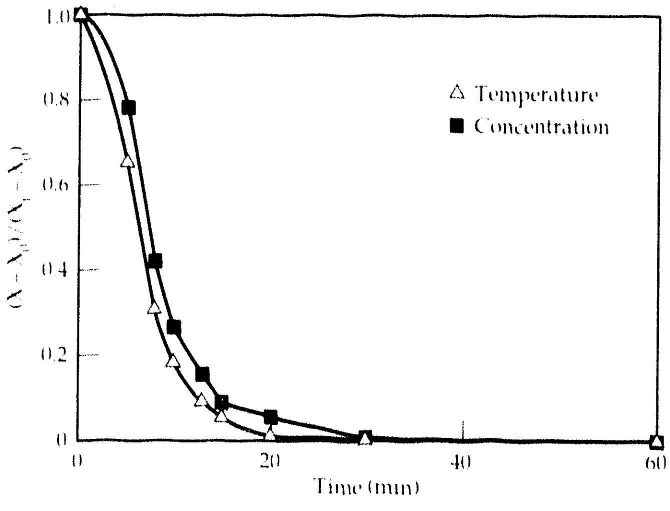

FIGURE 3. Change in KDP concentration and temperature over time following a change in the setpoint temperature from 33 to 30°C in a batch slurry saturator. X represents either temperature T, or concentration C. X_0 and X_f are the initial and final values of X, respectively. Fitting the response of the concentration to Eq. (1) gives a dissolution rate constant of 0.017 s^{-1}.

We also designed and recently tested a radically different conic downflow crystallizer to further reduce solution volume and to provide higher mass transfer rates near the crystal surface. Figure 5 is a schematic of this crystallizer (the saturation loop is the same as that described earlier). The crystallizer consists of a conical plenum that is captured by an o-ring seal inside a

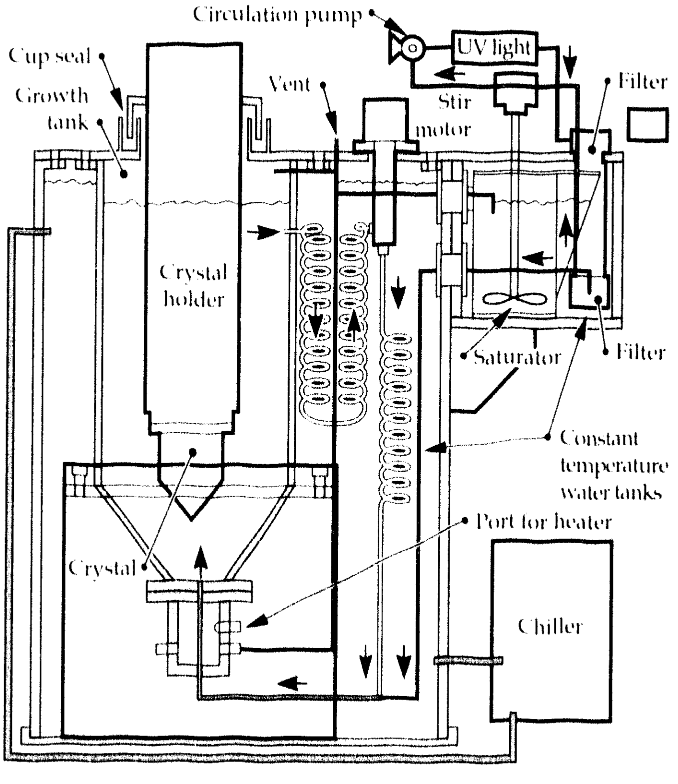

FIGURE 4. Schematic of the augmented flow, low-solution-capacity crystallizer for growing 150 × 150 mm^2 KDP boules.

cylindrical tube. The bottom edge of this cylindrical tube is cut at an angle that matches precisely with the angle of the tapered crystal holder. By adjusting the gap between the crystal holder and the tube end (nominally 0.5 mm), we controlled the leak rate of solution around the crystal, through the gap, and into the solution reservoir below. To recharge this leak rate, we pumped solution from this reservoir into the conical plenum (an overflow system maintains a constant liquid level in the plenum). Using this geometry, we minimized the fluid volume surrounding the crystallizer and maintained high fluid velocities very near the crystal surface. The solution volume therefore can be very small.

To test this concept, we grew a 100 × 100 × 30 mm^3 boule for 15 days from a z-cut plate in an existing tank (used for convenience and not optimized to reduce solution volume). During that time, the crystal grew at an average rate of 2 mm/day in the z-direction with no significant x-y growth. Several veils (light-scattering inclusions of solution) formed on the crystal edges due to the non-reversing rotation of the crystal holder. Otherwise, the crystal quality was sufficient to deem this first experiment a success. Our next experiment will provide a more accurate, repeatable, and reliable means of controlling the flow-regulating gap. To ensure the maintenance of the solution level around the crystal, we will place a level-detector in the plenum with a servo-controlled positioning system to adjust the gap.

Rapid Growth at High Supersaturations

Using conventional techniques, KDP crystals are grown at rates of about 1 mm/day. Recently, Zaitseva *et al.*[5,6] reported the growth by temperature drop of KDP and DKDP crystals at rates of 10 to 50 mm/day! What enabled them to achieve these phenomenal growth rates was the realization that KDP solutions are inherently stable against spontaneous crystallization up to relatively high supersaturations, provided the solution is properly prepared and all sources of spontaneous nucleation are removed from the crystallizer. Stabilization is achieved by first filtering the solution to remove foreign particles, which can serve as sources for heterogeneous nucleation, and then superheating the solution by tens of degrees above the saturation point to dissolve any small nuclei, which could cause homogeneous nucleation. Sources of nucleation within the tank are eliminated by avoiding sharp corners, pores, cold spots, regions with no flow (dead zones) and by hermetically sealing the tank during growth. Growth is also seeded with a small "point seed" rather than a full-sized plate [Fig. 1(a)]. This is necessary because at such high levels of supersaturation, impurities are ineffective in inhibiting growth on the prismatic faces. Consequently, a small seed is required to produce a boule with a useful aspect ratio.

We initiated a set of experiments to extend this growth technology to the growth of large-aperture, high-quality

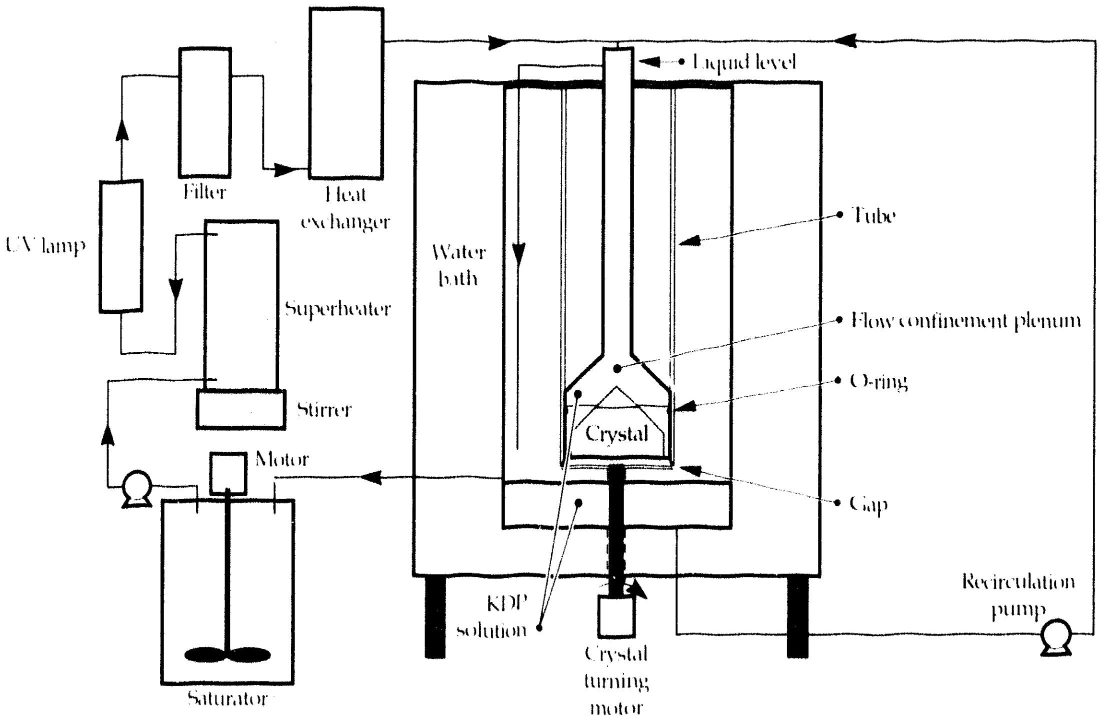

Figure 5. Schematic of the conic downflow crystallizer.

crystals. Figures 6(a) and (b) are photographs of KDP crystals being grown using this method. At the time of these photographs, the crystal in Fig. 6(a) had been growing for 8 days at 10 mm/day while the one in Fig. 6(b) had been growing for 2.5 days at 30 mm/day. Using conventional methods, a crystal of this size would require a growth time of about 2 months. The potential for cost savings with this technique is obvious. To realize those savings, over the next 12 months, we plan to: (1) determine the dependence of internal strain on growth rate; (2) develop a method for habit control; (3) scale the method to large size; and (4) incorporate the technique into a constant-temperature system using the saturator described earlier. Steps 1 and 2 are currently underway, and the equipment for steps 3 and 4 is being designed. Results thus far indicate that habit can be determined by controlling the dislocation structure of the capped seed, and that the level of strain in crystals grown at high-growth rates is similar to that in crystals grown conventionally.

Understanding the Source of Internal Strain

As discussed, internal strain in crystals generates spatial variations in the refractive index tensor through the stress-optic effect. This results in both anomalous birefringence and variations in the average refractive index. The detrimental effects of this strain on ICF laser performance are four-fold. (1) The stress induced birefringence in the Pockels cell crystals causes beam depolarization. Because the Pockels cell is used in conjunction with a polarizer, passage of the beam through the polarizer results in spatial variations in output intensity. This intensity modulation then grows through nonlinear absorptive processes in the downstream optics. Eventually, it can become sufficiently large to cause laser induced damage in the optics. (2) Anomalous birefringence in the frequency conversion crystals makes it impossible to meet the condition for phase matching at all positions in the crystal. This reduces the overall frequency conversion efficiency and produces further modulation of the beam intensity. (3) The distortions of the transmitted wavefront from the Pockels cell caused by variations in the average refractive index lead to energy losses at the downstream spatial filters. (4) Transmitted wavefront distortion from the harmonic generator crystals reduces frequency conversion efficiency and softens the focus of the beam at the target.

The level at which these effects are acceptable determines the specifications for crystal quality. Consequently, the laser performance requirements exert a strong influence on the yield of acceptable crystal plates from an as-grown boule and hence cost. To increase the yield and reduce the cost, we are working to understand the source of strain in KDP and its connection to optical degradation.

The Stress-Optic Effect in KDP

We have shown[7,8] that in (001) KDP and DKDP plates, internal strain induces a spatially varying change in the refractive index given by:

$$n' - n_0 = \Delta n \pm \frac{\delta n}{2} \quad , \tag{5}$$

where n_0 is the ordinary index, n' is the new index, Δn is the average shift in refractive index, and δn is the induced birefringence. The dependence of Δn and δn on the components of the strain tensor are given by:

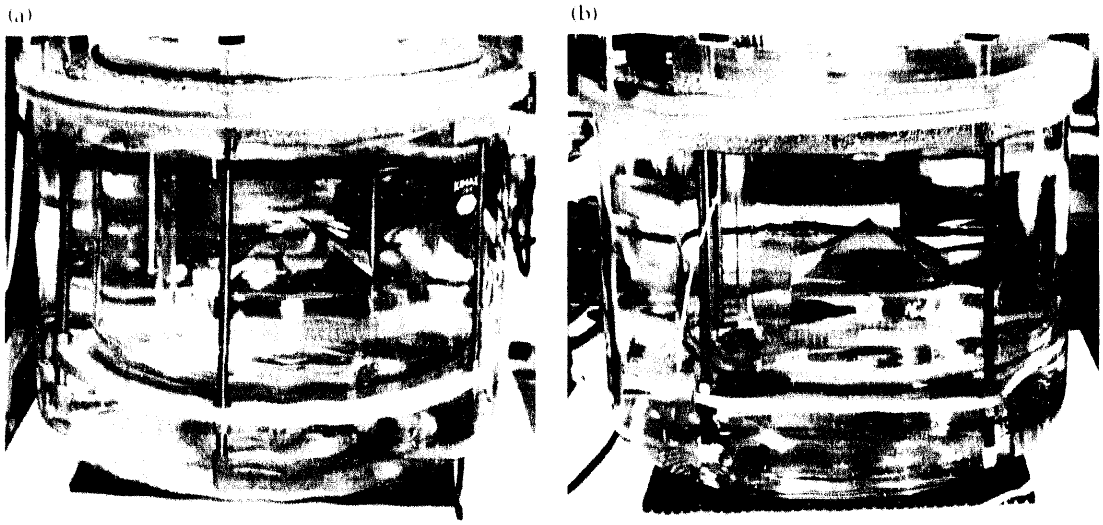

FIGURE 6. Two KDP crystals grown by recently developed rapid-growth techniques. At the time of the photographs, the crystal in (a) had been growing for 15 days at 5 mm/day, and the crystal in (b) had been growing for 2.5 days at 30 mm/day.

$$\Delta n = \frac{1}{2} n_o^3 \left[\frac{1}{2} (p_{11} + p_{12})(\varepsilon_x + \varepsilon_y) + p_{13}\varepsilon_z \right] \qquad (6)$$

and

$$\delta n = n_o^3 p_{66} \varepsilon_{xy} \quad , \qquad (7)$$

where the p_{ij}'s are the elasto-optic coefficients;[9] ε_x, ε_y, and ε_z are the normal stresses; and ε_{xy} is the shear strain in the xy plane of the crystal. The effect of the index shift Δn, is to generate a spatial variation of the phase Γ, given by:

$$\Gamma = \frac{2\pi}{\lambda} \Delta n l \quad , \qquad (8)$$

where l is the thickness of the crystal and λ is the wavelength of the laser.

The effect of the birefringence is to generate a depolarization loss L, given by:

$$L = \sin^2\left[(\pi/\lambda)\delta n l\right] \quad . \qquad (9)$$

Consequently, we can use measurements of the depolarization loss and transmitted phase front to determine the magnitude of the internal strain in the crystals.

Measurements of Optical Distortion

Using a circular polarimeter[8] and a phase stepping interferometer, we measured the depolarization loss and transmitted wavefront distortion in large numbers of KDP and DKDP crystals ranging in size from 5 × 5 × 1 cm^3 to 32 × 32 × 1 cm^3. Figure 7 shows the depolarization loss profiles in two 5 × 5 × 1 cm^3 crystals of $K(D_{0.98}H_{0.02})_2PO_4$ cut from the same boule. The crystal in Fig. 7(a) is a "first grown" crystal (97FG) cut from the region just above the seed cap while that of Fig. 7(b) is a "last grown" crystal (97LG) cut from the end of the boule. Figure 8 shows the transmitted wavefront profiles for the same crystals. The overall depolarization losses in the first and last grown crystals are 0.087% and 0.004%, respectively. The maximum losses are 1.0% in 97FG and 0.06% in the 97LG. The maximum loss in the first grown crystal corresponds to a birefringence of 3.2 ppm, a strain of 38 ppm, and a shear stress of 2.3 × 10^5 Pa. The transmitted wavefront data show that the index inhomogeneity varies from 17 ppm in the 97FG to about 6.4 ppm in 97LG. The corresponding normal strains are on the order of 10 ppm.

Although we observe a substantial variation in the level of strain from boule to boule, the above results are typical and show that the level of internal strain is much greater in first grown than in last grown crystals from a single boule. There are three possible sources of strain in these crystals:

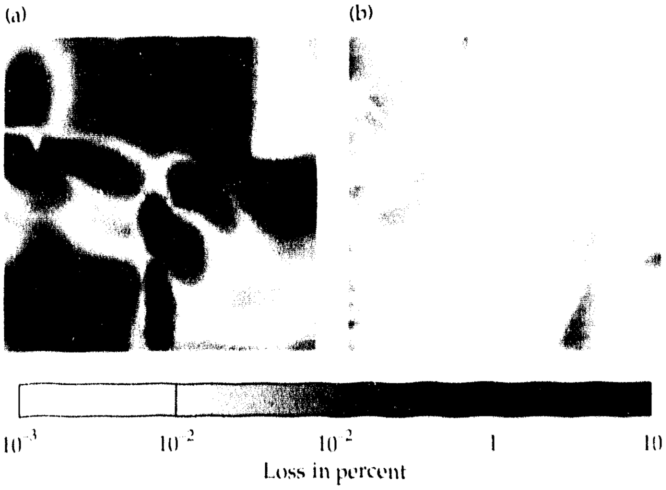

FIGURE 7. Depolarization loss in percent: (a) 97FG, a "first grown" crystal, was cut from just above the seed cap; (b) 97LG, a "last grown" crystal, was cut from the end of the boule.

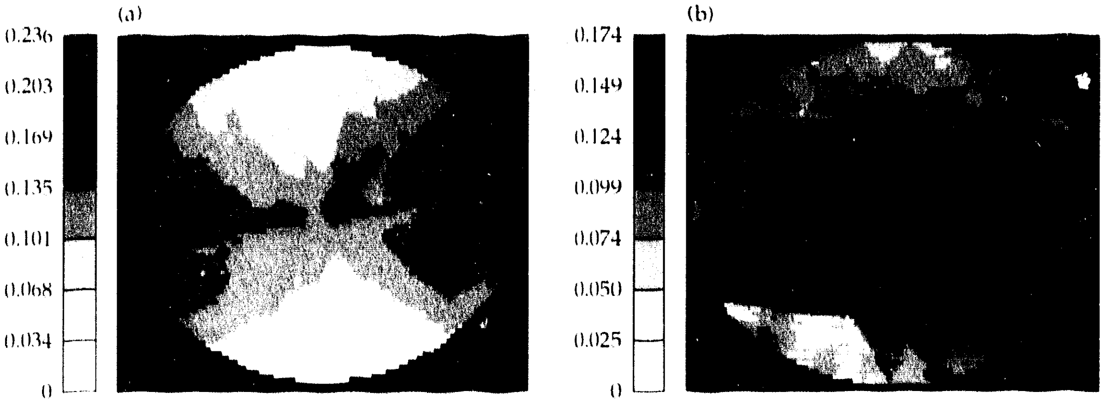

FIGURE 8. Transmitted wavefront in fractions of a wave from (a) 97FG and (b) 97LG of the same crystals as shown in Fig. 7.

1. Impurities can cause strain due to lattice mismatch. Belouet *et al.*[10] used x-ray topography and autoradiography to demonstrate that spatial variations in the concentration of trivalent cations at the 10 to 100 ppm level generates regions of strain and that the patterns of strain often reflect the growth habit of KDP.
2. The mixing of hydrogen and deuterium on the hydrogen sub-lattice will generate strain, due to the differences in the structural parameters of KH_2PO_4 and KD_2PO_4. Both the cell parameters and the orientation of the PO_4 tetrahedra are different for the two end members of this solid solution series,[11,12] consequently the mixed crystals will be strained. The change in the average orientation of the PO_4 tetrahedra within the xy-plane of the crystal with changes in deuteration is particularly large and reaches 0.5° in pure DKDP. A shear stress in the xy-plane will also result in such a rotation. Consequently, H-D mixing can create large shear strains and should be effective in generating depolarization losses. However, these losses will only be observable when the H distribution is correlated over distances that are comparable to the sampling volume of the laser.
3. Dislocations produce strain fields which vary as $1/r$ where r is the distance from the dislocation.[13] X-ray topographic studies[14,15] have shown that the majority of dislocations in KDP emanate from the seed cap, propagate at 90° to the pyramidal {101} faces of the growing crystal, and emerge from the crystal at the {100} faces [Fig. 1(d)]. Consequently, the dislocation density as well as the internal strain due to dislocations should decrease with distance from the seed.

X-Ray Topography

To identify the source of the strain that gives rise to the observed optical distortions, we performed x-ray topography using white-beam synchrotron radiation in reflection on fifteen $5 \times 5 \times 1$ cm^3 KDP and DKDP crystals. Our results revealed three common defects: regions dense in dislocations, a distribution of "domains," and regular banding in {100} growth sectors of rapidly grown crystals. (The growth bands have not been observed in conventionally grown crystals because they do not contain any prismatic sectors.) Figure 9 shows the topographs of 97FG and 97LG crystals. Crystal 97LG [Fig. 9(a)] is virtually dislocation free, but contains well-defined domains, polygonal regions whose lattice parameters and/or orientations differ from those of the rest of the crystal. They appear as dark regions on the topographs because they are not in diffraction simultaneously with the rest of the crystal. The characteristics of these domains are currently unknown but they are most likely a result of inhomogeneous impurity and/or H distributions. The location of the domains in 97LG corresponds to the regions of highest depolarization loss [Fig. 7(b)]. However, the magnitude of this loss is relatively small. Crystal 97FG [Fig. 9(b)] contains a few small domains but exhibits a large number of dislocations contained in five groups. Although not exact, there is a correlation between the location of these dislocation bunches and the lobes of high depolarization loss [Fig. 7(a)]. The transmitted wavefront profile for this crystal also reflects this distribution of dislocations but, once again, a one-to-one correspondence is not observed.

In the KDP and DKDP boules we examined, first-grown crystals were high in dislocation density but contained few domains; middle- and last-grown crystals contained few dislocations and numerous large domains. In each case, the domains appear to contribute only to moderate levels of strain while crystals high in dislocation density were always highly strained. While there is sometimes a strong correlation between the precise location of the dislocation bunches and the lobes of high depolarization loss, this correlation is often absent. We presume this is because: (1) The reflected x-rays originate in the upper 100 μm of the crystal while the optical profiles sample the entire thickness; and (2) The optical distortion is sensitive only to particular components of the stress field, which is a complicated function

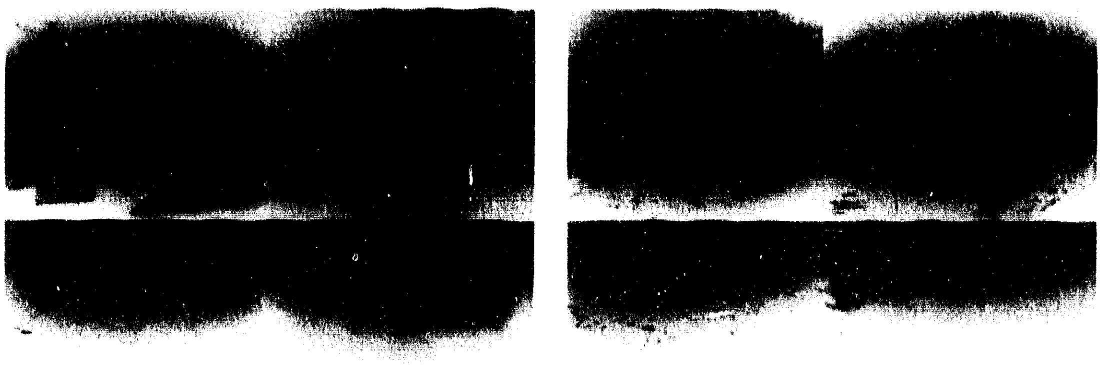
(a) (b)

Figure 9. X-ray topographs of (a) 97LG and (b) 97FG, for the same crystals as shown in Fig. 7. The topographs were collected in reflection using white-beam synchrotron radiation.

of dislocation density, dislocation type, and the Burgers vectors. However, we conclude that dislocations emanating from the seed cap are the main source of strain in KDP and DKDP plates. To reduce the level of strain, we must now focus on reducing the number of dislocations generated during the capping phase of growth.

Conclusions

The goal of our KDP development plan is to ensure the availability of large-aperture, high-quality KDP and DKDP crystals by advancing the technology of KDP growth. In the area of optimizing current techniques, we focused on improving saturator performance and flow in the growth tank and reducing the volume of heavy water needed for growth. These improvements aim at increasing growth rates while maintaining constant growth conditions and, therefore, crystal quality. The conical downflow crystallizer provides a more radical approach to reducing heavy water use but operates in a flow regime that differs substantially from that of conventional crystallizers. The rapid growth technique offers the greatest potential for cost reduction while maintaining or improving crystal quality. However, as yet, this technique has not been demonstrated at full scale and involves a great deal of technical risk associated with habit control and the danger of massive, spontaneous crystallization. In addition, this method has never been adapted to constant-temperature growth. Our future development activities are designed to address these technical issues.

Notes and References

1. LLNL ICF Program, *Nova Upgrade: A Proposed ICF Facility to Demonstrate Ignition and Gain*, Lawrence Livermore National Laboratory, Livermore, CA, UCRL-LR-106736, Rev. 1 (1992).
2. L. N. Rashkovich, *KDP-Family Single Crystals*, a review on KDP crystal growth (Adam Hilger, New York, 1991) pp. 202.
3. G. M. Loiacono, "Crystal growth of KH_2PO_4," *Ferroelectrics*, **71**, 49 (1987).
4. J. J. Carberry, *Chemical and Catalytic Reaction Engineering*, Ch. 3, (McGraw Hill, New York, 1976).
5. N. P. Zaitseva, I. L. Smol'skii, and L. N. Rashkovich, "Study of rapid growth of KDP crystals by temperature lowering," *Kristallografiya*, **36**, 198 (1988).
6. N. P. Zaitseva, F. Sh. Ganikhanov, O. V. Kaetchalov, V. F. Efimkov, S. A. Pastukhov, and V. B. Sobolev, "Optical properties of KDP crystals grown at high growth rates," in *Joint seminar on non-linear optics in control, diagnostics, and modeling of biophysical processes*, (SPIE—International Society for Optical Engineering, Bellingham, WA, 1990; *Proc. SPIE* **1402**) p. 223.
7. J. J. De Yoreo and B. W. Woods, "Investigation of strain birefringence and wavefront distortion in 001 plates of KD_2PO_4," in *Inorganic crystals for optics, electro-optics and frequency conversion*, (SPIE—International Society for Optical Engineering, Bellingham, WA, 1991; *Proc. SPIE*, **1561**) p. 50.
8. J. J. De Yoreo and B. W. Woods, "A study of residual stress and the stress-optic effect in mixed crystals $K(D_x H_{1-x})_2PO_4$," *J. Appl. Phys.*, **73**, 1 (1993).
9. J. F. Nye, *Physical Properties of Crystals*, Ch. 13, (Oxford University Press, New York, 1985).
10. C. Belouet, E. Dunia, and J. F. Petroff, "Autoradiography as a tool for studying iron segregation and related defects in KH_2PO_4 single crystals," *J. Cryst. Growth*, **29**, 109 (1975).
11. Z. Tun, R. J. Nelmes, W. F. Kubs, and R. F. D. Stansfield, "A high resolution neutron–diffraction study of the effects of deuteration on the crystal structure of KH_2PO_4," *J. Phys. C*, **21**, 245 (1988).
12. R. J. Nelmes, "Structural studies of KDP and the KDP–type transition by neutron and x-ray diffraction—1970–1985," *Ferroelectrics*, **71**, 87 (1987).
13. I. Kovacs and L. Zsoldos, *Dislocations and Plastic Deformation*, pp. 34–39, (Pergammon Press, New York, 1973).
14. C. Belouet, E. Dunia, and J. F. Petroff, "X-ray topographic study of defects in KH_2PO_4 single crystals and their relation with impurity segregation," *J. Cryst. Growth*, **23**, 243 (1974).
15. H Klapper, "Defects in non-metal crystals," in *Characterization of crystal growth defects by x-ray methods*, B. K. Tanner and D. K. Bowen, Eds., (Plenum Press, New York, 1980).

INNER-SHELL PHOTO-IONIZED X-RAY LASERS

D. C. Eder
G. L. Strobel
R. A. London
M. D. Rosen

Introduction

This report summarizes the processes that are important in calculating x-ray lasing pumped by inner-shell photo-ionization. Our discussion includes modeling of the high-Z plasma heated by a short-pulse high-intensity laser, and the spectrum of the resulting x rays that are produced. The calculated x-ray flux is used to pump a Ne gas to predict gain at an x-ray wavelength of 14.6 Å. In our conclusion, we suggest improvements in the modeling techniques and address requirements on the driving laser.

The collisional excitation approach to x-ray lasing, which was pioneered at LLNL, has been used to obtain lasing in the 35 to 500 Å wavelength regime.[1] Given sufficient pump energy, it may be possible to extend this approach down to 21.5 Å using Ni-like U. To achieve even shorter wavelengths, however, we must consider other pumping methods such as lasing following inner-shell photo-ionization. This lasing approach uses a high-intensity optical pulse with a rapid rise time to heat a plasma, which emits a large flux of x rays with a corresponding rapid rise time. With appropriate filtering, these x rays can be used to pump a population inversion in another medium. The x rays preferentially photo-ionize electrons from lower energy levels, leaving higher energy levels filled and hence producing a transient population inversion and laser gain. Recent advances in the required short-pulse high-intensity driving lasers have generated renewed interest[2,3] in this method, which has been around for a number of years.[4] Inner-shell lasing with wavelengths from 15 to 5 Å is possible using elements from Ne to Cl as the lasant material. For these elements, the population inversion is between two energy levels in the singly ionized atom. The upper-laser level corresponds to an electron hole in the inner K shell, and the lower-laser level corresponds to an electron missing from the outer L shell. The energy of the x rays required to inner-shell ionize these elements ranges from 870 eV for Ne to 2.8 keV for Cl.

Inner-shell lasing at very short wavelengths (15 to 5 Å) requires, as is the case for all lasers, a significant population in the upper-laser level and a small population in the lower-laser level. But, this places requirements on the driving laser and the fabrication of the target material: (1) Very rapid Auger decay is the dominant process that fills the inner-shell-electron hole. In this process, an outer-shell electron fills the hole with the extra energy being carried off by another outer electron that produces a doubly ionized ion. To maintain a significant population in the upper-laser level, the rate of inner-shell ionization must be comparable to this fast Auger decay. The ionizing x rays come from a nearby plasma, and the requirement of a large x-ray flux for ionization translates to a requirement of high intensity on the driving laser that heats that plasma. (2) It is also necessary to keep the population of the lower-laser state small. Since this state decays very slowly, this places a requirement on the rise time of the x rays that translates to a requirement on rise time of the driving laser pulse. Additionally, the lower-laser state can be populated directly by ionization through collisions with energetic photo and Auger electrons. To reduce this process, we introduce H into the lasant medium.

Inner-Shell Processes

Current x-ray lasing schemes use valence transitions of highly ionized atoms. For example, Ni-like Ta, with 45 electrons removed, has a lasing transition between the excited 4d to 4p levels with a wavelength of 44.8 Å. Alternatively, we can obtain short wavelengths in singly ionized atoms by using inner-shell transitions. However, the difficulty is that nonradiative processes (e.g., Auger decay) play an important role.

Figure 1 shows the important levels for inner-shell lasing in Ne and Mg. We used a hole notation where, for example, LL denotes a doubly ionized electronic structure with two holes in the L shell (principal quantum number 2). The energy of the K-hole to L-hole lasing transition is a large fraction of energy required to create the K hole giving the scheme a high quantum efficiency. The figure shows the Auger rates out of the upper-laser state of 363 and 492/ps, which greatly exceed the radiative rates to the lower-laser level of 6.7 and 16.3/ps for Ne and Mg, respectively. For Ne and Na, the lower-level decay rates are very slow, causing the laser to self terminate. For elements with two or more M-shell electrons (e.g., Mg) the lower-laser level can have an Auger decay. The rate for this Auger decay is always relatively slow compared to the K-shell Auger rate, but does exceed the radiative rate of the lasing transition for Si and higher Z elements. Self termination still occurs for higher Z elements, because collisional processes can populate the lower level faster than they can be emptied by Auger decay.

In addition to collisional population of the lower level, consider direct photo-ionization of an L-shell electron. This process directly populates the lower-laser level. For x rays with enough energy to ionize a K-shell electron, the cross section for L-shell ionization is approximately 10 times less than the K-shell cross section for the elements of interest. This means the majority of the photo-ionizations from these x rays will result in a K-shell hole. However, to keep L-shell ionization at an acceptable level, the majority of x rays with energies below the K edge must be removed by an appropriate filter (e.g., Be).

Compared to photo-resonant-line schemes, one advantage of photo-ionization is that it does not require the x rays to match the energy of a pumping transition. Figure 2 shows the K-shell cross sections for "even" Z atoms. The x rays only need energies greater than the K-shell edge, which allows for bands of emission to be used. The K-shell photo-ionization cross section decreases rapidly above the threshold energy, particularly for the lower Z elements, which limits the usefulness of a wide band of emission and places requirements on the energy and width of the radiation band. There are difficulties using higher Z atoms to extend the scheme to a short wavelength: (1) higher Z atoms have larger Auger rates out of the upper-laser level, (2) higher energy x rays are required with higher Z atoms, and (3) the photo-ionization cross section decreases for higher Z atoms.

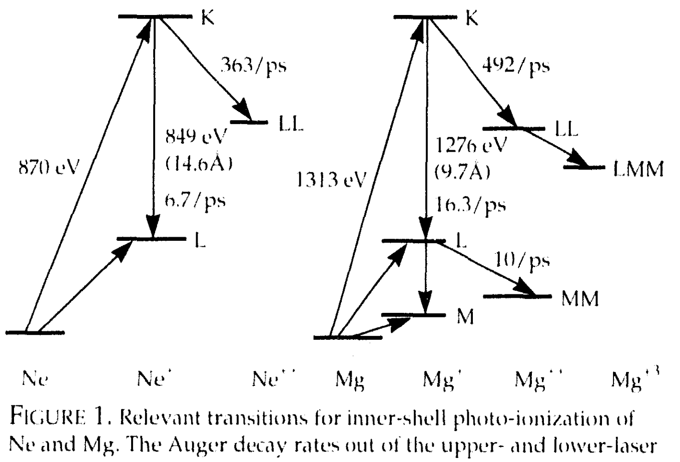

FIGURE 1. Relevant transitions for inner-shell photo-ionization of Ne and Mg. The Auger decay rates out of the upper- and lower-laser levels, the ionization, and lasing transition energies are given.

X-Ray Source Modeling

We have known for many years that high-Z material (e.g., Au) is an efficient source of x rays with important application in ICF and other areas. When short-pulse high-intensity lasers heat flat Au targets, the reflectivity increases (exceeding 90% for high intensities), resulting in poor coupling to the target.[5] When grooves are made in the target with depths of order 2000 Å and spacings are small compared to the wavelength, the reflectivity measures less than 20%, indicating good coupling.[5] Therefore, using grooved targets is one solution for heating the target effectively.

Figure 3 is a schematic of a complete x-ray laser target. As illustrated, the short-pulse high-intensity laser heats the grooved target to produce a short pulse of x rays. The optical laser is line focused onto the grooved target, with a width of 5 µm and a length of 1 to 3 cm. The low-Z filter (3-µm Be) absorbs the majority of the low-energy photons that could only ionize L-shell electrons. The thickness of the low-Z filter is comparable to the width of the line focus, which

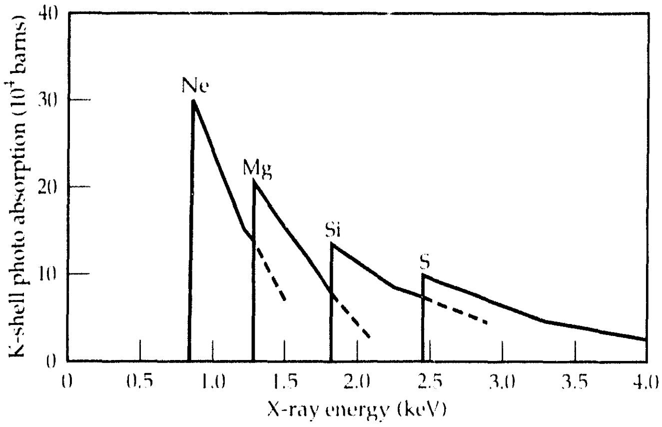

FIGURE 2. K-shell photo-absorption cross section energy dependence, for "even" Z atoms.

means that 2-D dilution effects must be included when calculating the x-ray flux that reaches the lasant material. The high-energy x rays that pass through the filter inner-shell ionize the lasant material. To reduce collisional ionization, we used H as a significant fraction of the lasant target (discussed later).

We modeled the grooved target using the hydrodynamic code LASNEX, as a collection of expanding planar foils. We assumed the energy associated with a laser intensity of 10^{17} W/cm^2 to be absorbed in a skin depth on each side of a 1000-Å Au foil. The duration (FWHM) of the optical pulse was taken to be 100 fs (1 fs = 10^{-15}s) with a Gaussian temporal profile. We found that shorter pulses do not significantly decrease the rise time of the required x rays. While intensities greater than 10^{17} W/cm^2 have been obtained with 100-fs pulses, the relatively large area in this line-focused geometry requires laser energies on the order of 5 to 15 J. These energies are approximately a factor of 10 greater than what is available from current laser drives, but should be available in the near future.

Figure 4(a) shows the calculated spectrum 100 fs after the peak of the optical pulse. In Fig. 4(b), we express the spectrum in terms of the temperature of a blackbody (T_{bb}) that radiates an equal amount of energy per unit area as the foil at each x-ray energy. There are two peaks in the emission corresponding to $n = 5$ to $n = 4$ transitions around 1 keV, and $n = 4$ to $n = 3$ transitions around 2.8 keV from various highly ionized stages of Au (e.g., Ni-like Au). The lower energy peak is appropriate for inner-shell ionization of Ne or Na, and the higher energy peak could be used for S or Cl lasants. We calculated the radiation using average-atom atomic physics with principal and angular-momentum quantum numbers. (When we used the simpler average-atom atomic model with only principal quantum numbers, the peaks were narrower and had higher peak values.[3]) The energy of these two bands of emission depends on the incident intensity; higher intensity gives more ionization and shifts the peaks to higher energies. The type of target material also changes the energy of the peaks, which allows you to obtain a band at the energy needed for a particular lasant by varying the Z of the pump material.

The rise time of the x rays is very important for inner-shell photo-ionized x-ray lasing. Figure 4(c) shows the time dependence for x rays near the K edge of Ne with the 100-fs optical pulse centered at 150 fs. The energy band of these x rays shifts in time because of a changing ionization balance associated with a changing temperature. These shifts, combined with a change in the magnitude of the peak, give rise to the time dependence shown in the figure. Figure 4(c) also shows the time dependence for representative x rays that do not have enough energy to ionize K-shell electrons but can still ionize electrons out of the L shell. The rise time for these x rays is slower.

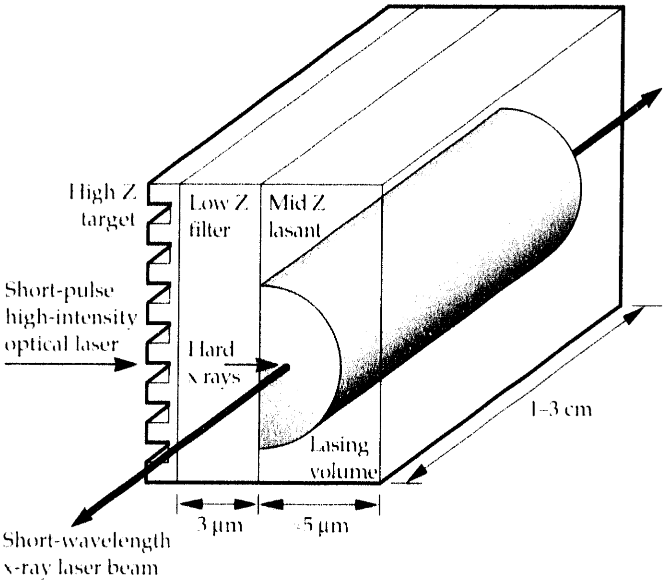

FIGURE 3. Schematic of a complete inner-shell photo-ionized x-ray laser.

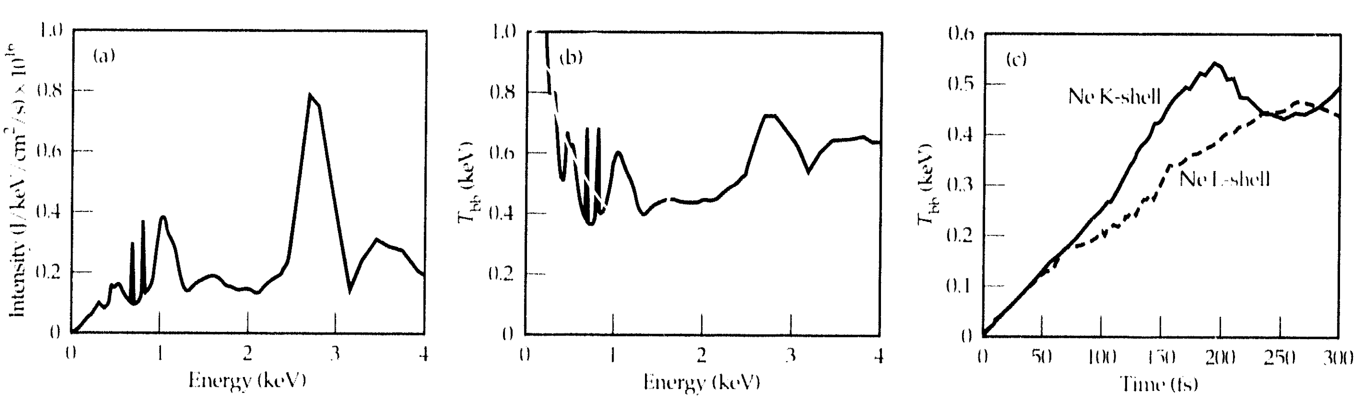

FIGURE 4. (a) Spectrum of a 1000-Å Au target at 100 fs after peak of 100-fs (FWHM) pulse. The absorbed intensity on each side of the Au foil is 10^{17} W/cm^2. (b) The spectrum expressed in terms of an equivalent blackbody temperature (T_{bb}). (c) Time-dependent equivalent blackbody temperature used for K- and L-shell ionization.

X-Ray Laser Gain Calculations

In general, there are three important ranges for the gain-length *GL* product of an x-ray laser:

1. In the smallest range (*GL* ≈ 5), there is a clear demonstration of lasing.
2. In the mid-range (*GL* ≈ 10), there can be enough intensity in the lasing transition to be useful for applications (e.g., DaSilva *et al.*[6] obtained microscopy images using the Ni-like Ta collisional x-ray laser with a *GL* ≈ 8).
3. In the largest range (*GL* ≈ 15), saturation is reached. The only x-ray lasers that have obtained saturation are Ne-like collisional schemes. Our calculations show that an inner-shell x-ray laser scheme could operate in the first two ranges with driver laser energies in the 5 to 10 J category, with saturation requiring approximately 15 J.

In this article, we present gain calculations for an Ne lasant, ionized by x rays emitted from an Au target after passing through a 3-μm Be filter. We use the driving laser conditions discussed earlier (i.e., absorbed intensity of 10^{17} W/cm^2 and a 100-fs FWHM pulse duration). We modeled the calculated time-dependent LASNEX emission spectrum as a composite of two blackbodies with time-dependent temperatures. One temperature characterizes the incident x-ray flux at energies just above the K edge; the other characterizes the incident x-ray flux that enters into the calculation of the L-shell ionization. The relatively rapid decrease in the cross sections makes this approximation reasonable, despite the nonthermal property of the spectrum [Fig. 4(b)]. Previous calculations modeled the x-ray source as a single T_{bb}.[2] For future calculations, we plan to extend our modeling to use the LASNEX spectrum.

The rise time for the two x-ray sources is obtained from smooth fits to the two curves [Fig. 4(c)]. We used the blackbody fluxes to calculate ionization after accounting for absorption in the filter. The Ne is at a density of 1.5×10^{20} cm^{-3} in liquid H. The 1% of Ne in the mixture absorbs almost all of the x rays. The H is present to thermalize the energetic photo and Auger electrons that could ionize the Ne. Figure 5 shows the time dependence of the calculated gain in Ne for the 2p–1s transition at 14.6 Å.

The peak gain coefficient is about 5 cm^{-1} with an FWHM duration of approximately 20 fs. For a 1-cm-long target and absorbed energy of 5 J, this gain coefficient would give *GL* ≈ 5, showing clear demonstration of lasing. Longer lengths and larger input energies are required to provide a useful amount of x rays for applications and to reach saturation. We calculated the saturation intensity for this scheme to be relatively high (≈10^{13}W/cm^2), because the rapid Auger rate out of the upper-laser level makes it resistant to change. However, the short duration (≈20 fs) and small cross-sectional area combine to give an output energy on the order of 1 μJ/pulse. For an input pulse of 10 J, this corresponds to an efficiency of 10^{-7}. This efficiency is approximately a factor of 10 lower than that obtained using saturated collisional x-ray lasers with kilojoule inputs and millijoule outputs.[1]

The repetition rate at the driving laser will be important in determining the range of applications appropriate for a short wavelength x-ray laser with 1 μJ/pulse.

Conclusion

The prospect of having driving lasers with a pulse duration of 100 fs and energies in the 5 to 15 J range motivates a renewed consideration of inner-shell x-ray laser schemes. A scheme based on K-shell ionization using Ne to Cl as the lasant material could provide lasing in the 15 to 5 Å wavelength regime. The calculated x-ray flux from an Au target heated by such a high-power driving laser is sufficient to obtain lasing with a gain coefficient in Ne on the order of 5/cm. For a driving laser energy of 5 to 15 J, this gain should allow clear demonstration of lasing and may provide enough energy to reach saturation. We calculated saturated output pulses to have energies on the order of 1 μJ.

To improve our modeling techniques, we plan to: (1) Use the spectrum in the gain calculation instead of expressing the spectrum in terms of the T_{bb}. (2) Calculate the spectrum using a detailed atomic model

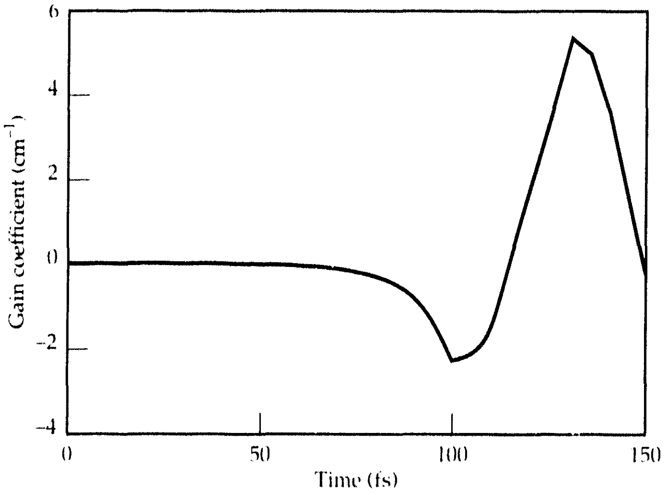

FIGURE 5. Time-dependent gain coefficient for an inner-shell photo-ionized Ne x-ray laser at a wavelength of 14.6 Å using the x-ray flux from an Au target heated by the optical pulse described in Fig. 4.

rather than the average-atom approximation, because we found there is a significant difference in adding angular momentum splitting within the average-atom approximation. Although detailed atomic models that treat individual ionization stages would calculate line emission more accurately, their assembly requirements and computational costs can be consuming. (3) Add the effects of ponderomotive forces in our calculation. We currently model the grooved targets as expanding planar foils without including any ponderomotive force associated with the intense laser field. Mourou and Umstadter[7] observed that ponderomotive forces inhibit expansion when heating slab targets with short-pulse high-intensity lasers. The resulting higher densities associated with inhibited expansion could affect the emitted x-ray spectrum. (4) In addition to H, consider other low-Z materials to slow down the energetic photo and Auger electrons.

Currently, short-pulse driving lasers with sufficient energy to obtain lasing are not available, but we can study many aspects of these inner-shell x-ray laser schemes with existing lasers by using spot rather than line focus. An important measurement is the time-dependent spectrum of the emitted x rays as a function of laser intensity and target material. We should also address the issue of fabricating targets with a large amount of H or other low-Z material, which is required to thermalize energetic electrons. One option might be a CH (plastic) foam target containing a lasant material.

Acknowledgments

We thank P. Amendt, R. Falcone, S. Gordon, and H. Kapteyn for informative discussions.

Notes and References

1. *X-Ray Lasers 1992, Proceedings of the 3rd International Colloquium on X-Ray Lasers,* IOP Conf. Ser. 125, Ed., E. E. Fill (IOP, Bristol, England, 1992), and references therein.
2. H. C. Kapteyn, "Photoionization-pumped x-ray lasers using ultrashort-pulse excitation," *Appl. Opt.* **31**, 4931–4939 (1992).
3. G. L. Strobel, D. C. Eder, R. A. London, M. D. Rosen, R. W. Falcone, and S. P. Gordon, "Inner-shell photo-ionized x-ray laser schemes," in *Short-Pulse High-Intensity Lasers and Applications,* Ed., H. A. Baldis (SPIE—International Society for Optical Engineering, Bellingham, WA, 1993; *Proc. SPIE* **1860**).
4. M. A. Duguay and P. M. Rentzepis, "Some approaches to vacuum UV and x-ray lasers," *Appl. Phys. Lett.* **10**, pp. 350–352 (1967).
5. M. Murnane, H. Kapteyn, S. Gordon, S. Verghese, J. Bokor, W. Mansfield, R. Gnall, E. Glytsis, T. Gaylord, and R. Falcone, "Efficient coupling of high-intensity sub-picosecond laser pulses into dilute solid targets," in *Short Wavelength Coherent Radiation: Generation and Application,* Eds. P. H. Bucksbaum and N. M. Ceglio (Optical Society of America—OSA, Washington, DC, 1991) pp. 281–284.
6. L. B. DaSilva, J. E. Trebes, R. Balhorn, S. Mrowka, E. Anderson, D. T. Attwood, T. W. Barbee Jr., J. Brase, M. Corzett, J. Gray, J. A. Koch, C. Lee, D. Kern, R. A. London, B. J. MacGowan, D. L. Matthews, and G. Stone, "X-ray laser microscopy of rat sperm nuclei," *Science* **258**, 269–271 (1992).
7. G. Mourou and D. Umstadter, "Development and applications of compact high-intensity lasers," *Phys. Fluids B* **4**, 2315–2325 (1992).

X-RAY RADIOGRAPHIC MEASUREMENTS OF RADIATION-DRIVEN SHOCK AND INTERFACE MOTION IN SOLID DENSITY MATERIALS

B. A. Hammel *B. A. Remington*
D. Griswold *P. L. Miller*
O. L. Landen *T. A. Peyser*
T. S. Perry *J. D. Kilkenny*

In the work reported here, we studied shock propagation and interface motion in solid density plastic samples, using time-resolved x-ray radiography measurements at high photon energy. Previous x-ray backlighting measurements used an x-ray collecting optic,[1] which has decreased sensitivity at ≳ 3 keV, or a pinhole imager, which has a small collection angle. By coupling a slit imager to an x-ray streak camera, we extended radiographic measurements to ~7 keV. For the first time, we have directly observed radiation-driven shock waves in solid density materials, and measured the shock position as a function of time and material compression from x-ray transmission. Unlike optical techniques, this radiographic method allows measurement behind the shock front, since the shocked material remains partially transparent to the probing x rays. By doping a section of a sample with a high-Z material (Br) for contrast, we measure the shock-induced motion of the interface between doped and undoped materials of comparable density.

Introduction

An understanding of hydrodynamic phenomena, such as shock propagation, interface motion, and material mix, is essential to the study of ICF; however, experimental observations of these phenomena in high-density materials ($\rho \geq 1$ g/cm^3) are difficult. X-ray techniques, such as point projection spectroscopy[2] and radiography,[3] can probe dense samples with high time resolution, but require high photon energies to penetrate the sample.

Limits on instrumental spatial resolution constrain the design of hydrodynamic experiments at solid densities to millimeter-scale sample dimensions, which, in turn, constrain the measurement technique to high-energy x rays. As an example, consider an experiment where one would like to measure the growth of random perturbations at the interface between two materials of different mass density due to the passage of a shock. The growth leads to interpenetration of the two materials, or "mix."[4] The growth rate of an initial perturbation at the interface with amplitude a_0 and wavelength λ is given by

$$\frac{da}{dt} = \frac{2\pi}{\lambda} a_0 v \frac{\rho_1 - \rho_2}{\rho_1 + \rho_2} , \qquad (1)$$

where ρ_2 and ρ_1 are the mass densities of the two materials and v is the interface velocity.[4] The growth rate is constant so long as the final amplitude is less than some fraction of λ. Therefore, linear growth of an initial perturbation by ten fold requires that the initial amplitude a_0 be less than 1/10 λ. As an example, consider the case where $a_0/\lambda = 1/60$ and there is a large density difference ($\rho_1 \gg \rho_2$). Under these conditions, the perturbation amplitude scales approximately as 1/10th the distance that the interface moves.

To prevent sample decompression and to minimize two-dimensional (2-D) effects (such as shock curvature), the dimensions of the sample both parallel to and transverse to the direction of shock propagation must be larger than the distance that the interface moves. The minimum growth observable is set by the spatial resolution of the detector; it is about 10 µm for the imaging techniques available for these types of measurements.[5] For reasonable resolution in this region (10 resolution elements across the mixed region), the interface must move about 1.0 mm, implying that the sample dimensions must be comparable. A direct measurement of the shock-induced growth in solids ($\rho \gtrsim 1$ g/cm^3) can therefore only be achieved by observing x rays that can penetrate materials with areal densities of ~0.1 g/cm^2. One-mm-thick plastic samples, which have relatively low opacity and are easy to fabricate, require photons with energies above 6 keV to represent less than one optical depth to the probing radiation.

Experimental Technique

In these experiments, CH samples were radiatively driven by x rays from a cylindrical gold hohlraum, which was heated with eight beams (0.35-μm-wavelength) of the Nova laser (Fig. 1). The duration, shape, and total energy of the laser pulse were varied, allowing the radiation drive to be optimized for a particular experiment. In the data presented here, the laser drive has ceased and the shock is decaying as it propagates into the material. Another beam of the laser (0.53-μm wavelength, 3-ns flat-topped pulse with an intensity of ~3×10^{14} W/cm^2) was focused onto an Fe disk to form a 0.8-mm-diam spot. This beam produces Fe K-shell emission at ~6.7 keV, which backlights the plastic sample.

The sample, which is nominally 0.7 mm diam and 1.5 mm in length, is mounted in a fixture from the wall of the hohlraum. It is viewed from a direction perpendicular to its length and, therefore, transverse to the direction of shock propagation. Although the sample is 0.7 mm diam, a mask permits only the central 0.3 mm of the cylinder to be viewed by the slit imager (described below). The backlighter disk is positioned nominally 3 mm behind the package. A wire or a gold grid (62-μm period) is mounted to the front of the sample (in the line of sight of the backlighting x-rays as viewed from the instrument), so that magnification and spatial resolution can be measured simultaneously with the shock trajectory.

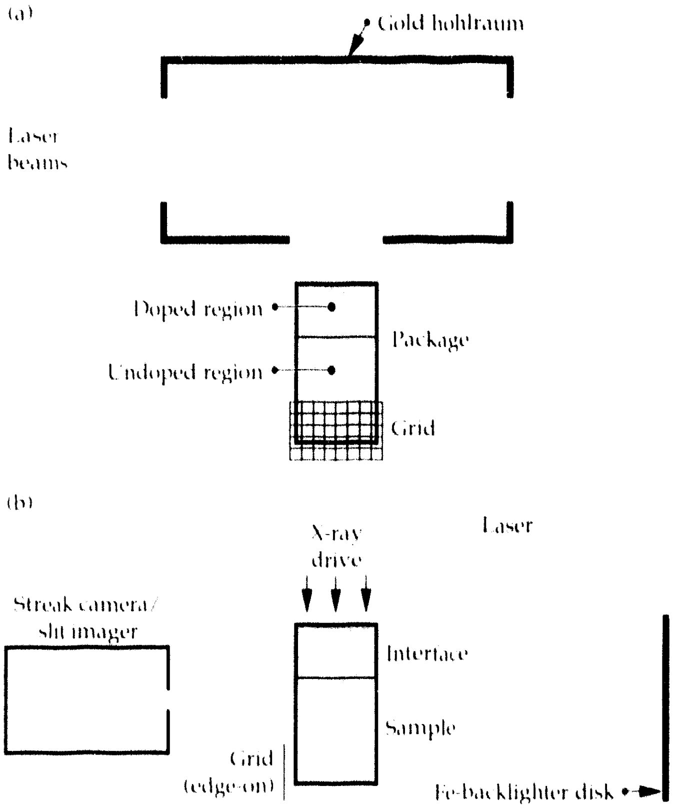

FIGURE 1. Schematic of the experimental set up. (a) The target as seen from the streaked imager with the backlighter disk behind the sample. (b) The sample viewed from the side.

The sample is imaged with 20× magnification using a slit imager coupled to an x-ray streak camera, providing a time resolved x-ray radiograph of the sample.[5] This instrument is filtered with 500-μm Be to discriminate against low energy photons. The imaging slit (10×750 μm) is oriented so that its length is parallel to the interface and hence perpendicular to the direction of shock motion. To achieve high spatial resolution, the imaging slit must be aligned so that it is parallel to the actual interface direction. This is achieved by first measuring the sample interface orientation on a precision microscope during target characterization and then rotating the imaging slit slightly to achieve the same orientation. This azimuthal alignment is done before each shot. The overall azimuthal uncertainty is less than 1°. Measurements of a backlit resolution grid indicate that the azimuthal alignment results in ~15-μm (FWHM) spatial resolution in the object plane, in the direction of shock propagation.[5] In these measurements, the use of a slit imager results in a factor of 40 increase in the aperture of the instrument when compared to a camera operated with a 10-μm-diam pinhole. The streak camera provides 160-ps temporal resolution and uses a CsI-coated photocathode for enhanced sensitivity to photon energies above 5 keV.

Shock compression of the sample increases the line density through the package in the viewing direction, resulting in a decrease in the transmitted x-ray intensity. To observe the motion or mixing of an interface between two materials, one region of the package is doped with 2–3 at.% Br for radiographic contrast, resulting in ~10% transmission of the backlighter x rays through the solid density ($\rho \sim 1.3$ g/cm^3) material. Transmission through the unshocked, undoped material ($\rho \sim 1.05$ g/cm^3) is 60%. In the absence of mixing, a planar interface between the doped and undoped material should appear as a sharp gradient in the transmitted x-ray light, degraded only by the spatial resolution of the detector and alignment uncertainties. Any curvature of the shock or interface leads to further degradation in this resolution.

To infer quantitative information about sample density from the radiographs of undoped targets, we must know both the sample opacity κ_ν and the backlighter spectral shape. For high energy backlighter emission with energies $h\nu$ which are well above the K-edge in the sample material E_k and for low sample temperatures (where $kT << E_k$), the opacity of the sample material is nearly identical to the cold material opacity. Uncertainties in the backlighter spectrum, however, lead to corresponding uncertainties in the transmission (at a specific energy) through the sample, limiting the accuracy with which sample areal density can be measured. To minimize this effect, we used a 13-μm-thick Fe filter on the detector. This filter preferentially transmits the Fe He- and Ly-α lines from the backlighter while attenuating transitions from higher quantum levels and the free-bound continuum.[5] Under our conditions, because the backlighter spectrum contains no significant H-like emission, the backlighter is nearly monoenergetic (He-α). This can be seen in Fig. 2, where the measured backlighter spectra (with and without the Fe filter) and their running integrals are shown. Nevertheless, a low-level of continuum emission, extending toward high photon energies, cannot be accurately measured by this technique. It would bypass the instrument filters, leading to higher sample transmission and hence to an underestimate in sample compression. To further test the quantitative limits of our radiographic technique, we placed several CH filter strips over the entrance slit of the streak camera and, with the streaked slit imager and Fe filter, observed the resulting attenuated backlighter emission on a shot that had no hohlraum or sample. The observed attenuation through filters with thickness of 0.7 mm and 2.8 mm (mimicking a 4× increase in areal density due to shock compression) was 62 ± 5% and 16 ± 2% respectively. These numbers are in reasonable agreement with the calculated values of 60% and 13%; the errors are based on the level of noise in the data.

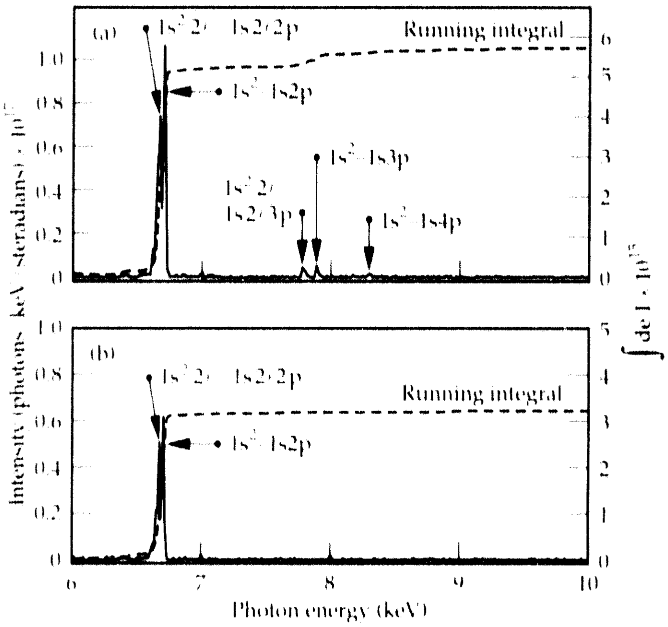

FIGURE 2. Measured spectrum of the Fe backlighter emission. Plotted are the intensity vs photon energy, corrected for film response and crystal reflectivity. The spectrometer used a 13-μm-thick Fe filter over one half of the film detector for simultaneous measurement of the spectrum with and without the filter. (a) The spectrum without the Fe filter shows emission primarily from Fe He-α ($1s^2$–$1s2p$), with some emission from higher lying levels (n = 3–1, etc.). (b) With the Fe filter, there is no measurable emission at energies above the Fe He-α line. This is most easily seen in the running integrals (dashed lines) of the two spectra (integrated over photon energy).

Spatial and temporal variations in backlighter intensity are also a concern for quantitative analysis of the data. Small scale-length variations, such as hot spots in the backlighter beam, are eliminated by the slit imager which averages across the beam profile. Long scale-length variations in backlighter intensity are ignored since this scale length (~0.5 mm) is much greater than that of the phenomenon under study. To minimize the effects of the backlighter structure and to allow for some thermal smoothing, we wait for the backlighter to reach a flat-topped intensity before we infer the sample compression. We account for temporal variations in the backlighter brightness by dividing the image by a time lineout taken from a part of the image that is ahead of the shock and hence free from density perturbations.

Measurements

Figure 3 shows a streaked radiograph of the shock from a typical shot passing through a plastic sample. The streak covers from 2 to 5 ns after the beginning of the drive pulse. The shock-compressed material appears as a region of decreased transmission. Figure 4 shows the position of the leading edge of the shock, along with a fit to the data, plotted as a function of time. The speed of the shock u_s, obtained by differentiating the fit with respect to time, is also shown. It is initially 75 μm/ns but slows during the duration of the streak as the shock

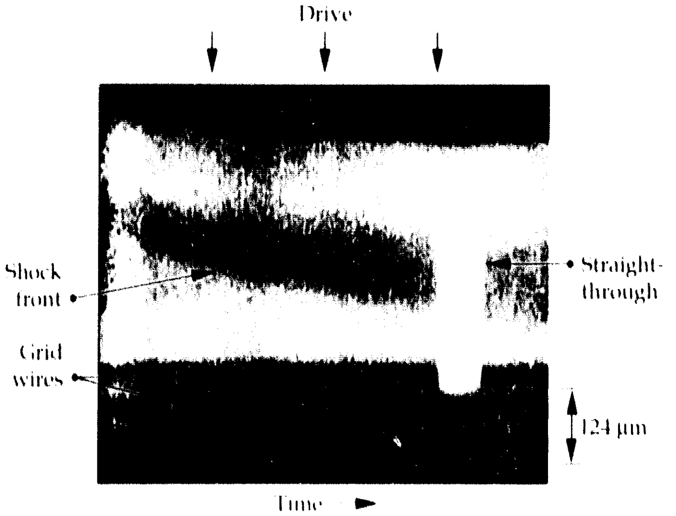

FIGURE 3. Streaked radiograph of an undoped plastic sample. The shock-compressed material appears as a region of decreased transmission. The "straight-through" feature is an artifact that arises from x rays that pass through the photocathode of the streak camera and interact directly with the phosphor screen. The streak covers from 2–5 ns after the start of the laser pulse.

decays. The sound speed in the unshocked material is ~2 μm/ns,[6] hence the Mach number is ~35 at this time. The pressure p associated with the shock is roughly given by $\rho_{us} u_s^2$, where ρ_{us} denotes the density in the unshocked material. This implies a pressure of 56 Mb. Calculations of a realistic equation of state (EOS) of the material give a somewhat lower value of 40 Mb.[7] In the limit of very strong shocks ($p \rightarrow \infty$), the material can be considered an ideal gas with a specific heat ratio γ of 5/3. In this case, the compression, or ratio of the densities in the shocked and unshocked material, corresponds to that occurring in an ideal gas in the strong shock limit ($\rho_s/\rho_{us} = 4$).[8] The compression, consistent with the material EOS for a steady state shock with the above speed in room temperature CH, is ~4.5.

The density in the shocked region can be inferred from the radiograph. For a monoenergetic backlighter, taking the log of the transmission ratio through the shocked and unshocked regions provides a measure of the optical depth of the compressed material with thickness ℓ, relative to that of the uncompressed material ahead of the shock where the transmission is known (60% at 6.7 keV). The transmission through the unshocked material is given by

$$I_{us}/I_0 = e^{-\kappa_\nu \rho_{us} \ell} = 0.60 \quad , \tag{2}$$

where I_{us} is the observed intensity, and I_0 is the unattenuated backlighter intensity. It can then be used to infer the density of the shocked material ρ_s since the density ρ_{us} is known:

$$\rho_s = \frac{\rho_{us}}{\ln(0.60)} \ln\left[\frac{(0.60)I_s}{I_{us}}\right] \quad . \tag{3}$$

The fractional error in the inferred compression in terms of the measured intensity can be written as

$$\frac{d(\rho_s/\rho_{us})}{\rho_s/\rho_{us}} = \frac{1}{\ln(0.6 I_s/I_{us})} \frac{d(I_s/I_{us})}{I_s/I_{us}}$$

$$\approx -0.7 \times \frac{d(I_s/I_{us})}{I_s/I_{us}} \quad , \tag{4}$$

since $I_s/I_{us} \approx 0.4$ for this measurement. Therefore, a typical random error of 15% in the measured value of I_s/I_{us} results in a ~10% error in the inferred compression. Figure 5 shows a plot of the inferred compression through the shock for three times during the streak record, after the backlighter has reached its flat-topped value. Early in the data, the peak density is nearly three times the solid. As the shock propagates further and decays, the density appears to decrease. Any curvature of the shock front will decrease the line density and hence lead to a lower estimate of the density of the shock compressed region. We are developing techniques to measure the degree of curvature of the shock. Initial measurements, using a gated pinhole camera to obtain time resolved 2-D x-ray radiographic images of the shock, indicate that the shock front is curved and has a radius of ~0.7 mm. Future experiments will address techniques for the control of shock planarity.

Figure 6 shows a streaked radiograph of a 0.7-mm-diam sample, which consists of a Br doped section (0.24-mm long) butted to a undoped section (1.0-mm long). In this experiment a lower x-ray drive was used. The streak covers the period from 3 to 6 ns after the start of the drive. The doped section appears as an opaque region, leading to a clearly defined interface between the two materials. The radiograph in Fig. 6 shows the interface begin to move when the shock arrives. Here

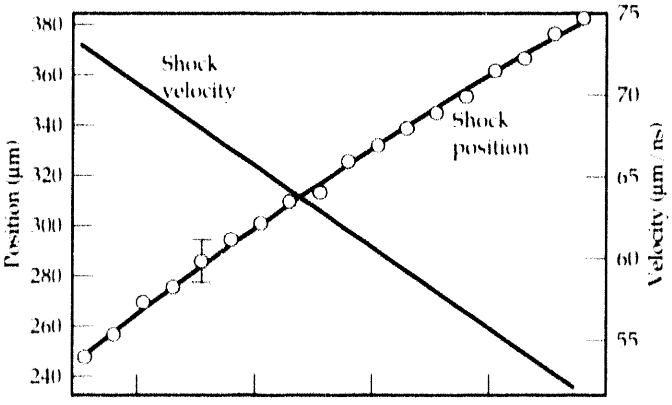

FIGURE 4. Shock position and velocity as a function of time. The error bar corresponds to the 15-μm (FWHM) instrument resolution.

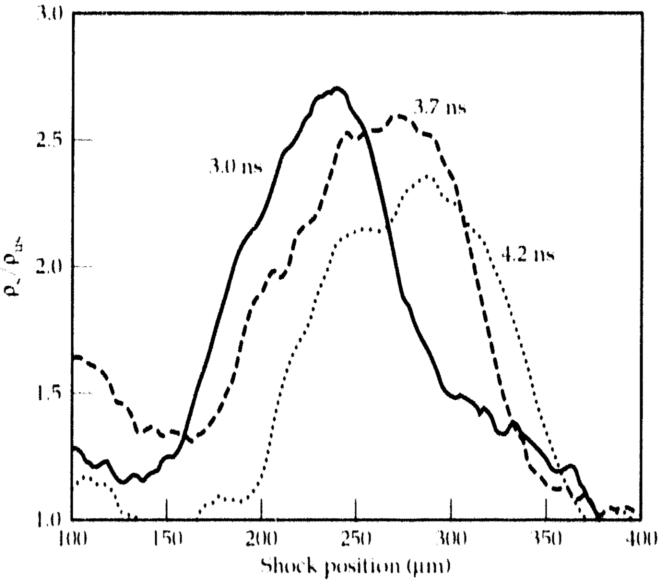

FIGURE 5. Measured compression through the shock as a function of position, inferred from backlighter transmission, at 3.0, 3.7, and 4.2 ns after the start of the drive.

the shock and interface are not sufficiently far apart to resolve them separately. The initial interface velocity is 24 µm/ns. By changing the time delay on the backlighter beam, we have observed the interface position as late as 25 ns after the start of the x-ray drive, after the interface has traveled 0.6 mm. In Fig. 7, we show data between 8–11 ns after the start of the drive, from a shot with higher x-ray drive. Here the shock is sufficiently ahead of the interface for both to be visible. Figure 8 shows the positions of the shock and interface as measured from this data. Fits to the data, along with the velocity of the shock u_s and interface v, obtained by differentiating the fits, are also shown. From the conservation of mass, in steady state, the compression is given by $\rho_s/\rho_{us} = (1 - v/u_s)^{-1}$. This data therefore provides an independent estimate of the compressed density. Taking $v/u_s = 3/5$ from the data at the beginning of the streak, we find $\rho_s/\rho_{us} = 2.5$. This technique, however, also underestimates the compression. Because the shocked particle velocity decreases with distance behind the shock, the interface velocity is not representative of the maximum shocked particle velocity.

Figure 9 shows the compression inferred via Eq. (2) from the measured x-ray transmission in Fig. 7, 9.1 ns after the start of the drive. Just ahead of the interface, a compression of 2.5 is achieved in the shocked undoped plastic; this in agreement with the conservation of mass

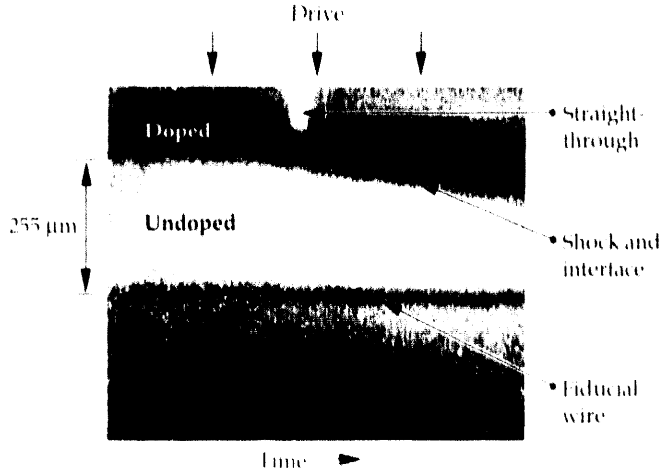

FIGURE 6. Streaked radiograph of plastic sample, where the first 0.24 mm was doped with 3 at.% Br to provide radiographic contrast at the interface. The interface begins to move when the shock arrives. The streak covers from 3–6 ns after the start of the laser pulse.

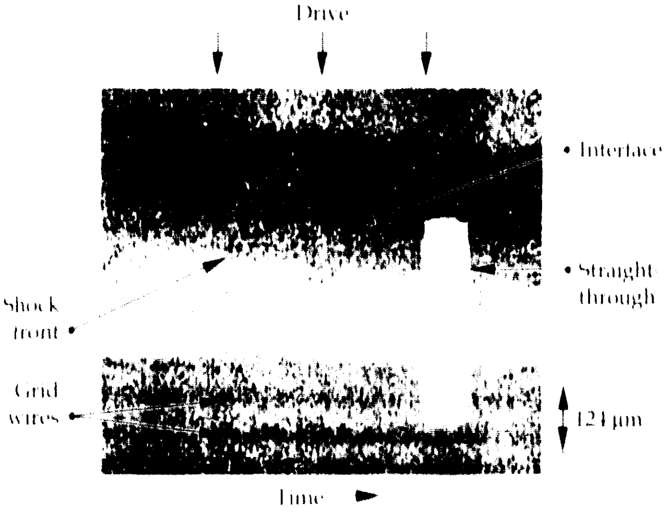

FIGURE 7. Streaked radiograph of plastic sample, where the first 0.30 mm was doped with 3 at.% Br. The shock has passed through the interface and both are visible. The streak covers from 8–11 ns after the start of the laser pulse.

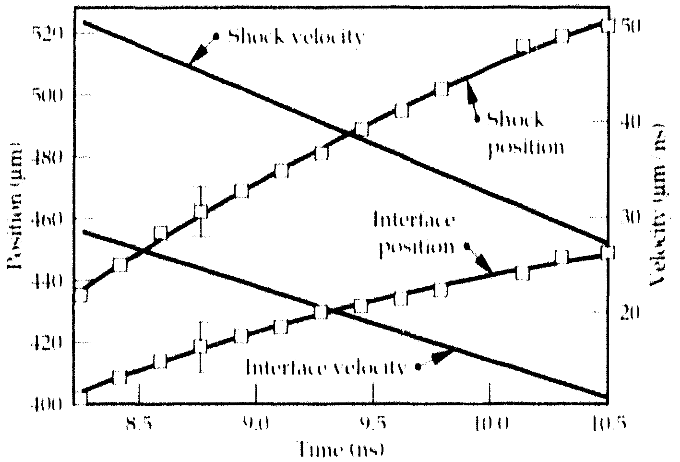

FIGURE 8. Shock and interface position as a function of time, for the data shown in Fig. 7. The shock and interface velocities as a function of time, obtained by differentiating the fit, are also shown.

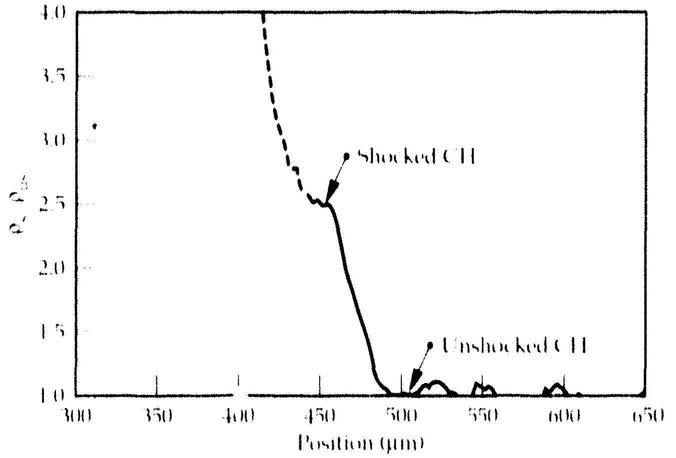

FIGURE 9. Measured compression through the shock-compressed CH 9.1 ns after the start of the drive, as inferred from the backlighter transmission. The apparent continued increase in density above 2.5 (dashed line) is due to the increase in the opacity due to the Br dopant, and does not represent the actual compression in the sample.

calculation. The apparent continued rise in the compression after the interface (dashed line) is due to attenuation of the probing x rays by the increased opacity of the Br-doped material, and therefore is no longer representative of the sample density.

Summary

Using time resolved x-ray radiography at high photon energy, we observed radiation driven shock and interface motion in solid density plastic samples. From the observed shock velocities, we infer shock pressures of ~40 Mb. With this technique, which allows us to directly measure the areal density in the shocked material, we infer a lower limit on the material compression of a factor of ~2.5. Furthermore, measurements of the interface motion behind the shock have enabled us to independently infer the compression via the continuity equation.

Measurements of shock propagation in solid density material have been performed by other researchers.[9] Observations of shock breakout, viewed from the rear side of a sample (opposite the drive), have provided measurements of shock velocities.[9] Measurements of shocks propagating through optically transparent materials have been performed by viewing the sample from the side.[10] The material becomes opaque as the shock propagates, providing a measurement of the shock velocity. X-ray radiography, however, is a more powerful technique, as it allows measurements ahead and behind the shock, as well as a means of inferring the compressed density. This technique promises to be very useful for the study of a large variety of hydrodynamic phenomena in solid density material. We are beginning experiments to address material mixing in samples with dissimilar densities. In addition, we are planning experiments to measure the EOS in various materials, through measurements of the shock and interface velocity[11] and the self similar motion of impulsively driven shocks.[12]

Acknowledgments

We thank D. Phillion for providing us with computer codes to analyze the backlighter spectra, and R. Pasha for providing technical support.

Notes and References

1. J. D. Kilkenny, *Phys. Fluids B*, **2**, 1440 (1990); B. A. Remington, S. W. Haan, S. G. Glendinning, J. D. Kilkenny, D. H. Munro, and R. J. Wallace, *Phys. Rev. Lett.* **67**, 3259 (1991); B. A. Remington, S. W. Haan, S. G. Glendinning, J. D. Kilkenny, D. H. Munro, and R. J. Wallace, *Phys. Fluids B*, **4**, 967 (1992).
2. C. L. S. Lewis and J. McGlinchey, *Opt. Commun.* **53**, 179 (1985).
3. A. J. Cole, J. D. Jilkenny, R. T. Rumsby, R. G. Evans, C. J. Hooker, and M. H. Key, *Nature* **299**, 329 (1982); R. R. Whitlock, M. H. Emery, J. A. Stamper, E. A. McLean, S. P. Obenschain, and M. C. Peckerar, *Phys. Rev. Lett.* **52**, 819 (1984).
4. R. D. Richtmyer, *Commun. Pure Appl. Math.* **13**, 297 (1960).; E. E. Meshkov, *Izv. Akad. Nauk. SSSR Mekh. Zhidk.* Gaza **4**, 151, (1969) [*Izv. Acad. Sci. USSR Fluid Dynamics* **4**, 101 (1969)].
5. B. A. Remington, B. A. Hammel, O. L. Landen and R. A. Pasha, *Rev. Sci. Instrum.* **63**, 5083, (1992).
6. *Handbook of Chemistry and Physics*, (Chemical Rubber Co., Cleveland, Ohio, 1970), p. E41.
7. J. Nash, Lawrence Livermore National Laboratory, Livermore, CA, private communication, 1992.
8. Ya. B Zel'dovich and Yu. P Raizer, *Physics of Shock Waves and High Temperature Phenomena*, (Academic Press, New York, 1966), Vol. I, p. 52.
9. F. Cottet, J. P. Romain, R. Fabbro and G. Faral, *Phys. Rev. Lett.* **52** 1884 (1984), and references therein.
10. C. J. M. van Kessel and R. Sigel, *Phys. Rev. Lett.*, **33** 1020 (1974).
11. B. K. Godwal, S. K. Sikka and R. Chidambaram, *Phys. Reports* **102**, 121 (1983); R. Cobble, Lawrence Livermore National Laboratory, Livermore, CA, private communication, 1992.
12. S. A. Lilits, S. I. Anisimov and J. Meyer-ter-Vehn, *Z. Naturforsch* **47a**, 453 1992.

THE ROLE OF NODULE DEFECTS IN LASER-INDUCED DAMAGE OF MULTILAYER OPTICAL COATINGS

M. R. Kozlowski
M. C. Staggs
J. F. DeFord

Introduction

For high peak-power lasers, such as the prototype Beamlet Laser and the proposed 1–2 MJ National Ignition Facility, the system output fluence and architecture are influenced by the damage threshold of multilayer dielectric coatings used as high reflectors (HR) and polarizers.[1,2] The damage to these coating is generally localized in nature, typically initiating at preexisting defects in the coatings.[3,4] In an effort to understand the localized nature of the thin film damage, we recently employed two new tools: the atomic force microscope (AFM)[5], a scanning-probe microscopy technique that can provide nanometer-scale topographical information on dielectric materials, and AMOS, an electromagnetic modeling code that can calculate electric-field distributions at 3-D defects in multilayer structures.

Presently, hafnia/silica (HfO_2/SiO_2) material combinations deposited by electron-beam evaporation yield the highest and most consistent damage thresholds for the HR and polarizer coatings used in pulsed 1.06-µm lasers. The damage threshold of the coatings can be increased by a factor of 2–3 using a process called laser conditioning, in which the optics are illuminated at controlled subthreshold fluences.[1,6] An understanding of the mechanisms of laser-induced damage in these coatings is required to understand their limitations, as well as to develop better coatings.

In dielectric HR and polarizer coatings, the predominant surface defects are micrometer-scale domes associated with the classic nodule defect. These defects (Fig. 1) are initiated at seed particles present on the substrate or deposited in the film during deposition. Film deposition at these seeds results in the parabolic nodular defects. We are now exploiting the AFM technique to characterize defects in multilayer HR and polarizer coatings and to study, in-situ, the evolution of laser conditioning and laser damage on the films.

Historically, laser damage has been associated with peaks in the standing-wave electric-field (SWEF) distribution within the multilayer interference stacks.[7] The intensity of light at a given point is proportional to the square of the E-field magnitude. In common bulk dielectric optical materials, the local laser-induced E-fields increases by as much as a factor of 4 for simple defects such as cracks, grooves and spherical voids.[8] We use a finite-difference time-domain electromagnetic modeling code to predict the influence of 3-D nodule defects on the E-field distribution in the multilayer interference coatings. The modeling results are then corellated with the results of the AFM laser-damage studies.

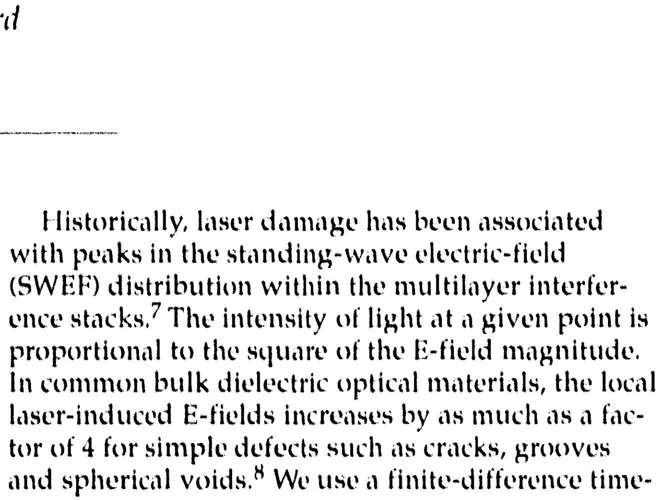

FIGURE 1. Geometry of an ideal nodule defect in a multilayer stack. The surface defect height *h* and the diameter *D* are determined by the defect seed diameter *d*, and depth *T*, as shown in Eq. (1).

AFM of As-Deposited Surfaces

The capabilities of the AFM were first used to map the surface topography of as-deposited and laser-damaged HR coatings.[4] The AFM has similarly been used to study laser damage at other materials, including multilayer antireflection coatings.[9-11] The coating presently studied is a multilayer stack consisting of alternating quarterwave-optical-thickness layers of HfO_2 and SiO_2. The top layer is a halfwave layer of SiO_2. Figures 2(a)–(c) show images, at three magnifications, of an area of an as-deposited coating. Most of the SiO_2 surface consists of a background of hillocks of approximately 200-nm width and 10-nm height. These high aspect-ratio features are difficult to resolve using optical or electron microscopy. Figure 2(c) shows a high magnification (5 × 5 µm) image of these hillocks. Topography studies of the single layers of HfO_2 and SiO_2 indicate that the hillocks reflect the columnar growth structure of the underlying HfO_2 layers.[4]

Irregularities in the surface of the HR coating consist of shallow domes and occasional craters. The defect shown in the lower right corner of Fig. 2(a), and at higher magnification in Fig. 2(b), is such a dome defect. The lateral dimension of these domes ranges from 1 to 10 µm with the vertical dimension typically less than one third of the lateral dimension. The density of micrometer-scale defects is on the order of $10/mm^2$, so that a typical random AFM scan (approximately 100 µm by 100 µm) does not include a defect.

Figure 3 shows 3-D AFM images of a dome or nodule defect and two types of crater defects. Also shown are schematic representations of such defects. Both experimental evidence and computer modeling show that the nodule defects are caused by geometrical effects initiated at surface irregularities during the deposition process.[12,13] Focused ion-beam cross-sectioning and chemical analysis of the coating defect indicate that the defect is initiated within the film by a seed, which has the same composition as the film. The seed is likely due to (1) splattering of large pieces of the coating material, especially HfO_2, from the e-beam charge or (2) contamination from the coating chamber.[14] The parabolic shape of the sides is the result of deposition while the substrate is moving in a planetary pattern.[12] Assuming an omnidirectional coating flux, a simple model for the nodule defect geometry (Fig. 1) is developed in which the defect height h and the diameter D are determined by the defect seed diameter d, and depth T as[15]

$$D = (8Td)^{1/2} \text{ and } h = d. \tag{1}$$

This model is used as a basis for the analysis of defect-topography data and for simulating the E-field distributions at ideal defects.

Two different types of craters are observed on the coating surface. The first type [Fig. 3(b)] reveals the layered nature of the films. The thicknesses of the layers visible in the image are consistent with the λ/4 layer

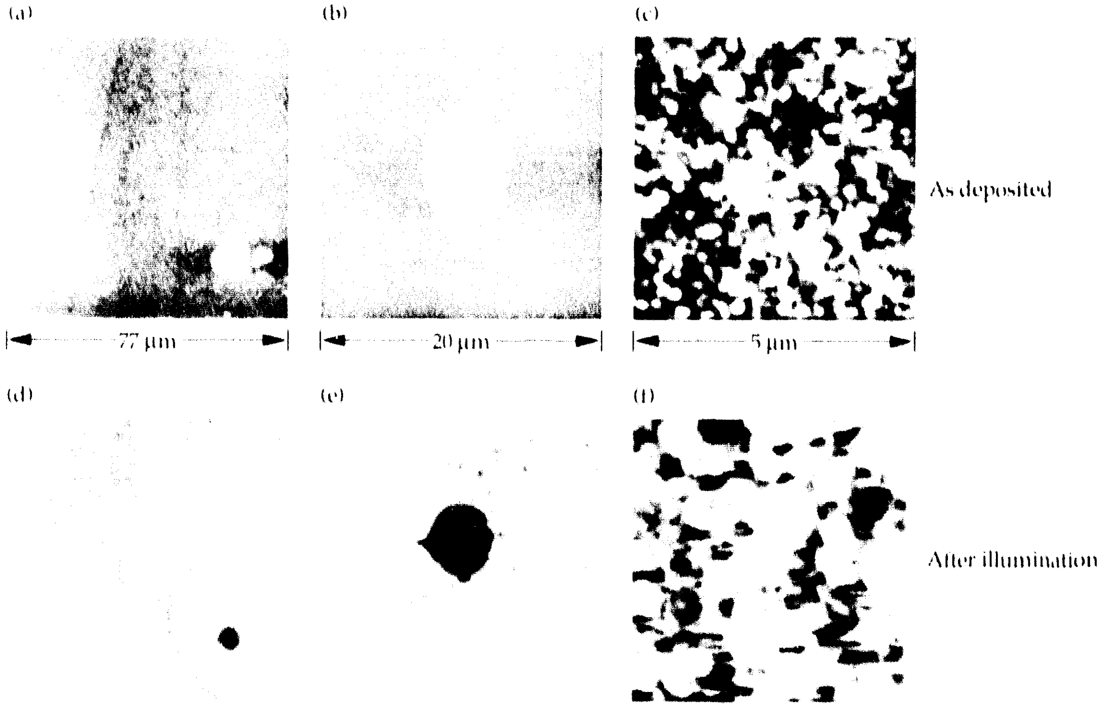

FIGURE 2. AFM images, at three magnifications, of an HR surface as-deposited and after illumination with one laser pulse at 43 J/cm² (a) and (d) show the full area studied, (b) and (e) the location of a nodule defect, and (c) and (f) a defect-free area.

thicknesses of the two materials used. This type of crater is likely created by the ejection of a nodule from the multilayer coating after material deposition is completed. The ejection is the result of the mechanical instability of the coating defect. It is associated with either stress in the coating material or voids at the nodule boundary caused by shadowing effects during nodule growth. The second type of crater [Fig. 3(c)] does not reveal the layered nature of the films. This suggests that ejection of a nodule occurred during the deposition process and that subsequent layers covered the crater walls. One of the issues to be addressed is the relative susceptibility of nodules and nodule craters to laser damage.

AFM of Laser-Damaged Surfaces

We next integrated the AFM into our standard laser-damage testing station[6] so that the topographical changes associated with laser damage could be studied. A 1064-nm Nd:YAG laser with a 8–10 ns pulsewidth and a beam diam of 1.3 mm at $1/e^2$ was focused onto the sample surface. Laser fluences were determined by beam profiling and total energy measurements. Figures 2(d)–(f) show the areas in Figs. 2(a)–(c) after illumination with a damaging laser pulse (43 J/cm^2). The most notable change in the surface is the ejection of the nodule leaving an almost circular crater with a single crack at its left-most edge [Fig. 2(d), (e)]. Although the nodule defects were generally found to be highly susceptible to laser damage, not all defects damaged at the same fluence. The nodule ejection itself is not considered catastrophic because very little of the film is actually removed. Catastrophic laser damage has been shown, however, to propagate from cracks originating at the boundaries of nodule defects.[4]

Another obvious change observed in the coating surface after damaging illumination is an increase in the size of the hillocks in the defect-free areas [Fig. 2(c), (f)]. The average diameter and height of the hillocks increased by approximately a factor of eight, indicating a type of growth or coalescence phenomenon had occurred. Such coalescence indicates that the surface reached temperatures high enough to allow surface migration of its constituents in nanosecond time-scales with resulting formation of larger structures of minimized surface free-energy. At these fluences, we also noticed that the interaction of the imaging tip with the surface often changed after laser exposure; the surface seemed to become sticky, indicating that adhesion between the tip and the substrate had increased substantially. This stickiness may indicate that the laser-exposed surface is more hygroscopic or has become charged. The stickiness can be minimized if a conductive Cr-plated tip is used, therefore suggesting that the charging explanation is more likely. Further study of the tip-surface interaction may provide insight into the mechanism for laser damage.

Damage Thresholds at Defect and Defect-Free Areas

Additional AFM-assisted laser-damage experiments at different fluences indicated that nodule ejection typically occurs at lower fluences than does hillock coalescence. The results of the AFM measurements were correlated with the damage features observed using Nomarski phase-detection microscopy, the common method of damage characterization used at LLNL. Although Nomarski microscopy has lower spatial resolution, with it we can quickly identify defect and

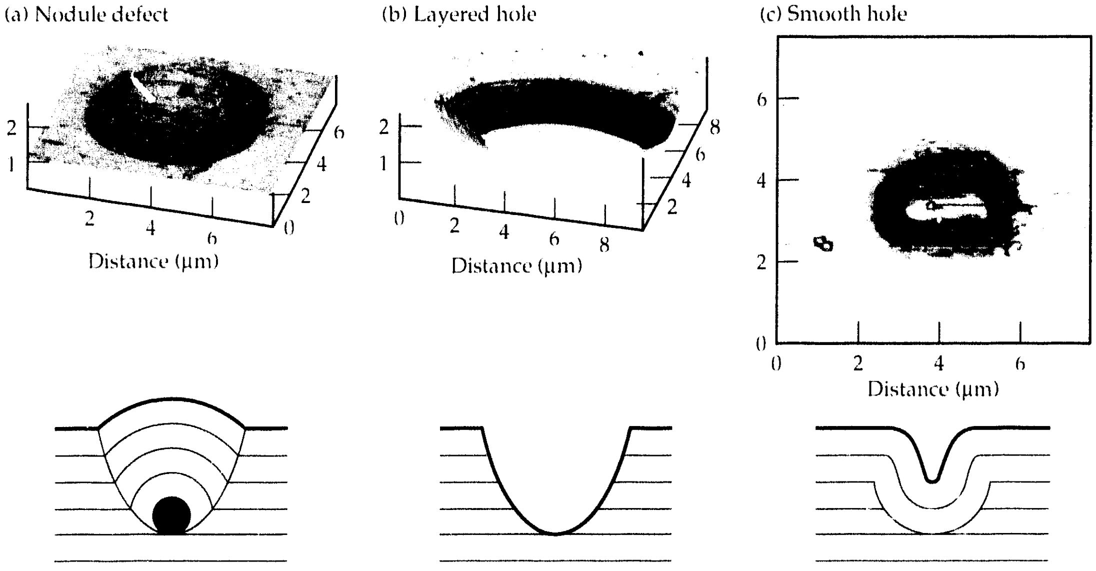
(a) Nodule defect

(b) Layered hole

(c) Smooth hole

FIGURE 3. 3-D images of the three types of surface defects observed on the HR coatings. Also shown are schematic representations of the coating defects.

defect-free areas. Our goal was to determine the actual damage thresholds for these areas. We were particularly interested in the difference between damage thresholds of the as-deposited and laser-conditioned areas of the coating. A 100-µm-diam damage testing beam was used so that defect and defect-free areas could be tested individually.[16]

Figure 4 shows the laser damage thresholds obtained in these small-area tests. We measured the unconditioned damage threshold by illuminating individual areas of the coating, each with a separate fluence, to determine at which fluence the damage would begin. The nominal unconditioned threshold for defects was 7 J/cm^2. The corresponding threshold for the defect-free areas was 50 J/cm^2. The damage threshold measured in the defect areas corresponds well with the threshold measured using the standard 1.2-mm beam that covers both defect and defect-free regions. Not surprisingly, these results showed that the defects are the features most susceptible to laser damage.

Figure 4 also shows the conditioned thresholds for the defect and defect-free areas of the coating. The conditioned threshold is measured by illuminating the area of interest with many pulses of increasing fluence starting at fluences well below the unconditioned threshold. The threshold for the conditioned defects is about 3 times that of the unconditioned defects. In contrast, the defect-free areas show no significant change in threshold on conditioning. The conditioned threshold of the defects is also lower than either damage threshold of the defect-free area. These results indicate that the defects control both the unconditioned and the conditioned thresholds for the coatings. This conclusion is supported by the observation that for the conditioned defect tests, the areas surrounding the defects showed no collateral damage at fluences near the defect threshold.

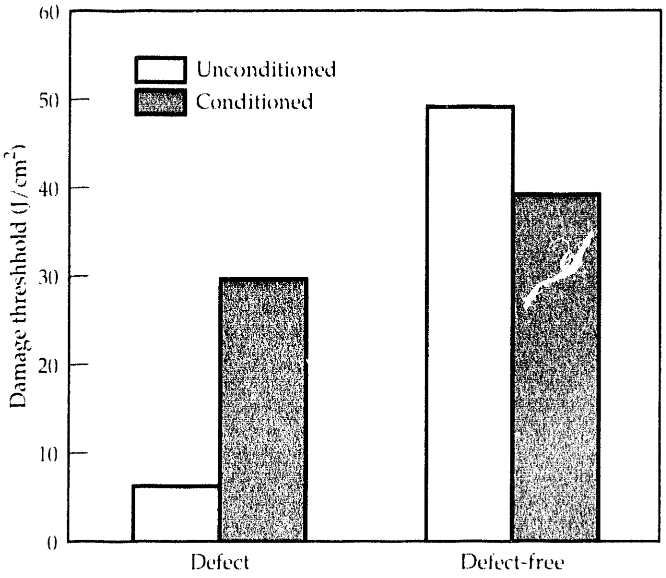

FIGURE 4. Unconditioned and conditioned laser damage thresholds measured at coating defects and at defect-free areas using a 85-µm-diam beam. Laser parameters: λ = 1.06 µm, pulse length = 10 ns, repetition rate = 20 Hz.

It should be noted that the abruptness of the damage threshold was different for defect and defect-free areas. For defect-free areas, the threshold was sharp with most variations within the ±15% accuracy of the damage threshold measurement. In contrast, for defect areas, the thresholds varied by more than a factor of two. The thresholds given in Fig. 4 represent the low end of each range. The threshold variation suggests that all defects are not the same. One might expect that the interaction of laser light with the defect, and the mechanical stability of the defect itself, may be dependent on the size and shape of the defect and, in particular, the layer depth at which it originates.

Geometric Model of Nodule Defects

Using the AFM, we characterized the shapes of a large number of nodule defects to aid in identifying any correlation to damage susceptibility and to improve our understanding of how and when the defects are initiated. Two HR coatings with the same design but deposited during different coating runs were examined. Figure 5 shows the diameters and heights of 23 defects found over an area of a few square centimeters on one of the samples (15D). The data show a general increase in defect diameter with height. Note that the data is plotted as diameter squared vs height and forms a line that passes through the origin. This type of correlation is predicted from Eq. (1) if all of the defects initiate at the same depth, as would occur when the source becomes unstable and ejects particles only once during the deposition. The second sample (09A) showed a wider spread

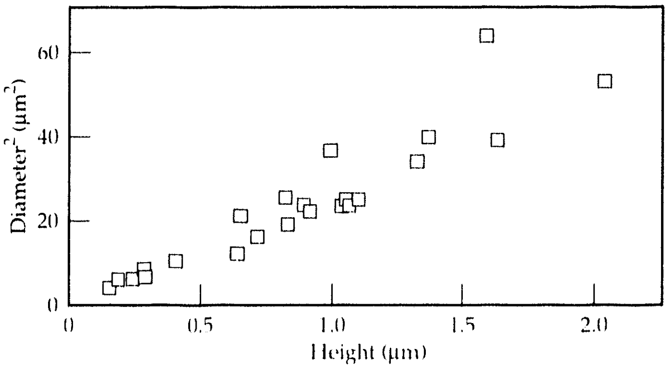

FIGURE 5. Plot of diameter squared vs height for defects found on sample 15D.

in the data, indicating that defects were formed at several different times during the coating deposition.[17] This data supports the simple geometric model for defects given by Eq. (1) and suggests that the AFM can serve as a nondestructive evaluation tool to identify when source instabilities occur during a given coating run.

Damage Susceptibility vs Defect Size

We next irradiated at various laser fluences a large number of defects on the HR coating samples. Each defect was illuminated at only one fluence ranging from 4 to 35 J/cm^2. The conventional unconditioned damage threshold for these coatings was near 4.7 J/cm^2 at 10 ns. Figure 6 shows the heights of various defects examined on the two samples. Each defect was illuminated at the indicated fluence. In both samples, defects with heights greater than approximately 0.6 µm are most susceptible to damage. It is not clear from the data if the damage threshold varies with defect height or if there is only a threshold height above which damage is likely for the range of fluences tested.

The diameters of the defects studied in Fig. 6 were also measured. Plots of the defect diameter vs fluence for this data indicate that the damage susceptibility of the defects cannot be simply correlated to defect diameter. Nodule height, therefore, is the defect parameter that may prove useful in predicting the damage susceptibility of nodules in multilayer coatings.

Six crater defects (holes left by nodules ejected prior to illumination) were also illuminated on the samples. Figure 7 shows that, over the range of fluences used in nodule damage studies, none of the crater defects were damaged. This data, although limited, may indicate that nodule craters have less effect on the coating damage threshold than the nodules themselves.

Electric-Field Modeling at Defects

One possible explanation for the increased damage susceptibility of the nodules is an increase in the local electric fields in the coating. To test this explanation, we examined the influence of simple nodule defects on the SWEF of multilayer stacks. The computer program used, AMOS,[18] is a finite-difference time-domain (FDTD) code that can integrate the full time-dependent Maxwell equations for 2-D systems and for rotationally symmetric 3-D systems such as the nodule defects defined by Eq. (1). The FDTD technique involves distributing the electric and magnetic field components on a regular rectangular grid that fills the simulation volume and then updating the Maxwell equations using an explicit leapfrog integration scheme. AMOS (1) calculates the SWEF distribution, which is caused by a monochromatic plane-wave incident on the coating/defect system, by illuminating the coating with a pulse and (2) takes the Fourier-transform of the resulting fields at the frequency of interest. Our test calculations on systems with known analytical solutions, such as a perfect dielectric-stack mirror and an isolated dielectric sphere in free space, showed that the FDTD technique is valid in the regime of interest for mirror-defect modeling.[19]

Figure 8 shows the geometry of a cylindrically symmetric defect initiated by a HfO$_2$ seed in a multilayer stack, as well as the boundary conditions used in modeling this defect. The defect geometry is based on Eq. (1)

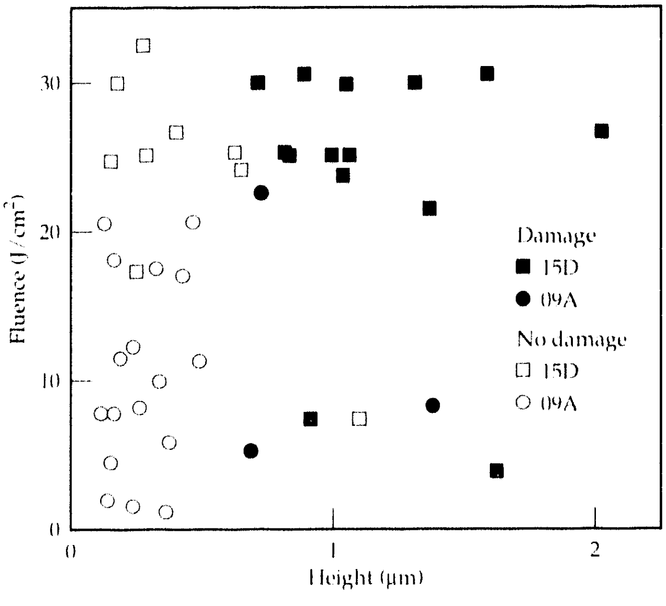

FIGURE 6. Plot of fluence vs height of nodule defects on samples 15D and 09A.

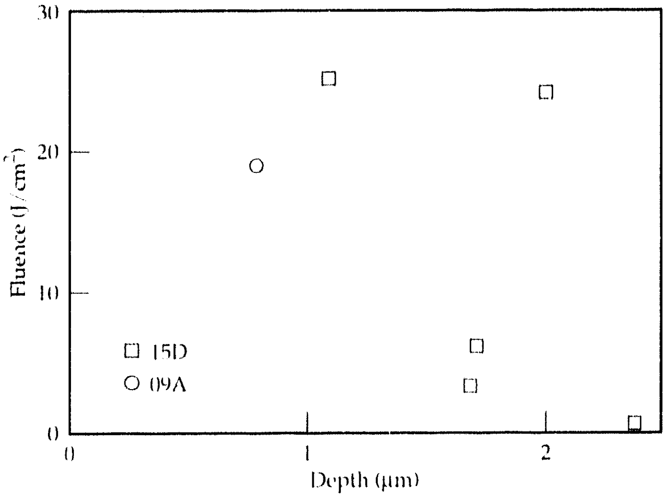

FIGURE 7. Plot of fluence vs diameter of nodule craters on samples 09A and 15D.

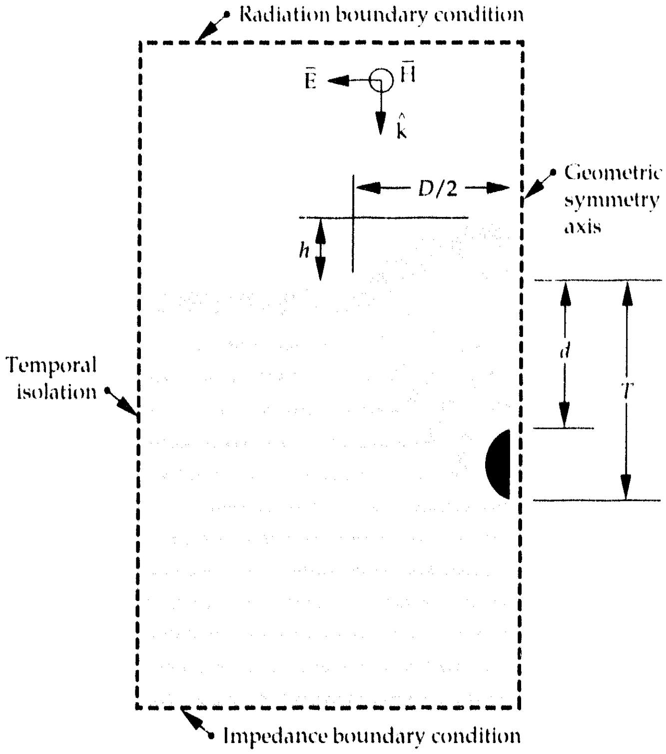

FIGURE 8. The geometry of a model cylindrically symmetric nodule defect within a multilayer stack. The boundary conditions used to model the SWEF pattern in the defect are shown. For this defect, $d = 0.67\ \lambda$ (HfO_2) and $T = 3.25\ \lambda$. $\hat{\mathbf{k}}$ is the direction of propagation of the plane wave and $\bar{\mathbf{E}}$ and $\bar{\mathbf{H}}$ are the electric and magnetic field vectors, respectively.

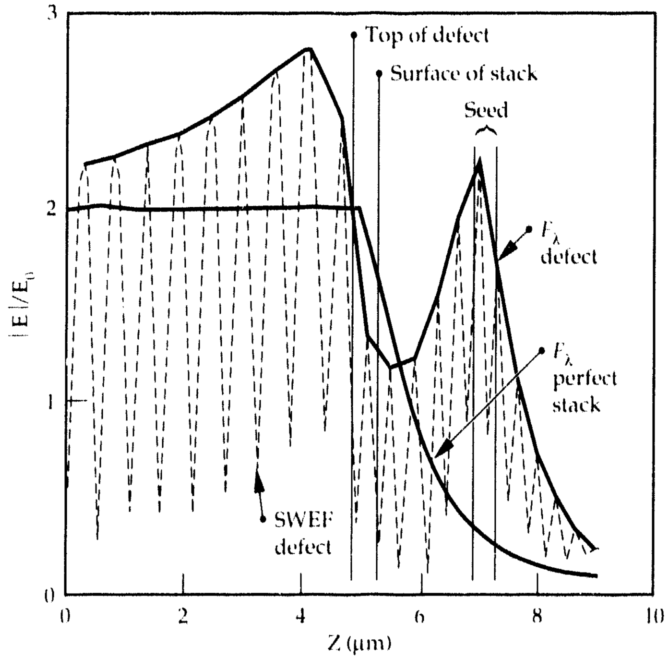

FIGURE 9. SWEF distribution along the axis of the nodule defect shown in Fig. 8. A line connecting the peaks in a SWEF curve is identified as F_λ. Also shown is the F_λ plot for the perfect stack.

using a seed diam of 0.37 μm (0.67 λ HfO_2) and a seed depth of 2.18 μm (3.25 λ). Figure 9 shows the SWEF distribution calculated along the axis of the defect. The magnitude of the calculated field $|E|$ is normalized to the incident field E_0. We report E-fields only on the defect axis, since studies of other locations consistently showed lower E-fields. To simplify the remaining SWEF plots, we plot only the set of points corresponding to the peaks F_λ in the SWEF plot. This set of points is shown as the solid line in Fig. 9.

Superimposed on Fig. 9 is the curve showing the F_λ curve for the multilayer stack without a defect. For the perfect stack, $|E|/E_0$ equals 2.0 above the coating surface but falls off quickly within the stack. In the case of the defect, $|E|/E_0$ approaches 2.0 at distances far from the surface of the coating. There are two predominant features in the SWEF pattern along the defect axis: a maximum value above the defect surface F_a, and a maximum value in the defect F_d. In this figure, and in most other cases, F_d occurs within the defect seed. F_d is our main interest, as F_a should have little influence on the damage threshold of the underlying material. The peak field in the defect seed is higher than at any point in the perfect stack. Because the E-field, and therefore the light intensity, is highest at the defect seed, this area of the coating is expected to show increased laser-damage susceptibility.

Various other defect shapes defined by Eq. (1) were also modeled. Figure 10 shows how the SWEF distribution varies with seed depth. Here the seed size is 1 λ.

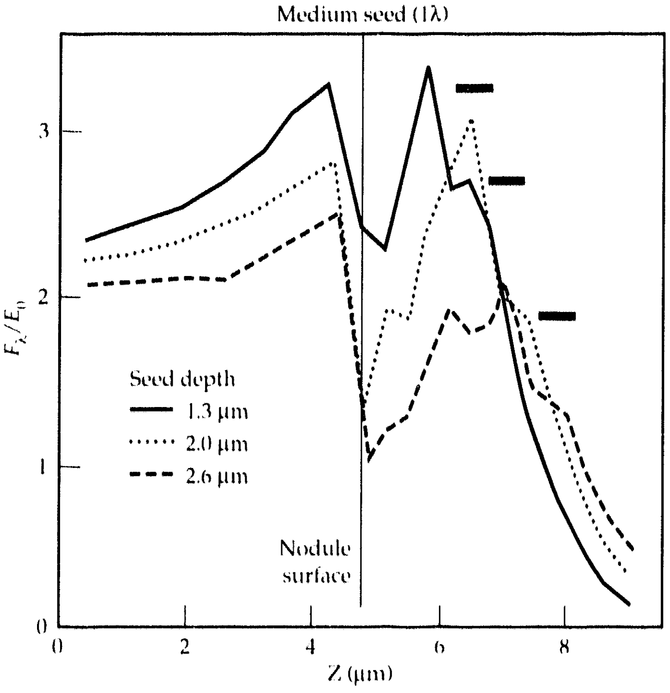

FIGURE 10. F_λ/E_0 curves along the axis of nodules with 0.55-μm (1 λ) seeds deposited at three different depths. The seed positions are given by the horizontal bars.

The location of F_d follows the seed position and the magnitude of F_d decreases as the seed depth T increases. Note that, in contrast to the defect modeled in Fig. 9, F_d for the 1-λ seed is located slightly above the seed.

We also calculated the SWEF distributions for the case where the nodule defect was removed leaving only a parabolic crater. Figure 11 shows the F_λ profiles calculated for the same defect geometries as in Fig. 10, but with the defect removed. The surface segment overlaid on each curve shows the location of the bottom of the crater. In all cases, the peak observed in the E-field is located within the crater void rather than in the coating. The E-field enhancement in the film is on the order of only 1.5× for the crater defect, which is much less than the enhancements calculated when the defects are intact.

The modeling results agree qualitatively with those of the AFM study on several counts:

1. The modeling predicts increased damage susceptibility of the nodule defects.
2. The expected damage susceptibility is dependent on the defect shape.
3. The crater defects are predicted to have lower damage susceptibility than the nodules themselves.

AFM of Laser-Conditioned Surfaces

Having shown that the damage threshold of both as-deposited and laser-conditioned coatings are controlled by the nodule defects, we wished to identify the laser-induced changes in the defects that could account for the laser conditioning effect. We used the AFM to look for changes in the film and defect morphology. Sites on and near nodules were imaged before and after irradiating the coatings with increasing subthreshold fluences.

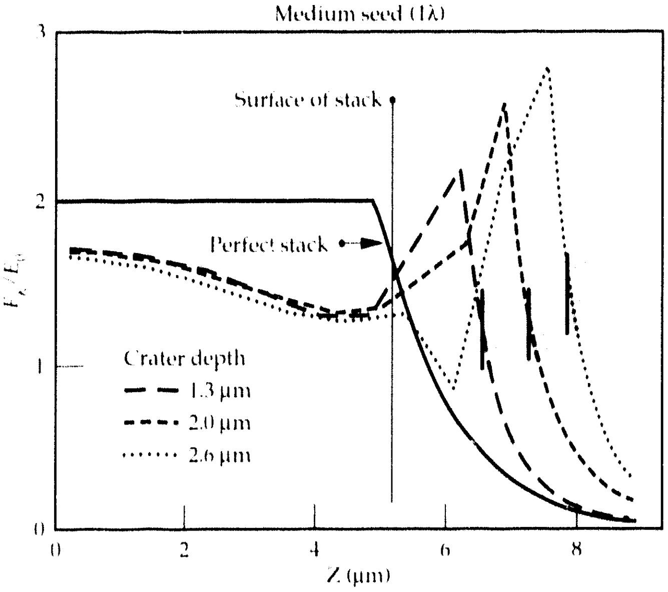

FIGURE 11. F_λ curves along the axis of craters left by the removal of the three nodules modeled in Fig. 10. The vertical bars show the locations of the respective crater bottoms.

A typical 2.5-μm-diam nodule was illuminated with eight pulses of increasing fluence ranging from 7.8 J/cm² to 56 J/cm². This range of fluences starts below the unconditioned damage threshold of the defects on the particular coating and increases until a level is reached that causes ejection of the nodule. Figure 12 shows line scans of an area near the edge of the defect at four stages of the illumination process: before illumination and after the 2nd, 3rd and 7th pulse. No changes were apparent after the first two pulses. However, after the third pulse, at 19.8 J/cm², much of the nodule's 10-nm-scale surface roughness has been removed. No further changes in the surface structure were observed with subsequent pulses up to 54.6 J/cm², although the nodule was ejected after the next pulse at 56 J/cm². The smoothing of the surface occurs in a fluence range at which an unconditioned defect would normally be ejected. Damage does not occur until fluences above the typical large-area conditioned damage threshold of these films are reached. We believe that this surface smoothing is associated with the laser conditioning process. The smoothing may indicate a melting or flowing of the material, which may result in the stabilization of the mechanically unstable defects.

Conclusions

Advances in AFM have made it easier to characterize and to monitor laser-induced damage at defects in optical coatings. In studies of HfO_2/SiO_2 multilayers, we found that nodule defects with large dome heights (particularly those above 0.6 μm) are most susceptible

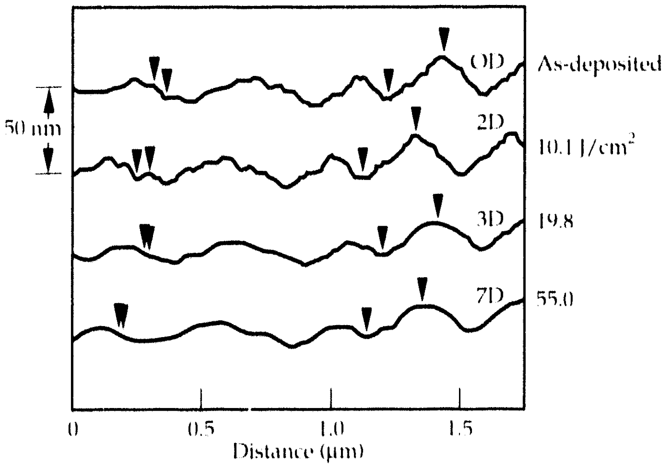

FIGURE 12. AFM images of the top of a defect at four stages during the laser-conditioning program.

to laser-induced damage. Nodule craters left by nodules ejected prior to illumination showed no increased damage susceptibility. Smoothing of 10 µm-scale surface features on the coating may be associated with the laser conditioning effect that raises the damage threshold of the films.

Advances in numerical modeling methods have also made it possible to study the influence of nodule defects on the laser-induced electric fields within the coatings. The modeling results show qualitative agreement with the results of the AFM study in that nodule defects show increased damage susceptibility, which is dependent on the shape of the defect, while crater defects do not.

Acknowledgments

The authors thank M. Balooch and W. J. Siekhaus for their assistance in the AFM work and C. Shang for his assistance with the modeling work.

Notes and References

1. J. R. Murray, J. H. Campbell, D. N. Frank, J. T. Hunt, and J. B. Trenholme, "The Nova Upgrade Beamlet Demonstration Project," *ICF Quarterly Report*, **1** (3) 89, UCRL-LR-105821-91-3 (1991).
2. M. R. Kozlowski, I. M. Thomas, J. H. Campbell, and F. Rainer, "High-Power Optical Coatings for a Mega-Joule Class ICF Laser," *Thin Films for Optical Systems*, (SPIE—The International Society for Optical Engineering, Bellingham, WA, 1992; *Proc. SPIE* **1782**), p. 105.
3. L. F. Johnson, E. J. Ashley, T. M. Donovan, J. B. Franck, R. W. Woolever, and R. Z. Dalbey, "Scanning Electron Microscopy Studies of Laser Damage Initiating Defects in ZnSe/ThF_4 and SiH/SiO_2 Multilayer Coatings," *Laser Damage in Optical Materials: 1984*, NBS Special Pub. **727**, 1984, p. 356.
4. M. R. Kozlowski, M. Staggs, M. Balooch, R. Tench, and W. Siekhaus, "The Surface Morphology of As-Deposited and Laser-Damaged Dielectric Mirror Coatings Studied In-Situ by Atomic Force Microscopy," *Scanning Microscopy Instrumentation: 1991* (SPIE—The International Society for Optical Engineering, Bellingham, WA, 1992; *Proc. SPIE* **1556**).
5. D. Rugar and P. Hansma, "Atomic Force Microscopy," *Physics Today*, 23, Oct. 1991.
6. C. R. Wolfe, M. R. Kozlowski, J. H. Campbell, F. Rainer, A. J. Morgan, and R. P. Gonzales, "Laser Conditioning of Optical Thin Films," *Laser Damage in Optical Materials: 1989*, (SPIE—The International Society for Optical Engineering, Bellingham, WA, 1990; *Proc. SPIE* **1438**), p. 360.
7. D. H. Gill, B. E. Newnam, and J. Mcleod, "Use of non-quarter-wave designs to increase the damage resistance of reflectors at 532 and 1064 nm," *Laser Induced Damage in Optical Materials: 1977*, NBS Spec. Pub. **509**, 1977, p. 260.
8. N. Bloembergen, "Role of cracks, pores, and absorbing inclusions on laser induced damage thresholds at surfaces of transparent dielectrics," *Appl. Opt.*, **12**, 661, 1973.
9. M. A. Schildbach, R. J. Tench, M. Balooch, W. J. Siekhaus, "Scanning Tunneling Microscope Observations of Pulsed Laser Modification of the Basal Plane of Graphite," *Mater. Lett.* **13**, 169, 1992.
10. R. J. Tench, M. A. Schildbach, M. Balooch, W. J. Siekhaus, A. Tesar, "In Situ Scanned Probe Studies on Site Specificity of Laser Surface Damage of Graphite, Sapphire, and Multilayer Coatings," Engineering Foundation Conference Proceedings, *Scanned Probe Microscopies: STM and Beyond*, K. Wickramasinghe Ed., (*AIP Conference Proceedings* **241,** Santa Barbara, 1992) p. 492.
11. A. A. Tesar, M. Balooch, K. W. Shotts, W. J. Siekhaus, "Morphology and Laser Damage Studies by Atomic Force Microscopy of e-Beam Evaporation Deposited AR and HR Coatings," *Laser-Induced Damage in Optical Materials: 1990*, SPIE—The International Society for Optical Engineering, Bellingham, WA, 1991; *Proc. SPIE* **1441**), p. 228.
12. B. Liao, D. J. Smith, and B. McIntyre, "The formation and development of nodular defects in optical coatings," *Laser Induced Damage in Optical Materials: 1985*, NBS Special Publication **746**, 1985, p. 305.
13. D. J. Smith, "Modeling of Nodular Defects in Thin Films for Various Deposition Techniques," *Modeling of Optical Thin Films*, (SPIE—The International Society for Optical Engineering, Bellingham, WA, 1987; *Proc. SPIE* **821**), p. 120.
14. R. Chow, S. Falabella, G. E. Loomis, F. Rainer, C. J. Stolz, and M.R. Kozlowski,"Reactive evaporation of low defect density hafnia," *Laser-Induced Damage in Optical Materials: 1992*, (SPIE—The international Society for Optical Engineering, Bellingham, WA, 1993; *Proc. SPIE* **1848**).
15. S. A. Letts, D. W. Myers, and L. A. Witt, "Ultrasmooth plasma coatings for fusion targets," *J. Vac. Sci. Tech.*, **19** (3), 736 (1981).
16. M. C. Staggs, M. Balooch, M. R. Kozlowski, and W. J. Siekhaus, "In Situ Atomic Force Microscopy of Laser-Conditioned and Laser-Damaged HfO_2/SiO_2 Dielectric Mirror Coatings," *Laser-Induced Damage in Optical Materials: 1991*, (SPIE—The International Society for Optical Engineering, Bellingham, WA, 1991; *Proc. SPIE* **1624**), p. 375.
17. M. C. Staggs, M. R. Kozlowski, W. J. Siekhaus, and M. Balooch, "Correlation of damage threshold and surface geometry of nodular defects in HR coatings as Determined by In-Situ Atomic Force Microscopy," *Laser Induced Damage in Optical Materials: 1992*, (SPIE—The International Society for Optical Engineering, Bellingham, WA, 1992; *Proc. SPIE* **1848**).
18. J. F. DeFord, G. D. Craig, and R. R. McLeod, "The AMOS (Azimuthal Mode Simulator) code," *Proceedings of the 1989 Particle Accelerator Conference*, (IEEE, NY,NY, **89CH2669-0**, 1989) p. 1181.
19. J. DeFord and M. R. Kozlowski, "Modeling of electric field enhancements at nodular defects in dielectric multilayer coatings,"*Laser Induced Damage in Optical Materials: 1992*, (SPIE—The International Society for Optical Engineering, Bellingham, WA, 1993; *Proc. SPIE* **1848**).

TECHNIQUES FOR MBAR TO NEAR-GBAR EQUATION-OF-STATE MEASUREMENTS WITH THE NOVA LASER

R. Cauble
L. B. Da Silva
S. G. Glendinning
S. M. Lane
T. S. Perry
D. W. Phillion

Introduction

Much of the work at the Nova laser involves matter that is subjected to strong shock waves, which can compress the material to pressures of hundreds of megabars. Direct illumination of metals by a Nova-class terawatt laser beam can produce pressures of nearly 100 Mbar.[1] Gigabar pressures are predicted in spherically compressed capsules typical of ICF targets.[2] The equation of state (EOS) largely describes how a material reacts to pressure. Thus, the thermodynamics and hydrodynamics of these systems cannot be predicted without a knowledge of the EOS for this pressure regime. In the limit of extremely high pressures, the EOS is described by a Thomas–Fermi model; for metals, this model is expected to become valid only well into the gigabar regime.[3] Unfortunately, EOS data are sparse at pressures above ~3–4 Mbar because of the combined difficulty of producing such high pressures and measuring the relevant parameters.

We are developing three techniques that should allow us to obtain EOS data in the megabar and near-gigabar regimes. All three use Nova as the driving source to produce intense shocks in materials. The shock is transient; all measurements must be made in a short time (of order tens of picoseconds) after passage of the shock front. A primary objective of this work is to produce spatially large, planar shocks. Use of a convergent geometry to increase pressure makes measurements very difficult. Further, if the shock is not planar, results must be inferred through multidimensional computer codes, so that the data then depends on a correct code description (which itself must use an unmeasured EOS). The shock must be spatially large enough that the data are unambiguous: intense shocks can be generated by focusing a laser beam to a very small spot, but then side motion and likely development of plasma instabilities require multidimensional modeling. A large spatial extent also allows any nonplanarities in the shock to be observed and corrected for.

EOS Data from Hugoniot Measurements

The equation of state is a thermodynamic relation that closes the hierarchy of hydrodynamic equations: conservation of mass, momentum, and energy. Applied to an ideal shock moving at speed D through a material of known initial mass density ρ_0, particle speed u_0, pressure P_0, and internal energy E_0, these conservation relations yield[4]

$$\rho(D-u)=\rho_0 D \quad ,$$

$$P=P_0+\rho_0 u D \quad ,$$

$$E=E_0+\frac{1}{2}(P+P_0)\left(\frac{1}{\rho_0}-\frac{1}{\rho}\right) \quad , \qquad (1)$$

where ρ, u, P, and E are the corresponding quantities in the material after the shock has passed. These three equations, with five unknowns, describe a Hugoniot, a track in the EOS followed by a material as it is compressed. Generally the shock speed can be measured in an experiment. If the shock speed and the EOS of the material is known, say, as the relation $P = P(E, \rho)$, Eqs. (1) can be solved for the remaining unknowns. Conversely, if a second unknown (besides D) can be measured, the Hugoniot of the material can be mapped out. Hugoniots are extremely important in themselves, because they describe how materials behave when shocked, but they also serve as baselines for models of much of the thermodynamic space covered by the full EOS.[5] The aim of our experimental program is to obtain Hugoniot data at high material pressures by measuring that second unknown which, as described below, is *u*, the matter speed behind the shock. So far, however, much of our effort has been directed toward verifying conditions in the experiments, validating our techniques, and measuring the shock speed accurately.

Directly Driven High-Pressure Shocks

There is a long history of attempts to produce very strong shocks in materials by direct irradiation with lasers.[1,6–8] Although inferred pressures were high (2 to ~100 Mbar), many experiments involved relatively low-power laser beams focused to small spot sizes and, as described in the Introduction, concomitant difficulties of interpretation. Even experiments with high-power lasers suffered from uneven laser footprints. Uneven deposition can lead to hot spots and consequent generation of high-energy electrons, penetrating radiation, and hydrodynamic instability. Since Nova has the necessary power, the solution is to smooth the beam.

A smoothed far-field laser spot can be produced with the use of a random phase plate.[9,10] We have used a plate with hexagonal elements 3 mm in diameter, producing a far field that is nearly an Airy pattern with a 1-mm zero-to-zero diameter and a characteristic speckle size of 6 μm. Since such a sharply peaked distribution would not provide the desired planar conditions, steering wedges were also used. The wedges steer different parts of the beam in the near field to different spots in the focal plane to produce a more flat-topped distribution.[11] Figure 1 shows typical images of smoothed and unsmoothed far fields.

Using phase plates and steering wedges on a 1-ns Nova beam provides an intensity of ~3 × 10^{14} W/cm^2 of 2ω light in a focal spot more than 1 mm in diameter with an envelope uniformity of ± 10% over the spot diameter on scales >100 μm. We have used such a beam to irradiate a 25-μm-thick, 0.5-mm-diam Al disk target. The back of the disk (away from the beam) was imaged onto a UV streak camera. Figure 2 shows the setup and a typical streak image. The space across the back of the disk is in the horizontal direction on the image, and time runs vertically; the shock clearly breaks out across the disk with very little tilt or curvature. In fact, the shock breakout time varies across the entire diameter by less than 20 ps (the transit time through the 25 μm of Al is 650 ps), implying that the shock is extremely planar across the disk—by less than 1°. The inferred pressures in the shocked targets are 20–30 Mbar.

In spite of these excellent results, the smoothed beam does have intensity variations on the order of the speckle size; the small speckles can have intensity modulations as high as 10 times the average intensity. Such areas of high intensity can produce x rays of energy high enough to penetrate into the cold material, even when the front surface is coated with 2 μm of CH as a laser burnthrough barrier. We are planning experiments in which high magnification XUV sidelighting will be used to determine whether such preheating is causing premature expansion of the target.

Indirectly Driven Colliding Foil Experiments

We have seen that we can generate pressures of tens of megabars over ~1 mm spot size by direct illumination with a kilojoule laser. To reach much higher pressures

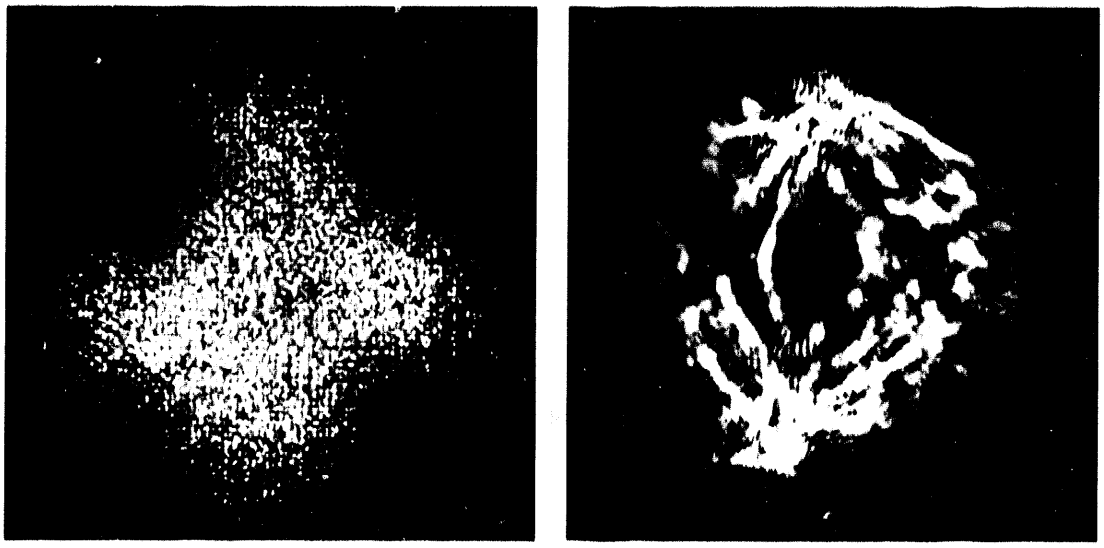

FIGURE 1. Far-field focal spot of one Nova beam with and without beam smoothing (accomplished with a random phase plate and steering wedges). On scales >100 μm, the smoothed beam suffers intensity variations of only ±10%, while variations of more than factor of 10 are typical in the unsmoothed beam.

without sacrificing spot size (and thus one-dimensionality), we use a variation and miniaturization of the well-known flyer-plate technique.[12, 13] In this method, the flyer (in our case, a foil) stores kinetic energy from the driver over an acceleration time and delivers it much more rapidly as thermal energy in collision with another foil. The flyer also acts as a preheat shield so that the target remains on a lower adiabat than if it were exposed to the driver. These attributes make it possible to achieve much higher pressures using a flyer-impact configuration than with a directly driven configuration. This technique has been demonstrated using a laser as a driver[14]; pressures of over 100 Mbar have been achieved.[15]

Several problems must be overcome when using this technique. First, if a laser is to be used as a driver, the laser beam must be spatially uniform to avoid breakup of the flyer foil. Second, penetrating radiation can be produced by the high laser intensity required to drive the foil.[15] Third, high driver intensities require small laser spot sizes. Fourth, a flyer foil directly irradiated by the laser is prone to Rayleigh–Taylor instability. If the instability is not avoided (for example, by using an ablator[16]), the acceleration distance between flyer and target foils must be kept short enough so that the instability has little time to grow. To circumvent these problems, we have performed a set of experiments with a high-intensity x-ray drive that is uniform over a circle about 0.5 mm in diameter. The x rays, produced by focusing the ten beams of the Nova laser into a millimeter-scale gold hohlraum, accelerate a foil that then collides with a stationary foil, producing pressures of over 700 Mbar in a planar shock.[17]

Figure 3 shows the experimental arrangement. The hohlraum x rays ablate a 50-µm layer of polystyrene attached to a 3-µm-thick gold foil. The foil accelerates through a 50-µm void region and, near the end of the laser pulse, collides with and launches a compression wave into a stationary gold target foil made of two

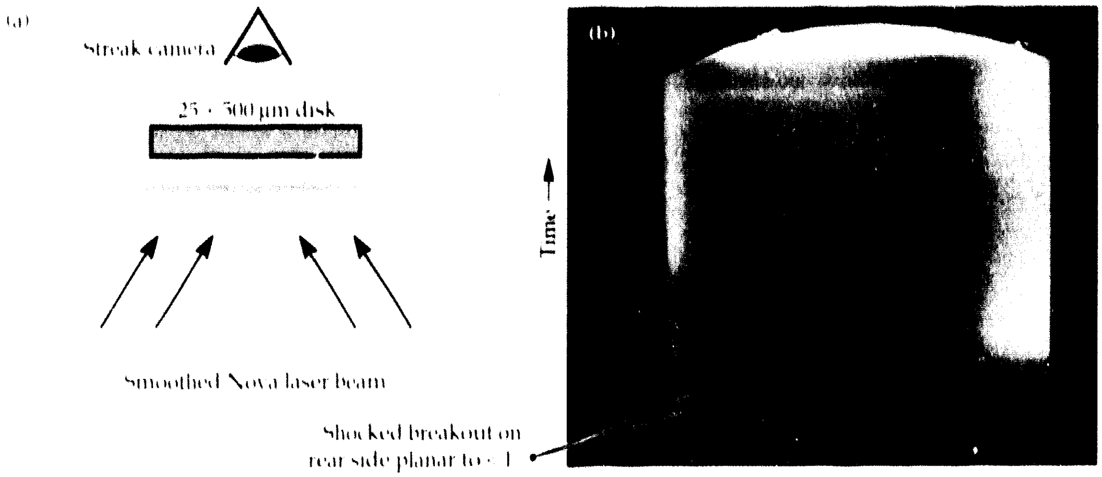

FIGURE 2. (a) Arrangement of direct-drive shock experiment. (b) Image from the diagnostic showing an extremely planar shock emerging from the rear of the target.

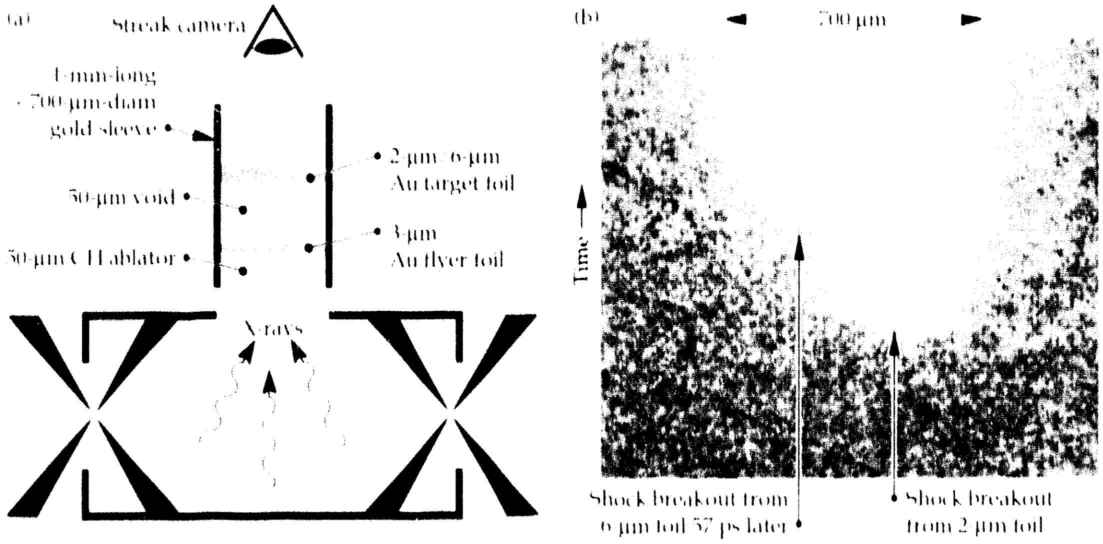

FIGURE 3. (a) Arrangement of indirect-drive colliding foil arrangement (not to scale). The 1-mm-long × 700-µm-diam experimental package faces the hohlraum x-ray drive. The package comprises a 50-µm CH ablator on a 3-µm Au flyer foil, a 50-µm void, and a Au target foil with a 4-µm step, all held in a gold sleeve. (b) Data image showing shock breakouts 57 ps apart, corresponding to a shock speed of 70 km/s.

thicknesses (2 and 6 µm, giving a 4-µm step). When the shock breaks out on the back side of the target foil, the high-temperature material is imaged onto a streaked optical pyrometer.[18] The cylindrical experimental packages were 0.5 and (later, to reduce edge effects) 0.7 mm in diameter, and were mounted across a hole in the wall of the hohlraum with the ablator facing the interior of the hohlraum. The approximately 100-µm-long target assembly was placed at the bottom of a 1-mm gold sleeve so that the assembly was completely shielded from unfocused, unconverted laser light. Additional shielding prevented the diagnostic from viewing heated areas of the sleeve and the hohlraum.

A typical streak camera image (Fig. 3) shows shock breakout at two times, corresponding to the two target foil thicknesses; the step height and the time interval between the breakout times together determine the shock speed in the target if the shock speed is constant. Here, the interval between shock breakouts is 57 ± 5 ps, corresponding to an average shock velocity of 70 ± 6 km/s. The SESAME equation of state tables[19] indicate that this shock speed corresponds to a density of 90 g/cm^3 and a pressure of 0.74 Gbar in the gold target.

Any slight spatial imbalance in the drive or any unexpected edge effects (due, e.g., to interactions between the flyer foil and the sleeve) could cause the flyer to tilt or curve, which would drive a nonplanar shock into the target and compromise the simulation-free (1-D) interpretation. However, because of the relatively large diameter of the foils, any nonplanarity in shock breakout is observable. In addition, the step in the target was at the center of the large foil, where the effects of edge-induced nonuniformities are minimized. For example, the streak image in Fig. 3 indicates that shock speed decreases toward the far left-hand side but is constant in the central portion.

Data were obtained on four shots in which measured shock speeds implied pressures of 0.65 to 0.83 Gbar. The largest single unknown is preheating of the target foil before the flyer–target collision; if this occurs, the 2-µm side of the target will have a higher energy density than the 6-µm side. In this case, enough mass near the surface of the 2-µm side could lift off to significantly alter the interpretation of the measurements: mass ablating off the back side of the target foil effectively makes the 2-µm side thicker, so that the shock on that side breaks out later. The shortened measured interval time would imply a higher pressure in the target.

Given the mass of material (ablator and flyer) between the drive source and the target foil, target preheat could only arise from high-energy x rays in the drive spectrum. To test this possibility, we reduced the intensity of high-energy x rays (>2.5 keV) by more than a factor of 5, but kept the overall drive intensity the same as in the three previous experiments. The resulting shock speed was essentially unchanged, so we do not believe that preheat affects our results.

Hydrodynamics simulations indicate that the bulk of the flyer should decompress from its initial density of 19.3 g/cm^3 to approximately 10 g/cm^3 before impact. The simulations also indicate that the 6-µm target foil is thin enough that the shock does not decay significantly as it transits the target foil. While the simulation results obviously depend on code parameters, zoning requirements, and input data tables, and the connection between shock speed and material pressure requires the assumption of an EOS, the simulations predict the bulk hydrodynamic properties of these experiments well.

Measuring a Second Unknown

In the shots discussed above, we demonstrated that material pressures of >0.7 Gbar could be produced by the colliding-foil method. A straightforward extension of this technique can be made to obtain EOS data in this regime. If the flyer foil can be shielded so that it does not significantly heat or decompress (we have not demonstrated this), data points on the Hugoniot can be found by measuring the flyer speed, from which u can be determined.[11] Flyer speed can be obtained by recording shock breakouts from two identical foils placed at different distances along the flyer path; this is in effect accomplished by modifying the target foil as shown in Fig. 4. The large diameter and one-dimensional nature of the experiment make this arrangement practicable.

To test the feasibility of this technique, we performed one experiment with a two-step Au target foil. Although the condition of the flyer foil was unknown, so that we could not evaluate a Hugoniot data point, we observed three shock breakouts, indicating the viability of the approach. If the behavior of the flyer during ablative acceleration can be characterized and controlled, this technique should yield Hugoniot data for gold at pressures in the near-Gbar regime.

Indirect-Drive Hugoniot Experiments on Polystyrene

Plastics are very different materials than aluminum or gold, but they are just as pervasive in ICF experiments as major constituents of spherical-capsule targets. Since plastics, unlike metals, are largely transparent to high-energy x rays, x rays can be used to backlight relatively thick samples of polystyrene ("CH"), providing information on the sample as a function of time. In particular, the shock front in a sample of CH can be seen on a streak camera by simultaneously imaging the transmission of an x-ray backlighter through the shocked and unshocked material; the transmissivity of the denser shocked CH is significantly less than that of normal-density CH (about 70% less for a compression of 4 in a 0.7-mm-thick sample at a 7-keV backlighter energy). If, at the same time, motion of the material behind the shock can also be imaged, Eqs. (1) can be solved and a data point on the Hugoniot obtained.

Figure 5 shows an experimental arrangement that accomplishes this. The material motion behind the shock [*u* in Eqs. (1)] is viewed as the difference in transmission of the backlighter through doped and undoped shocked CH; this is the interface shown in the figure. Again, the x-ray drive is provided by a hole in the side of a gold hohlraum. Here only eight Nova beams are used for the drive, saving two beams for the backlighter. The arrangement was adapted from an experiment used to measure material mixing at interfaces.[20] (In the mix experiment, the region of undoped CH in Fig. 5 is replaced by a material of much lower density than the doped CH region; material mixing occurs at this interface. Figure 5 in effect shows the "null" mix experiment, in which no mixing is expected because the interface separates regions of nearly equal density.)

Since the shock decays as it traverses the doped CH, the pressure in the vicinity of the interface can be varied from ~1 to ~40 Mbar, depending on distance from the hohlraum (that is, on the length of the doped CH ablator section). Two shots were performed with 2 at.% Br doped into the first section, which was 300 μm long. A 3-ns-long backlighter beam was turned on at about the time the shock was expected to pass through the interface. It is important to determine the speed of the shock as it passes through the interface, and the speed of the interface immediately after shock passage, because the shock and interface speeds will probably decay at different rates. The interface was clearly visible on the streak records, but the shock front was too weak to be seen. Both shock and interface were seen in one of the mix experiments, but there the backlighter was turned on several nanoseconds after the shock passed through the interface. Thus, we believe that this technique will allow us to obtain Hugoniot data on CH in the megabar regime; different dopants and backlighter energies will be used to increase the shock and interface contrasts.

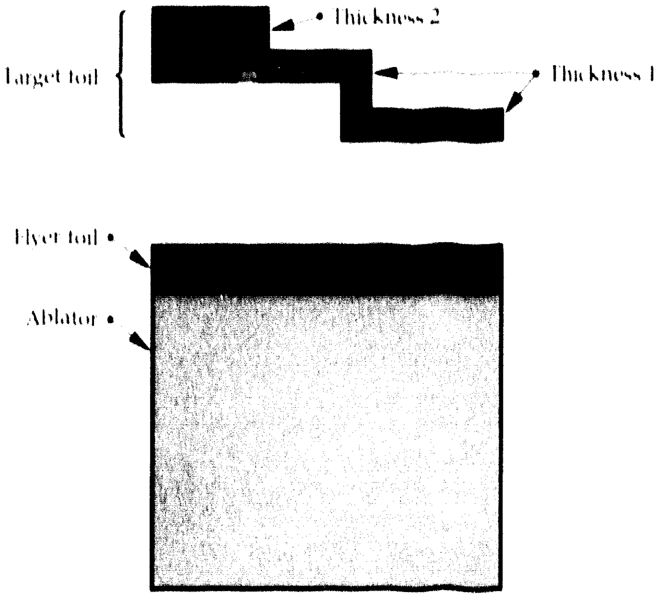

FIGURE 4. Target foil configuration for simultaneous measurement of shock speed *D* and of flyer speed, from which material speed *u* behind the shock can be inferred. These two measurements will determine a point on the Hugoniot in the gigabar regime.

Summary

We can produce extremely planar shocks in the 10–30 Mbar regime by direct illumination of metals with highly smoothed Nova laser beams. Using flyer foils driven by x-ray emission from hohlraums driven by Nova, we have obtained the first directly measured shock speeds indicating pressures of over 100 Mbar (indeed, over 700 Mbar) in the laboratory. The target foil was unaffected by preheat, and its large size made

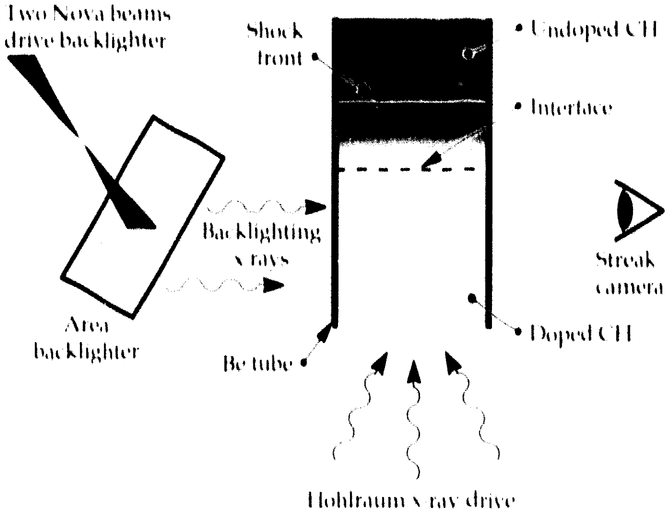

FIGURE 5. Arrangement for indirect-drive Hugoniot experiments in transmissive media such as CH, showing package (mounted across a hohlraum), backlighter, and streak camera. Differences in transmission of the backlighter through the package will allow measurement of shock speed and speed of interface between doped and undoped CH. These two measurements will determine a point on the Hugoniot in the megabar regime.

small two-dimensional effects observable. This technique can be readily applied to provide primary data on the equation of state of matter in the gigabar regime. We are pursuing another technique that will allow us to directly measure Hugoniot data for CH in the megabar regime.

Acknowledgments

This work benefited from numerous discussions with D. L. Griswold, B. A. Hammel, N. C. Holmes, T. J. Hoover (DNA), J. D. Kilkenny, R. W. Lee, P. L. Miller, T. A. Peyser, and J. Wark (Oxford University).

Notes and References

1. J. D. Kilkenny, "Ablation Pressure Measurements at 0.35 µm," in *Laser Program Annual Report 1986*, Lawrence Livermore National Laboratory, Livermore, CA, UCRL-50021-86 (1987), pp. 3-6 to 3-9.
2. J. D. Lindl, R. L. McCrory, and E. M. Campbell, "Progress Toward Ignition and Burn Propagation in Inertial Confinement Fusion," *Physics Today* **45** (9), 32 (1992).
3. A. V. Bushman and V. E. Fortov, "Model Equations of State," *Sov. Phys. Usp.* **26**, 465 (1984).
4. Ya. B. Zel'dovich and Yu. P. Raizer, *Physics of Shock Waves and High-Temperature Hydrodynamic Phenomena* (Academic Press, New York, 1967), Vol. I, p. 46.
5. L. V. Al'tshuler, "Use of Shock Waves in High-Pressure Physics," *Sov. Phys. Usp.* **8**, 52 (1965).
6. L. R. Veeser and J. C. Solem, "Studies of Laser-Driven Shock Waves in Aluminum," *Phys. Rev. Lett.* **40**, 1391 (1978).
7. R. J. Trainor, J. W. Shaner, J. M. Auerbach, and N. C. Holmes, "Ultrahigh-Pressure Laser-Driven Shock-Wave Experiments in Aluminum," *Phys. Rev. Lett.* **42**, 1154 (1979).
8. F. Cottet, J. P. Romain, R. Fabbro, and B. Faral, "Ultrahigh-Pressure Laser-Driven Shock-Wave Experiments at 0.26 µm Wavelength," *Phys. Rev. Lett.* **52**, 1884 (1984).
9. S. Skupsky, R. W. Short, T. Kessler, R. S. Craxton, S. Retzring, and J. M. Soures, *J. Appl. Phys.* **66**, 3456 (1989).
10. K. Mima, N. Miyanaga, S. Arinaga, Y. Kitagawa, M. Nakatsuka, and C. Yamanaka, "Random Phasing of High-Power Lasers for Uniform Target Acceleration and Plasma-Instability Suppression," *Phys. Rev. Lett.* **53**, 1057 (1984).
11. X. Deng, X. Liang, Z. Chen, W. Yu, and R. Ma, "Uniform Illumination of Laser Targets using a Lens Array," *Appl. Opt.* **25**, 377 (1986).
12. L. V. Al'tshuler, K. K. Krupnikov, B. N. Ledenev, V. I. Zhuchikhin, and M. I. Brazhnik, "Dynamic Compressibility and Equation of State of Iron under High Pressure," *Sov. Phys. JETP* **7**, 606 (1958).
13. Ya. B. Zel'dovich and Yu. P. Raizer, *Physics of Shock Waves and High-Temperature Hydrodynamic Phenomena* (Academic Press, New York, 1967), Vol. II, p. 724.
14. S. P. Obenschain, R. R. Whitlock, E. A. McLean, B. H. Ripin, R. H. Price, D. W. Phillion, E. M. Campbell, M. D. Rosen, and J. M. Auerbach, "Uniform Ablative Acceleration of Targets by Laser Irradiation at 10^{14} W/cm^2," *Phys. Rev. Lett.* **50**, 44 (1983).
15. R. Fabbro, B. Faral, J. Virmont, H. Pepin, F. Cottet, and J. P. Romain, "Experimental Evidence of the Generation of Multi-hundred Megabar Pressure in 0.26 µm Wavelength Laser Experiments," *Laser Part. Beams* **4**, 413 (1986).
16. S. E. Bodner, "Rayleigh-Taylor Instability and Laser-Pellet Fusion," *Phys. Rev. Lett.* **33**, 761 (1974); J. D. Lindl and W. C. Mead, "Two-dimensional Simulation of Fluid Instability in Laser-Fusion Pellets," *Phys. Rev. Lett.* **34**, 1273 (1975).
17. R. Cauble, D. W. Phillion, T. J. Hoover, N. C. Holmes, J. D. Kilkenny, and R. W. Lee, "Demonstration of 0.75 Gigabar Shocks in X-ray Driven Colliding Foils," *Phys. Rev. Lett.* **70**, 2102 (1993).
18. V. W. Slivinsky and R. P. Drake, "Nova Diagnostics Summary," *Laser Program Annual Report 1984*, UCRL-50021-84 (1985), pp. 5-89 to 5-91.
19. "T-4 Handbook of Material Properties Data Bases: Vol. Ic, Equations of State," K. S. Holian, Ed., Los Alamos National Laboratory, Los Alamos, NM, LA-10160-MS (November, 1984).
20. B. A. Hammel, D. L. Griswold, O. L. Landen, T. S. Perry, B. A. Remington, J. D. Kilkenny, and R. Pasha, "X-ray Radiographic Measurements of Radiation Driven Shock and Interface Motion in Solid Density Material," Lawrence Livermore National Laboratory, Livermore, CA, UCRL-JC-111933 (1993); to be published in *Phys. Fluids*.

PARAMETRIC INSTABILITIES AND LASER-BEAM SMOOTHING

H. A. Baldis *S. Dixit*
J. D. Moody *R. L. Berger*
D. S. Montgomery *B. F. Lasinski*
C. Labaune[*] *K. Estabrook*

Introduction

The study of parametric instabilities in laser plasmas is of vital importance for ICF. The long scale length, low-density plasma surrounding an ablatively imploded fusion target provides ideal conditions for the growth of instabilities such as stimulated Brillouin scattering (SBS), stimulated Raman scattering (SRS), and filamentation.[1,2] The scattering instabilities (SBS and SRS) can produce a significant loss of incident laser energy and can modify the light distribution around the target. The filamentation instability can generate high laser intensities in very localized regions that can modify the plasma and laser intensity conditions. These effects can lead to detrimental results for ICF.

The scattering instabilities occur through the resonant decay of an incident electromagnetic (EM) wave into a scattered EM wave and a local plasma mode. This mode is either an ion acoustic wave (IAW) in the case of SBS, or an electron plasma wave (EPW) in the case of SRS. Resonant coupling of three waves implies that the frequency and wave numbers of the waves are related as:

$$\omega_0 = \omega_s + \omega_a$$

and

$$k_0 = k_s + k_a \ . \qquad (1)$$

where ω_0 (ω_s) and k_0 (k_s) are the frequency and wave number of the incident (scattered) EM wave, and ω_a (k_a) is the frequency (wave number) of either the IAW or the EPW. The scattering instabilities result from a feedback loop by which the beating between the incident and scattered EM waves matches the frequency and wave number of a local longitudinal (electrostatic) normal mode of the plasma. When the local laser intensity is above a threshold (determined by wave damping and plasma gradients), and the resonant coupling conditions are satisfied, the instability grows exponentially until saturation.

The effect of laser-beam smoothing techniques[3,4] on parametric instabilities is of particular interest. These techniques can suppress hydrodynamic instabilities by improving irradiation uniformity. Laser-beam smoothing techniques also have the potential to control the scattering level from parametric instabilities since they produce a smoother laser intensity distribution as well as reduce the temporal beam coherence. Beam smoothing techniques that affect the growth of parametric instabilities include spatial smoothing and temporal smoothing.

Spatial smoothing breaks the beam up into fine-scale structures by modifying the phase fronts and spatial distribution of intensities in the incident laser focal volume. Laser beam nonuniformities can produce a focal spot consisting of several high intensity regions that are many times the diffraction limited size. The exact characteristics of the focal spot depend on the details of the laser system. An example of the Nova laser focal spot is shown in Fig. 1(a). The introduction of random phase plates (RPPs) in the beam produces a laser spot that is uniform on the large scale [shown in Fig. 1(b) for the Nova laser]. Spatial smoothing reduces the spectral intensity in the lower spatial wave numbers. This reduction is predicted to limit significantly the growth of filamentation. RPPs have the additional advantage of producing a focal spot with a well known (negative exponential) intensity distribution.

Temporal smoothing rapidly varies in time the fine-scale speckle structure produced by an RPP. Converse to spatial smoothing, temporal smoothing limits the

---

[*] Ecole Polytechnique, Paris, France

growth time of an instability by reducing the coherence time of the laser. Laser bandwidth is required for temporal smoothing.

Recent theoretical studies[5,6] have examined the effect of spatial and temporal smoothing on the growth of SRS and SBS. In 1984 at Osaka University, Kato et al.[7] proposed spatial smoothing using an RPP. Earlier in 1983, Lehmberg and Obenschain[8] at the Naval Research Laboratory (NRL) introduced a combined spatial and temporal smoothing technique called induced spatial incoherence (ISI), which they later implemented in 1985. In 1989, Skupsky et al.[9] at the University of Rochester's Laboratory for Laser Energetics demonstrated a method employing bandwidth and RPP called smoothing by spectral dispersion (SSD).

In NRL studies using the ISI technique, the levels of backscattered light from SBS and SRS were reduced for a plasma produced by spatially and temporally incoherent laser light.[10,11] Experiments at École Polytechnique[12] using RPP smoothing showed a reduction of approximately two orders of magnitude for both SBS and SRS (for laser intensities $>10^{14}$ W/cm^2). Measurements used to infer filamentation in these same experiments also indicated a reduction in this instability when using an RPP.[13,14] In a similar experiment at Rutherford,[15] the observed reductions of SBS and SRS were attributed exclusively to the reduction of filamentation.

Beam Smoothing on the Nova Laser

The Nova beam is considerably aberrated due to optical inhomogeneities, surface figure errors, and thermal nonuniformities in the large-aperture optical components. Aberrations are also introduced when using segmented optical components in the final amplifier stage. All these aberrations combine to produce beams on Nova that are many times (20–50) diffraction limited and thus highly modulated near the focus. As stated earlier, Fig. 1(a) shows a typical focal plane irradiance profile for one of the Nova beams. Large-scale inhomogeneities produced by the beam aberrations are clearly visible.

The focal plane intensity distribution on Nova is smoothed using RPP and SSD smoothing techniques. An RPP used in Nova experiments consists of regular hexagonal elements randomly chosen to introduce a phase delay of 0 or π in the beam. The far-field intensity distribution of an RPP consists of an overall envelope determined by the far-field of an individual (hexagonal) phase plate element. Within this envelope, there is a fine-scale speckle structure due to the interference between different phase plate element contributions. The RPP element size is chosen to produce an Airy pattern central maximum with a zero-to-zero spot diameter as required for the experiment. (See Refs. 16 and 17 for a detailed discussion of fabrication of the large-aperture RPPs for use on Nova. Figure 1(b) shows a far-field intensity distribution of the Nova beam with the RPP. The intensity distribution is completely homogeneous with very little "imprint" of the Nova beam profile [Fig. 1(a)]. The fine-scale speckle structure is also clearly visible. (The probability distribution of the intensity distribution in the speckle pattern is discussed elsewhere.[16,17])

The speckle pattern produced by the RPP can be smoothed further by using SSD. In the version of SSD implemented on Nova,[4] a broad bandwidth ($\Delta\lambda/\lambda \sim 0.1\%$) pulse is generated by cross-phase modulation in a polarization preserving optical fiber. Following moderate amplification, the pulse is dispersed using a 900 lines/mm reflection grating. The grating is located in a relay plane in the Nova laser chain. The dispersed pulse is further amplified, frequency converted to second harmonic, and focused through the hexagonal element RPP onto the plasma. The amount of bandwidth, along with the dispersion introduced by the grating, implies that an asymptotic smoothing level of about 0.1 (the value of the normalized variance of the time

FIGURE 1. Far-field irradiance pattern for (a) the Nova beam and (b) an RPP-smoothed Nova beam.

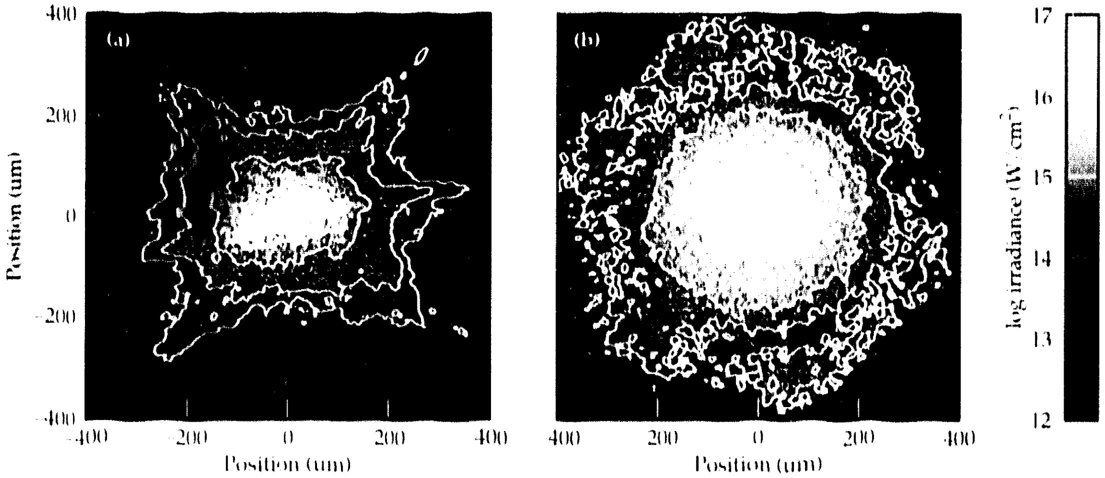

averaged intensity) is achieved within an asymptotic smoothing time of approximately 0.1 ns. SSD achieves this high level of smoothing by overlapping speckle patterns (for each frequency component) that are spatially shifted relative to each other. Time averaging eliminates the interference among these speckle patterns, which produces a smooth beam.

Nova Two-Beam Plasma Physics Experiments

Our recent experiments characterized the effect of beam smoothing on SBS and SRS. The experiments used the Two-Beam Chamber Facility in which one beam preformed a plasma and the second beam interacted with the plasma by exciting instabilities. This arrangement allowed for independent control of the plasma conditions and of the interaction beam. A single Nova arm can provide up to about 8 TW of power at a wavelength of 1054 nm (1ω) for a pulse duration of 1 ns. Frequency conversion KDP crystals can convert the 1054-nm laser light to either 527 nm (2ω) or 351 nm (3ω) with a conversion efficiency of about 40%. To provide uniform illumination on the target, we used an RPP on the plasma-forming laser beam. We used the interaction beam without beam smoothing, with RPP (spatial smoothing), and with SSD (temporal smoothing).

We collected backscattered light from the plasma using the entire Nova focusing lens. We then directed the light by a full-aperture beamsplitter and focusing optics (Fig. 2) to several instruments that measure the temporal and spectral characteristics of this light. One instrument, which uses a high dispersion spectrometer coupled to a streak camera, provided temporally resolved SBS spectra ($\Delta\lambda \approx 3$ Å, $\Delta\tau \approx 50$ ps). A similar instrument, which uses a lower dispersion spectrometer, recorded broadband spectra from SRS emission. This emission, for an interaction beam at 527 nm, had a spectral band between 600 nm and 1054 nm. Other instruments included a photodiode and a calorimeter to measure absolute levels of reflectivity. An array of photodiodes at different locations in the target chamber monitored the angular distribution of the scattered light.

We exploded a foil target with a single Nova laser beam to produce the preformed plasma. The target was a 2.0 ± 0.1-µm thick CH (plastic) disk (1.5 ± 0.1-mm diam) supported on a 700-Å sheet of Formvar. We created the plasma by irradiating one side of the foil with 2.0–2.3 kJ of 351-nm laser light in a 1-ns trapezoidal pulse. The laser intensity had a 0.1-ns rise and fall time and was constant to ± 10% over the peak of the pulse. We focused the preforming beam on target with an $f/4.3$ aspheric lens and spatially smoothed this beam with a 1.3-mm square-element RPP to produce a spot on target with a diameter of 1.4 mm at the first Airy minimum. The preforming beam heated the plasma to an electron temperature of about 2 keV and expanded it rapidly such that the peak electron density fell to 10^{21} cm^{-3} within 0.3–0.4 ns. The critical electron density n_{cr} for 2ω light is 4×10^{21} cm^{-3}.

We controlled the peak electron density present in the plasma at the beginning of the interaction pulse by adjusting the delay between the preforming and interaction beams. An early delay (0.4 ns) means that the interaction beam arrives at a plasma with a peak density of about 0.3 n_{cr}. A late delay (1.1 ns) means that the peak plasma density is slightly below 0.1 n_{cr}.

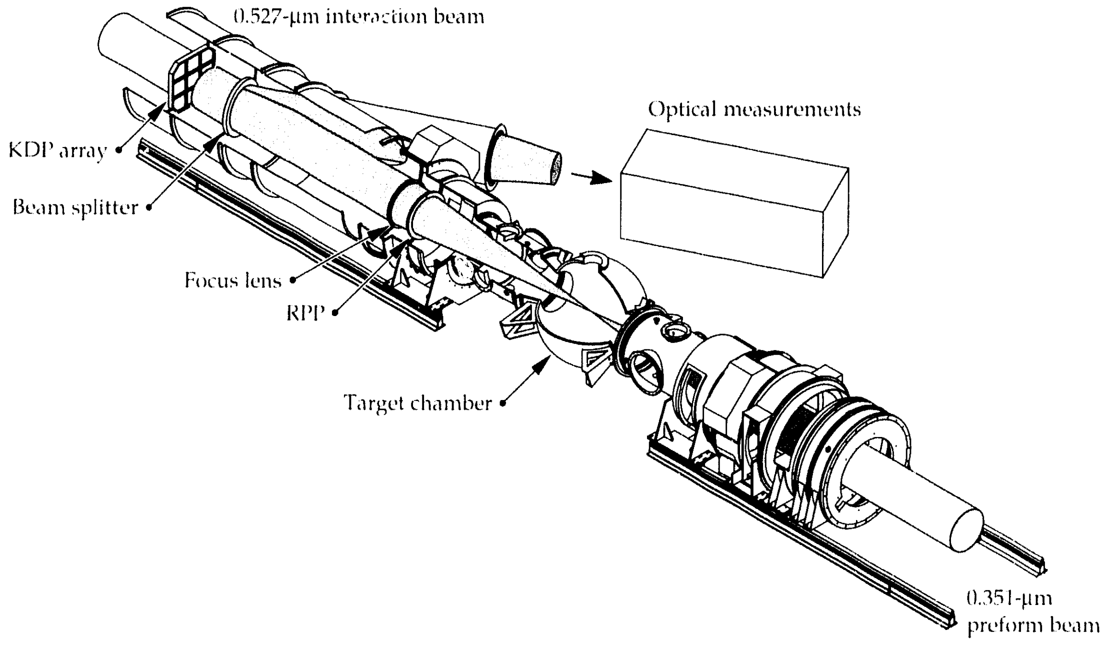

FIGURE 2. Two-beam experimental facility showing the location of the focus lens, the RPP, and the beam splitter used to direct the backscattered light to instruments that measure its temporal, spectral, and energy characteristics.

Information about the peak plasma electron density is inferred from time-resolved spectra of SRS emission. Figure 3(a) shows a typical example of SRS backscattered emission from a CH target. At each point in time, the spectrally resolved emission extends between a short and long wavelength limit. The long wavelength limit corresponds to SRS light emitted at the peak plasma density. The short wavelength limit corresponds to strongly damped SRS (stimulated Compton scattering) where the growth rate becomes negligible. Within this strongly damped regime, the Debye length is comparable to the electron plasma wavelength and strong Landau damping inhibits growth of the SRS instability. We calculated other plasma parameters such as temperature, flow speed, and nonpeak densities using the two dimensional hydrodynamic computer code LASNEX. Figure 3(b) shows a comparison between the time evolution of the peak electron density inferred from SRS emission and the peak electron density obtained from LASNEX. As shown, agreement between the two curves within the experimental and computational uncertainties is quite good. Additional agreement between LASNEX predictions and results from separate experiments suggests that the LASNEX model can provide good predictions of many of the hydrodynamic plasma parameters in the exploding foil plasma.

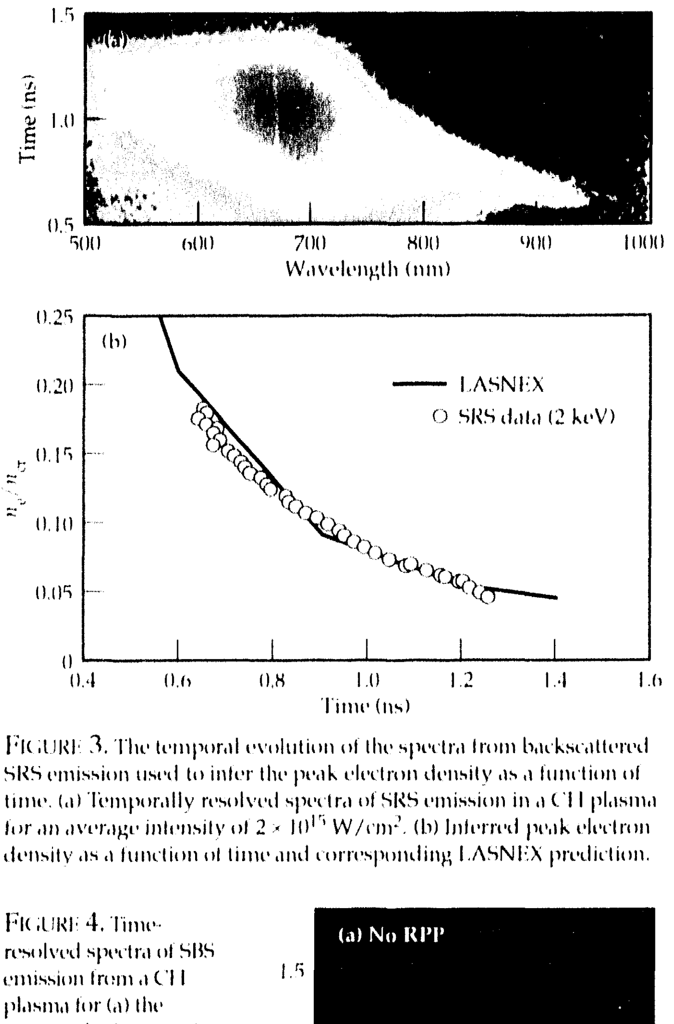

FIGURE 3. The temporal evolution of the spectra from backscattered SRS emission used to infer the peak electron density as a function of time. (a) Temporally resolved spectra of SRS emission in a CH plasma for an average intensity of 2×10^{15} W/cm^2. (b) Inferred peak electron density as a function of time and corresponding LASNEX prediction.

Stimulated Brillouin Scattering Measurements

We characterized the various beam-smoothing techniques by measuring their effects on the SBS emission. Figure 4 shows the time-resolved spectra of SBS emission for a case with (a) no RPP smoothing and (b) only RPP smoothing. Between these cases, we set the laser energy differently in an effort to keep the intensity on target similar. In case (a), the interaction beam energy was about one-third that of case (b) so that the resulting average intensity for the two cases was the same within a factor of two. Both cases showed an initial bright burst of emission for the first 0.1–0.2 ns of the interaction beam. This bright emission quickly decreased to the film noise level in the RPP-smoothed case. For the unsmoothed case, the emission continued for the duration of the interaction pulse and appeared to come in bursts at various times and spectral bands. The total reflectivity in both cases was about 2 to 5% with a peak instantaneous reflectivity near 10%.

FIGURE 4. Time-resolved spectra of SBS emission from a CH plasma for (a) the unsmoothed interaction beam and (b) the interaction beam smoothed with an RPP.

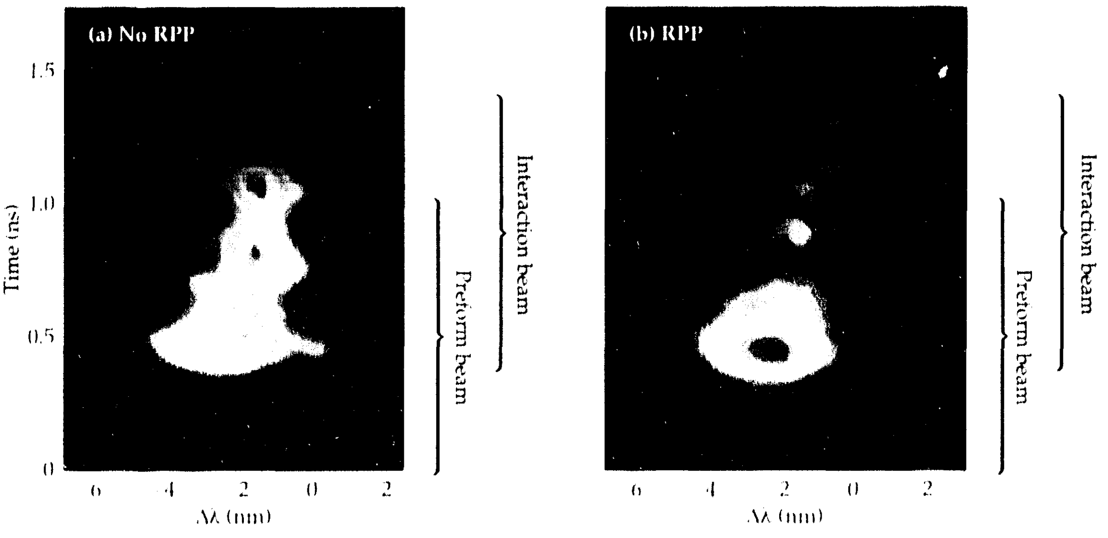

Figure 5 shows the temporal SBS reflectivity as a function of time for RPP and SSD smoothing in moderate-density (0.4-ns delay) and low-density (1.1-ns delay) plasmas. The reflectivities, as a function of time for RPP and SSD smoothing, were within a factor of two at the beginning of the interaction pulse for the moderate-density plasma case. About halfway through the interaction pulse (near 0.8 ns), the emission driven by the SSD beam decreased faster than the emission driven by the RPP beam. At that time, the RPP emission was about a factor of 10 higher than the SSD emission. Near the end of the interaction (1.1 ns), the SBS emission produced by irradiation with the SSD beam was reduced to the limit of detectability. Here, this emission was at least a factor of five lower than that produced by the RPP beam. Using SSD in the low-density (1.1-ns) delay case, there was an overall reduction of about a factor of 30 in the peak SBS emission. In the SSD smoothed case, the emission is both lower in amplitude and shorter in duration. The data in Fig. 5 show that adding bandwidth to the RPP-smoothed interaction beam substantially reduces the SBS emission below the RPP smoothing level only at late times, when the peak electron density is below 0.2–0.25 n_{cr}. Neither smoothing method seems to have much effect when the peak electron density is above 0.2–0.25 n_{cr}.

Our observations show two general features that appear to be characteristic of SBS emission from these exploding foil plasmas. (1) The emission at a particular time depends on the delay of the interaction beam. For example, the RPP emission in Fig. 5 at 1.2 ns is about three times greater when the interaction pulse starts at 1.1 ns than when it starts at 0.4 ns. (2) We observed an overall blue shift in the SBS emission that was smaller for late time interactions. The blue shift of the SBS light is consistent with the Doppler shift expected in the emission from a low-density plasma region that moves toward the observer with an expansion velocity of about 2 to 2.5 Mach numbers (~ 10^8 cm/s).

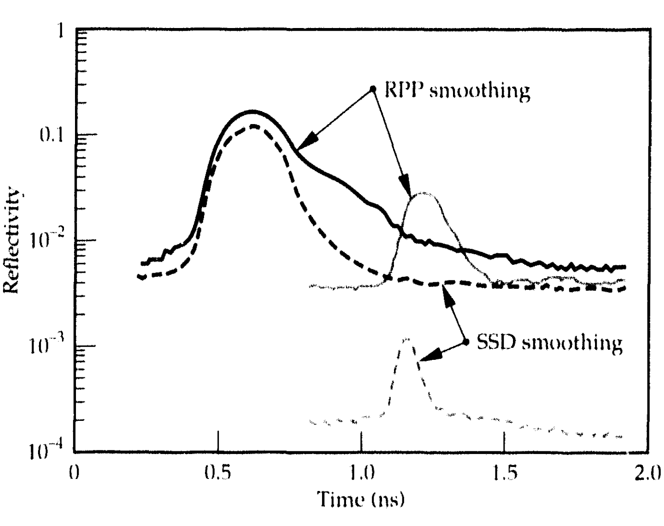

FIGURE 5. Total time-resolved emission from SBS backscattered light in a CH plasma at moderate (early interaction) and low (late interaction) peak electron density with RPP and SSD smoothing.

Stimulated Raman Scattering Measurements

As with SBS, we also characterized the various beam-smoothing techniques according to their effects on SRS emission. Figure 6(a) shows a typical SRS spectrum from an experiment with an average interaction beam intensity of 2.0 × 10^{15} W/cm^2 and no added bandwidth (narrowband). The long-wavelength cutoff

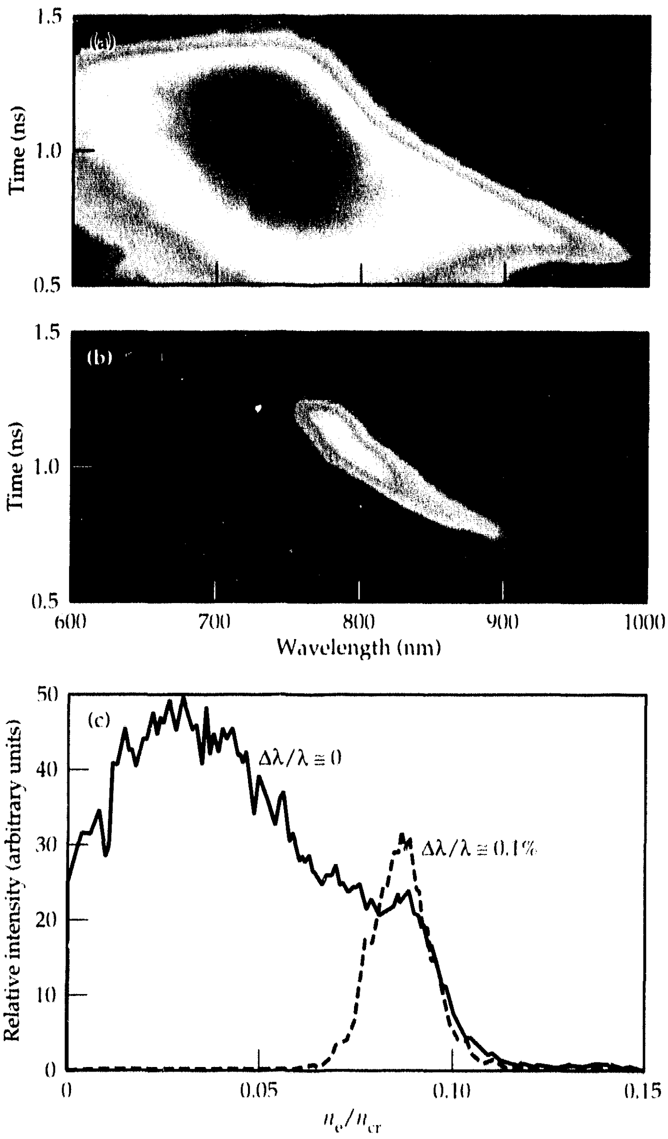

FIGURE 6. Backscattered emission from SRS produced by an interaction beam with (a) RPP smoothing and (b) SSD smoothing. (c) The emission vs electron density at 0.95 ns into the preformed pulse for (a) and (b).

of the SRS spectrum decreases with time and is consistent with plasma expansion for exploding-foil targets. The SRS spectrum [Fig. 6(a)] is quite broad and is typical for large-scale laser plasmas with high intensity and no temporal smoothing. Figure 6(b) shows the SRS spectrum for a laser intensity of 1.2×10^{15} W/cm^2, using bandwidth $\Delta\lambda/\lambda \sim 0.1\%$ for temporal smoothing. The spectrum is narrow and is significantly different from the spectrum shown in Fig. 6(a). We believe that these effects are due to temporal smoothing and not to the bandwidth itself, since we used very small bandwidth in these experiments compared to the growth rate for SRS. Figure 6(c) shows spectral profiles at 1 ns for the cases with and without bandwidth; the peak electron density was about 0.1 n_{cr}. The profile for the narrowband case had a maximum emission at a wavelength that corresponded to a density of 0.05 n_{cr}(λ = 740 nm), and emission from lower densities was observed. As shown in Fig. 6(c), the SRS spectral profile for $\Delta\lambda/\lambda \sim 0.1\%$ was narrow and occurred over a density range of 0.08–0.1 n_{cr}. The level of SRS emission in the range of 0.09–0.1 n_{cr} was similar for cases with and without bandwidth, but the emission below 0.09 n_{cr} was significantly reduced with bandwidth. The emission below 0.09 n_{cr} dropped below the detection threshold with temporal smoothing (or about a factor of 50). The SRS backscattering fraction, estimated from the photodiodes for the $\Delta\lambda/\lambda \sim 0$ case, was 3–5%. Comparing the integrated spectra, the total SRS reflectivity dropped only by a factor of 5–10 with SSD, since emission still occurred near the peak plasma density. Narrowband experiments were also performed with a lower interaction beam intensity of 10^{14} W/cm^2. Figure 7(a) shows the resulting SRS spectrum; Figure 7(b) shows the spectral profiles at 1 ns for the cases with and without bandwidth. Both profiles were quite narrow and occurred over a similar density range.

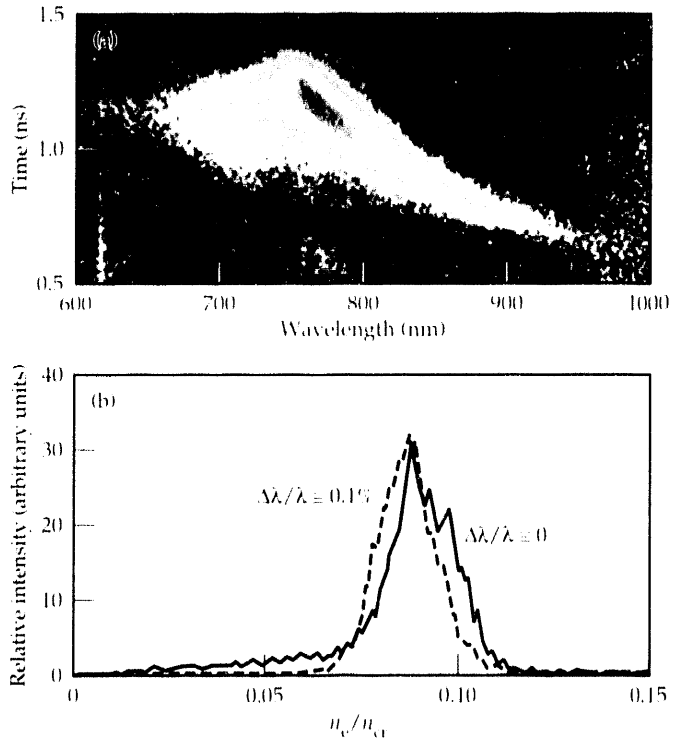

FIGURE 7. (a) Backscattered emission from SRS produced by a low-intensity interaction beam. (b) Emission vs electron density at 0.95 ns into the preformed pulse for case (a) and the high-intensity SSD case from Fig. 6(b).

Modeling

SRS and SBS are particular examples of parametric instabilities that grow provided the coupling parameter (the laser intensity in this case) is large enough. The laser must feed energy into the scattered light faster than it is lost by damping or convection of wave energy out of the region where the waves are resonantly coupled. These gain and loss rates for both SRS and SBS depend on the electron temperature, density, and their gradients in addition to the laser intensity and wavelength. SBS is also sensitive to the ion temperature and plasma flow velocity gradient.

As mentioned earlier, extensive LASNEX modeling of the hydrodynamics of these CH foils has shown the peak plasma electron density to be in agreement with the experimental data. Laser burnthrough times are also in agreement with experimental times. Given this agreement, we feel confident in using plasma parameters from the LASNEX simulations to calculate the linear gains and thresholds of SRS and SBS.

A few hundred picoseconds after the plasma becomes underdense ($n_e < n_{cr}$) to the heater beam, the plasma electron density assumes the generic shape of an isothermal-electron Gaussian expansion.[18] Although approximately constant in space, the electron temperature falls in time because the decreasing laser absorption heating cannot compensate for the hydrodynamic expansion cooling. The plasma flow in the direction normal to the initial target surface increases linearly with the magnitude of the distance from the peak density surface. In the long delay experiments, the electron temperature drops after burnthrough from 1.5 keV at 0.5 ns to 1.2 keV at 1.1 ns just before the interaction beam is turned on. In response to the better absorption of the 0.527-μm laser beam (as opposed to the 0.351-μm laser beam), the electron temperature increases within 0.1 ns to 2.1 keV after which it resumes a steady drop to 1.2 keV at 2 ns. When the interaction beam is turned on at 0.4 ns, the electron temperature rises to 3.2 keV at 0.5 ns, then falls to 1.3 keV by 1.5 ns. The ion temperature has a Gaussian shape with a profile similar to the electron density.

Analytical Modeling of the Plasma

Using the information on the plasma evolution provided by LASNEX, we find analytical approximations for the time and space dependent electron density and flow velocity. The peak electron density n_{ep} falls from 10^{21} cm^{-3} at 0.5 ns to 10^{20} cm^{-3} at 1.8 ns according to the equation

$$n_{ep}(t) = 10^{21}\exp\left[-(t-0.5)/0.56\ \mathrm{ns}\right] \quad . \tag{2}$$

For early times (data taken with 0.4-ns delay), the peak density is the same at 0.5 ns but it falls somewhat faster between 0.5 ns and 1.5 ns due to the presence of the interaction beam. The density profile n_e has the Gaussian shape

$$n_e(z,t) = n_{ep}(t)\exp\left(-z^2/2L_n^2\right) \quad , \tag{3}$$

with the characteristic density scalelength $L_n(t)$ = 500 µm $(t/1$ ns). The velocity V has the shape $V(z) = 10^8\,(z/L_v)$ cm/s with the velocity scalelength $L_v\,(t) \cong 650$ µm $(t/1$ ns). The scale-length parameters for the 0.4-ns delay case are not significantly different.

Strong flow velocity gradients in these exploding foil plasmas lead to a linear gain coefficient for SBS, also known as the Rosenbluth gain coefficient G_R, given as:

$$G_R = \frac{2\pi\gamma_0^2}{\left|\kappa' c V_{ga}\right|} \quad . \tag{4}$$

where $\kappa' = \partial\kappa/\partial z$, where the wave number mismatch $\kappa = k_0 - k_s - k_p$, and Vga is the group velocity of the IAW, and γ_0 is the homogeneous (no gradients and no damping) plasma growth rate

$$\gamma_0 = \left(\frac{1}{4}\right)\left(\frac{V_0}{V_E}\right)\left(\frac{\omega_{pe}}{\omega_0}\right)\sqrt{\omega_s\omega_a} \quad , \tag{5}$$

At the matching point of the three waves, we set $z = 0$, then we have $\kappa = 0$ and $k'\,V_{ga} \cong 2k_0\,|\,dV/dz\,|\,0$. The value of G_R at $z = 0$ can now be rewritten as

$$\begin{aligned} G_R &= \frac{2\pi^2}{8}\,\frac{V_0^2}{V_E^2}\,\frac{n_e}{n_{cr}}\left|\frac{C_s}{dV/dz}\right|\frac{1}{\lambda_0} \\ &= 300\,\frac{n_e}{n_{cr}}\,\frac{I_{15}\lambda_\mu}{T_{keV}^{1/2}}\sqrt{\frac{Z}{A}}\left(\frac{10^9\,\mathrm{s}^{-1}}{|dV/dz|}\right) \quad , \end{aligned} \tag{6}$$

where T_{KeV} is the electron temperature. In the 1.1-ns delay case, a peak laser intensity of 4×10^{15} W/cm^2 (I_{15} = 4) gives $G_R \cong 18$, and an average intensity of 2×10^{15} W/cm^2 gives $G_R \cong 9$ at 0.1 ns after the interaction pulse is turned on. The higher value for G_R implies substantial amplification over thermal noise such that reflectivity in excess of 10% is expected; the lower value implies less than 1% reflectivity. The high reflectivity measured in the experiment suggests that most of the observed SBS light is coming from the plasma region near the peak of the Airy spatial profile. For the 0.4-ns-delay case, a peak laser intensity of 4×10^{15} W/cm^2 gives $G_R \cong 21$ at 0.1 ns after turning on the interaction pulse. This value is similar to the 1.1-ns-delay gain coefficient. During the 0.1 ns in which the plasma is rapidly heating, a factor of two higher gain is possible so that the early-time reflectivity is expected to be substantially higher than the time-averaged. This change in the value of G_R during the first 0.1 ns of the interaction beam may partially explain the tendency of the SBS emission to consist of a bright burst followed by a rapid decrease in this emission. Seeding by IAW may also explain some of the transient strong SBS emission observed early in the interaction pulse which may be produced by the decay of electron plasma waves driven by SRS. The transient behavior of SRS-produced EPWs and their subsequent decay into an IAW and a secondary EPW has been observed in simulations.[19]

This description of the interaction (in terms of the vacuum laser characteristics) is too simple in regards to the relatively high ratio of plasma wave to thermal pressure. This ratio can be expressed as $V_0^2/V_E^2 = 4 \times 10^{-16}\,(I\lambda_\mu^2/T_{keV})$. On the spatial scale corresponding to the growth length of the SRS and SBS instabilities, the laser beam consists of speckles of FWHM width $f\lambda_0$, FWHM length $8f^2\lambda_0$ (where f is the full-beam f-number), and intensity peaks of two to ten times the local spatially averaged intensity. Thus, in the more intense speckles where $V_0^2 \cong V_e^2$, substantial modification of the local plasma density is expected.

A quantitative analysis of the depth of the density modulations produced by a combination of ponderomotive forces and electron pressure variations has been done with the use of a three-dimensional filamentation code.[20] Thermal forces with nonlocal thermal conduction were also included. The simulations were calculated with an average intensity of 2×10^{15} W/cm^2 and an electron temperature of 1.5 keV at initially uniform densities in the range between 0.05 to 0.2 n_{cr} of critical density for 0.527-µm laser light. At the lowest initial density, 0.05 n_{cr}, the laser beam intensity distribution changes very little in response to the filamentation process. However, the laser produces density holes as deep as 50% ($\delta n/n = 0.5$) within 10 ps after the laser is turned on. At the higher initial density of 0.2 n_{cr}, the plasma response produces a substantial increase in the fraction of laser energy at high intensity (i.e., the beam filaments and creates density holes of 100%). Simulations at the high initial density and the intensity at the peak of the Airy pattern (4×10^{15} W/cm) show that the strong plasma modification occurs over most of the plasma volume.

Simulations of three dimensional filamentation have also been done with an SSD model. At 0.2 n_{cr} and $I = 2 \times 10^{15}$ W/cm^2, the deepest modulations of the density are reduced from 100 to 20% and the intensity distribution of the laser beam energy does not change substantially (i.e., the filamentation process is stabilized for a bandwidth of 0.1%, which is roughly the value used in the experiments).

These simulation results suggest the following interpretation of the SRS spectra. Theoretically, the highest SRS gain should occur at the peak of the unmodulated density profile because the electron plasma wave damping is smallest there and because $\kappa' = 0$ (since $\partial\omega_{pe}^2/\partial z = 0$). However, when filamentation occurs in these experiments, the high laser intensities develop in holes of varying depth where $\kappa' = 0$ still applies. The width of the SRS spectrum then is a measure of the range of densities produced by the filaments at the peak of the spatially averaged density. In addition, electron Landau damping is strong inside the low-density filaments where $k_{EPW}\lambda_{De} > 0.5$. Thus, significant Compton scattering from high laser intensities ($>10^{16}$ W/cm^2) within filaments can also contribute to broadening the SRS spectrum. SSD produces a narrower spectrum at the average density maximum because the range of densities with $\kappa \sim 0$ is reduced.

The effect of filamentation on stimulated Brillouin backscattering is more difficult to assess than SRS because the time scales in which filaments form and SBS grow are similar. Our estimates for the growth of SBS with a uniform intensity beam in a one-dimensional plasma show that, except for a short time of about 0.1 ns, the SBS reflectivity is modest. In an RPP beam, however, 4% of the beam energy has intensity in excess of five times the average, which could account for the levels observed if most of this energy were backscattered. SBS phase matching is relatively insensitive to density gradients so the filamentation process should have little dephasing effect. Since the plasma moves laterally in filamentation, little modulation of the flow parallel to k_0 is produced. The expulsion of plasma from the high intensity regions reduces the growth rate of SBS and produces hydrodynamic (Doppler) frequency shifts. This effect might explain the peculiar early time spectral blue shifts. A quantitative assessment of this awaits further modeling.

Conclusions

We continue to study the effects of beam smoothing on parametric instabilities and its potential to control their growth. The study addresses the experimental application of present Nova beam smoothing techniques, as well as the modeling of instabilities in the presence of laser intensity distributions characterized by beam smoothing. Our experiments have shown that, although RPP and SSD can reduce the reflectivity of SBS at low electron density, it has little effect early in time when the maximum electron density is relatively high. Beam smoothing eliminates any observable SRS light from the shoulders of the electron density distribution, limiting the SRS growth to the density maxima. Future experiments will study the effect of speckle size, by varying the aperture of the focusing lens and will study the spatial distribution of emission within the focal spot. Beam smoothing may permit control of the growth of parametric instabilities and offers the possibility of performing experiments in which the distribution of laser intensity can be controlled.

Notes and References

1. W. L. Kruer, *The Physics of Laser Plasma Interactions* (Addison-Wesley, New York, 1988).
2. H. A. Baldis, E. M. Campbell, and W. L. Kruer, in *Handbook of Plasma Physics, Vol. 3: Physics of Laser Plasma* (North Holland, 1991), Ch. 9.
3. M. A. Henesian, S. N. Dixit, H. T. Powell, C. E. Thompson, P. J. Wegner, and T. L. Weiland, *XVIII International Quantum Electronics Conference*, 14–19 June 1992, Vienna, Austria, **TuE3** (in publication).
4. H. T. Powell, S. N. Dixit, and M. A. Henesian, "Beam Smoothing Capability on the Nova Laser," *ICF Quarterly Report* **1** (1) 28, Lawrence Livermore National Laboratory, Livermore, CA, UCRL-LR-105821-91-1 (1990).
5. D. Pesme, *Rapport annuel du GRECO 1987*, CNRS–Ecole Polytechnique, France, p. 27.
6. R. L. Berger, *Phys. Rev. Lett.* **65**, 1207 (1990).
7. Y. Kato, K. Mima, N. Miyanaga, S. Arinaga, Y. Kitagawa, M. Nakatsuka, and C. Yamanaka, *Phys. Rev. Lett.*, **53**, 1057 (1984).
8. R. H. Lehmberg and S. P. Obenschain, *Opt. Comm.*, **46**, 27 (1983).
9. S. Skupsky, R. W. Short, T. Kessler, R. S. Craxton, S. Letzring, and J. M. Soures, *J. Appl. Phys.* **66**, 3456 (1989).
10. A. N. Mostovich *et al.*, *Phys. Rev. Lett.* **59**, 1193 (1987).
11. S. P. Obenshain *et al.*, *Phys. Rev. Lett.* **62**, 768 (1989).
12. T. Jalinaud, S. Baton, C. Labaune, and H. A. Baldis, *Rapport Scientifique 1990 du Laboratoire pour L'Utilisation des Lasers Intenses*, CNRS–Ecole Polytechnique, France, p. 56.
13. S. Baton, C. Labaune, T. Jalinaud, and H. A. Baldis, "Experimental Study of Filamentation in High-Intensity Laser-Plasma Interaction," *21st European Conference on Laser Interaction with Matter* (October 1991), Warsaw, Poland.
14. C. Labaune, S. D. Baton, T. Jalinaud, H. A. Baldis, and D. Pesme, *Phys. Fluids B* **4**, 2224 (1992)
15. O. Willi, T. Ashard-rad, S. Coe, and A. Giulietti, *Phys. Fluids B* **2**, 1318 (1990).
16. S. N. Dixit et. al., "Random phase plates for beam smoothing on the Nova laser," *Appl. Opt.* **32**, 2543–2554 (1993).
17. Dixit et. al., "Large Aperture Sol-Gel Random Phase Plates for Beam Smoothing," *ICF Quarterly Report* **3** (2) 96, Lawrence Livermore National Laboratory, Livermore, CA, UCRL-LR-105821-93-2 (1993).
18. R. A. London and M. D. Rosen, *Phys. Fluids* **29**, 3813 (1986).
19. T. Kolber, W. Rozmus, V. Y. Tikhonchuk, H. A. Baldis, and K. Estabrook, "Brillouin Scattering From Fluctuations Produced by Stimulated Raman Scattering," *Proc. SPIE* **1860** (1993).
20. R. L. Berger et al., *Phys. Fluids B* **5**, 1 (1993).

FACILITY REPORT, APRIL–JUNE 1993

G. Hermes
Nova Operations Group
Nova Experiments Group
Laser Science Group

During this quarter, Nova Operations fired a total of 323 system shots, resulting in 393 experiments. These experiments were distributed among ICF experiments, Defense Sciences experiments, X-ray Laser experiments, Laser Sciences, and facility maintenance shots.

The installation of the new incident beam diagnostic (IBD) packages was completed this quarter. The IBDs will provide us with a temporal and spatial sampling of the incident beam, as well as 1, 2, and 3ω energy measurements. The diagnostics will be activated and calibrated next quarter.

The target plain imager replacement (TPIR) was completed and the system was activated in late June. The TPIR is used to view the reticule and beams at chamber center for target alignment. It is located off-axis and is designed to be more reliable and quicker to use than the present target plain imager (TPI). The TPIR is being used for routine operations during its shakedown period. After the TPIR has been completely tested, the present on-axis TPI will be removed to allow use of this premium location for other target diagnostics. We plan to remove the present TPI in early August.

Beam simultaneity was measured this quarter and showed a pre-existing 20-ps RMS variation between beam arrival times on target. After corrections were made to several of the beamlines, measurements showed a residual variation in timing offsets of 7 ps RMS, measurable with an accurate of ±4 ps RMS.

Installation of the small aperture (65-cm) debris shields was completed. These small debris shields replace the large (80-cm) version previously used. They are easier to handle during maintenance and cost less to replace than the larger version. As a part of our routine maintenance, we will clean and recoat five small debris shields per week to improve and maintain the precision power balance on the target.

PUBLICATIONS

A

Abare, A. C., Keane, C. J., Lee, R. W., Da Silva, L. B., Crane, J. K., Perry, M. D., and Falcone, R. W., *Analysis of Neon Soft X-Ray Spectra from Short Pulse Laser Produced Plasmas*, Lawrence Livermore National Laboratory, Livermore, CA, UCRL-JC-113498 (1993). Prepared for *Proc. 93 SPIE Short Pulse High Intensity Lasers and Applications II.*

Ateyan, B. B., and Williams, E. A., *Strong Coupling Limit of Stimulated Brillouin Sidescattering in Inhomogeneous Plasmas*, Lawrence Livermore National Laboratory, Livermore, CA, UCRL-JC-111155 ABS Rev. 1 (1993). Prepared for *23rd Annual Anomalous Absorption Conference*, Wintergreen, VA, June 21–25, 1993.

Amendt, P., Eder, D. C., Rosen, M. D., and London, R. A., *Plasma Dispersion in Ultra-Short Pulse X-Ray Lasers*, Lawrence Livermore National Laboratory, Livermore, CA, UCRL-JC-109987 (1993); *Phys. Rev. Lett. A* **47**, 2 (1993).

Amendt, P., London, R., and Strauss, M., *Optimization Study of X-Ray Laser Coherence in Ni-Like Ta*, Lawrence Livermore National Laboratory, Livermore, CA, UCRL-JC-110084 (1993). Prepared for *Third International Colloquium on X-Ray Lasers*, Schliersee, Germany, May 18–22, 1992.

Amendt, P., London, R., and Strauss, M., *Optimization of Single-Stage X-Ray Laser Coherence*, Lawrence Livermore National Laboratory, Livermore, CA, UCRL-JC-110900 (1993). Submitted to *Am. Phys. Soc.*

Amendt, P., Powers, L., Hauer, A., and Suter, L., *Time Resolved Symmetry Modeling in Nova Hohlraums*, Lawrence Livermore National Laboratory, Livermore, CA, UCRL-JC-113470 ABS Rev. 1 (1993). Prepared for *23rd Annual Anomalous Absorption Conference*, Wintergreen, VA, June 21–25, 1993.

Atherton, L. J., Payne, S. A., and Brandle, C. D., *Oxide and Fluoride Laser Crystals*, Lawrence Livermore National Laboratory, Livermore, CA, UCRL-JC-112688 (1993). Submitted to *Annual Review of Materials Science.*

B

Back, C. A., and Kauffman, R. L., *Characterization of Plasmas by Microdot Spectroscopy*, Lawrence Livermore National Laboratory, Livermore, CA, UCRL-MI-113820 (1993). Prepared for *Women's Technical Conference*, May 6–7, 1993.

Baldis, H., Montogomery, D., Batha, S., Labaune, D., Moody, J., Estabrook, K., Berger, K., and Kruer, W., *Parametric Instabilities in Large Nonuniform Laser Plasmas*, Lawrence Livermore National Laboratory, Livermore, CA, UCRL-JC-111546 (1993). Prepared for *1992 International Conference on Plasma Physics*, Innsbruck, Austria, June 29–July 3, 1992.

Baldis, H. A., Labaune, C., Jalinaud, T., Baton, S., Moody, J. D., Estabrook, K., and Dixit, S., *Temporal Evolution of Backscattered SBS Light from Preformed Plasmas*, Lawrence Livermore National Laboratory, Livermore, CA, UCRL-JC-113491 ABS (1993). Prepared for *23rd Annual Anomalous Absorption Conference*, Wintergreen, VA, June 21–25, 1993.

Baldis, H. A., Moody, J. D., Batha, S. H., Labaune, D., Montgomery, D. S., Estabrook, K. G., Berger, R. L., Williams, E. A., and Kruer, W. L., *Laser-Plasma Instabilities and Coherence Control*, Lawrence Livermore National Laboratory, Livermore, CA, UCRL-JC-110329 (1993). Prepared for *International Atomic Energy Agency*, Wurzberg, Germany, September 30–October 7, 1992.

Baldis, H. A., Villeneuve, D. M., Labaune, D., Enright, G. D., La Fontaine, B., Baton, S., Mounaix, P., Pesme, D., and Casanova, M., *Stimulated Brillouin Scattering in Picosecond Time Scales: Experiments and Modeling*, Lawrence Livermore National Laboratory, Livermore, CA, UCRL-JC-113224 (1993). Submitted to *J. Phys. Fluid.*

Barnard, J. J., Caporaso, G. J., Eylon, S., and Yu, S. S., *One Dimensional Simulations of Transients in Heavy Ion Injectors*, Lawrence Livermore National Laboratory, Livermore, CA, UCRL-JC-112343 (1993). Prepared for *1993 Particle Accelerator Conference*, Washington, DC, May 17–21, 1993.

Barnard, J. J., Caporaso, G. J., Sharp, W. M., and Chen, Y-J, *Research in the Heavy Ion Fusion Project*, Lawrence Livermore National Laboratory, Livermore, CA, UCRL-MI-113950 (1993). Prepared for UC Davis, Livermore, CA, April 14, 1993.

Barnard, J. J., Deadrick, F., Griffith, L. V., Grote, D. P., Friedman, A., Kirbie, H. C., Neil, V. K., Newton, M. A., and Paul, A. C., *Recirculating Induction Accelerators As Drivers for Heavy Ion Fusion*, Lawrence Livermore National Laboratory, Livermore, CA, UCRL-JC-111379 (1993). Submitted to *Phys. Fluids B.*

Barnard, J. J., Miller, J., and Haber, I., *Emittance Growth in Displaced, Space-Charge-Dominated Beams with Energy Spread*, Lawrence Livermore National Laboratory, Livermore, CA, UCRL-JC-112340 (1993). Prepared for *1993 Particle Accelerator Conference*, Washington, DC, May 17–21, 1993.

Bauer, B. S., Drake, R. P., Sleaford, B., Mizuno, K., Baker, K. L., Estabrook, K., Afeyan, B. B., Rubenchik, A. M., and Labaune, C., *Langmuir Turbulence Generated by the Ion Acoustic Decay Instability*, Lawrence Livermore National Laboratory, Livermore, CA, UCRL-JC-111276 ABS Rev. 1 (1993). Prepared for *23rd Annual Anomalous Absorption Conference*, Wintergreen, VA, June 21–25, 1993.

Bell, P. M., Kilkenny, J. D., Bradley, D. K., Hanks, R. L., and Landen, O. L., *Electrical Characteristics of Short Pulse Gated Microchannel Plate Detectors*, Lawrence Livermore National Laboratory, Livermore, CA, UCRL-JC-109796 (1993). Prepared for *Ninth Topical Conference on High Temperature Plasma Diagnostics*, Santa Fe, NM, March 15–19, 1992.

Berger, R., Lasinski, B., Langdon, A., Williams, E., Kaiser, T., and Cohen, B., *Theory and Three Dimensional Simulation of Light Filamentation in Laser Produced Plesmas*, Lawrence Livermore National Laboratory, Livermore, CA, UCRL-JC-111590 (1993). Submitted to *Phys. Fluids*.

Berger, R. L., Lasinski, B. F., Langdon, A. B., Kaiser, T., Cohen, B. I., and Williams, E. A., *Fluid Simulations of Laser Beam Smoothing Effects on Stimulated Raman and Brillouin Backscattering Including Filamentation*, Lawrence Livermore National Laboratory, Livermore, CA, UCRL-JC-113923 ABS and UCRL-MI-113923 (1993). Prepared for *23rd Annual Anomalous Absorption Conference*, Wintergreen, VA, June 21–25, 1993.

Bernat, T. P., Mapoles, E. R., Hoffer, J., and Collins, G., *Surface Characteristics of Solid Cryogenic Fuel in Laser Fusion Targets*, Lawrence Livermore National Laboratory, Livermore, CA, UCRL-MI-113050 (1993). Prepared for *22nd European Conference on Laser Matter Interaction*, Paris, France, May 10–14, 1993.

Brusasco, R., Ferguson, S. W., and Stever, R., *Impedance Power Effects on Plasma Polymer Surface Finish Using a Helical Resonator Discharge*, Lawrence Livermore National Laboratory, Livermore, CA, UCRL-JC-112361 and UCRL-MI-112361(1993). Prepared for *American Chemical Society National Meeting*, Denver, CO, March 29–April 3, 1993.

Busby, L., *Review of the LASNEX Batch Job System*, Lawrence Livermore National Laboratory, Livermore, CA, UCRL-ID-112691 (1993).

C

Caird, J. A., Murray, J. R., and Powell, H. T., *Precision Nova Project at LLNL*, Lawrence Livermore National Laboratory, Livermore, CA, UCRL-MI-113057 (1993). Prepared for *22nd European Conference on Laser Matter Interaction*, Paris, France, May 10–14, 1993.

Callahan, D. A., Langdon, A. B., Haber, I., and Friedman, A., *Longitudinal Beam Dynamics for Heavy Ion Fusion*, Lawrence Livermore National Laboratory, Livermore, CA, UCRL-JC-112341 (1993). Prepared for *1993 Particle Accelerator Conference*, Washington, DC, May 17–21, 1993.

Caporaso, G. J., *Novel High Gradient Accelerators*, Lawrence Livermore National Laboratory, Livermore, CA, UCRL-MI-113709 (1993). Prepared for Office of Fusion Energy, DOE, March 16, 1993.

Caporaso, G. J., and Barnard, J. J., *Analysis of Beam Loading in Electrostatic Columns*, Lawrence Livermore National Laboratory, Livermore, CA, UCRL-JC-112342 (1993). Prepared for *1993 Particle Accelerator Conference*. Washington, DC, May 17–21, 1993.

Chow, R., Falabella, S., Stolz, C. J., Rainer, F., Loomis, G. E., and Kozlowski, M. R., *Absorption and Damage Thresholds of Low Defect Hafnia Deposited with Activated Oxygen*, Lawrence Livermore National Laboratory, Livermore, CA, UCRL-JC-111458 (1993). Prepared for *Laser Induced Damage in Optical Materials*, Boulder, CO, October 28–30, 1992.

Collins, G. W., Maienschein, J. L., Fearon, E. M., Tsugawa, R. T., Mapoles, E. R., Souers, P. C., Gaines, J. R., and Fedders, P. A., *Atomic ESR Linewidths in Solid Hydrogen*, Lawrence Livermore National Laboratory, Livermore, CA, UCRL-JC-109911 (1993); *Phys. Rev. B* 1, 3.

Cook, R. C., Bernat, T. P., McEachern, R., Letts, S. A., Collins, G., and Overturf, G. E., *Production and Characterization of ICF Capsules*, Lawrence Livermore National Laboratory, Livermore, CA, UCRL-JC-109891 (1993). Prepared for *Fourteenth International Conference on Plasma Physics and Controlled Nuclear Fusion Research*, Wurzburg, Germany, September 30–October 7, 1992.

Coverdale, C. A., Darrow, C. B., Joshi, D., Mori, W. B., and Perry, M. D., *High Intensity Irradiation of Long Scalelength, Underdense Plasmas with the LLNL 10-TW Glass Laser*, Lawrence Livermore National Laboratory, Livermore, CA, UCRL-JC-113738 ABS (1993). Prepared for *23rd Annual Anomalous Absorption Conference*, Wintergreen, VA, June 21–25, 1993.

D

Da Silva, L. B., Trebes, J. E., Anderson, E., Mrowka, S., Balhorn, R., Attwood, D. T., Barbee, T. W., Brase, J., and Corzett, M., *X-Ray Laser Imaging Microscopy of Rat Sperm Nuclei*, Lawrence Livermore National Laboratory, Livermore, CA, UCRL-JC-110876 (1993). Submitted to *J. Science*.

Da Silva, L. B., Trebes, J. E., Koch, J. A., MacGowan, B. J., Mrowka, S., Matthews, D. L., Barbee, T. W., Balhorn, R., and Gary, J., *Progress in Imaging Microscopy with X-Ray Lasers At LLNL*, Lawrence Livermore National Laboratory, Livermore, CA, UCRL-JC-111296 REP (1991). Prepared for *Third International Colloquium on X-Ray Lasers*, Schliersee, Germany, May 18–22, 1992.

Da Silva, L. B., Trebes, J. E., Koch, J. A., MacGowan, B. J., Mrowka, S., Matthews, D., Barbee, T. W., Balhorn, R., and Gary, J., *Imaging Microscopy with X-Ray Lasers at LLNL*, Lawrence Livermore National Laboratory, Livermore, CA, UCRL-JC-111801 (1993). Prepared for *SPIE Technical Conference on Soft X-Ray Microscopy*, San Diego, CA, July 19–24, 1992.

Deadrick, F. J., *ILSE Diagnostics WBS 1.2.9*, Lawrence Livermore National Laboratory, Livermore, CA, UCRL-MI-114035 (1993). Prepared for ILSE Accelerator Construction Project Review, Berkeley, CA, May 4–6, 1993.

Deadrick, F. J., and Lionberger, C. A., *ILSE Supervisory Controls and Data Acquisition—WBS 1.2.10*, Lawrence Livermore National Laboratory, Livermore, CA, UCRL-MI-114034 (1993). Prepared for ILSE Accelerator Construction Project Review, Berkeley, CA, May 4–6, 1993.

Deloach, L. D., Payne, S. A., Smith, L. K., Krupke, W. F., Chai, B. H. T., Kway, W. L., and Tassano, J. B., *Laser and Spectroscopic Properties of Yb-Doped Apatite Crystals*, Lawrence Livermore National Laboratory, Livermore, CA, UCRL-JC-113407 (1993). Prepared for OSA *Advanced Solid-State Lasers, 8th Topical Meeting*, New Orleans, LA, February 1–3, 1993.

Devine, G., Letts, S., Brusasco, R., and Cook, R., *State-of-the-Art Plasma Polymerization Coater for ICF Targets*, Lawrence Livermore National Laboratory, Livermore, CA, UCRL-JC-112360 and UCRL-MI-112360 (1993). Prepared for *American Chemical Society National Meeting*, Denver, CO, March 29–April 3, 1993.

Ditmire, T., and Perry, M. D., *Terawatt Cr:LiSrAlF$_6$ Laser System*, Lawrence Livermore National Laboratory, Livermore, CA, UCRL-JC-111942 (1993); *J. Optics Letts.* **18**, 6 (1993).

Dixit, S., Lawson, J., Powell, H., and Manes, K., *Design and Fabrication of Continuous Contour Phase Plates for Beam Smoothing*, Lawrence Livermore National Laboratory, Livermore, CA, UCRL-MI-112268 (1993). Prepared for *CLEO/QELS '93*, Baltimore, MA, May 4, 1993.

Dixit, S., Lawson, J., Nugent, K., Powell, H., and Manes, K., *Designing Continuous Contour Phase Plates for Beam Smoothing*, Lawrence Livermore National Laboratory, Livermore, CA, UCRL-MI-112270 (1993). Prepared for *Optical Design for Photonics*, Palm Springs, CA, March 23, 1993.

Dixit, S. N., Feit, M., D., and Donnat, P., *Exact Solution for Light Propagation Through a Nonlinear Kerr Medium with Two-Photon, Absorption*, Lawrence Livermore National Laboratory, Livermore, CA, UCRL-JC-111924 (1993). Submitted to *Optics Communications*.

Dixit, S. N., Thomas, I. M., Woods, B. W., Morgan, A. J., Henesian, M. A., Wegner, P. J., and Powell, H. T., *Random Phase Plates for Beam Smoothing on the Nova Lasers*, Lawrence Livermore National Laboratory, Livermore, CA, UCRL-JC-109577 (1993); *App. Opt.*, **32** (14) 2543–2554 (1993).

Dixit, S. N., Thomas, I. M., Wegner, P. J., Henesian, M. A., Woods, B. W., and Powell, H. T., *Large Aperture Sol-Gel, Random Phase Plates for Beam Smoothing on the Nova Laser*, Lawrence Livermore National Laboratory, Livermore, CA, UCRL-JC-111299 (1993). Submitted to *App. Opt.*

Dubois, P. F., and Busby, L., *Portable, Powerful Fortran Programs*, Lawrence Livermore National Laboratory, Livermore, CA, UCRL-JC-112254 (1993). Submitted to *Computers and Physics*.

E

Ellis R., *Design of Multi-Function Alignment Microscope for Laser Fusion Experiments*, Lawrence Livermore National Laboratory, Livermore, CA, UCRL-JC-114561 ABS (1993). Prepared for *Design Engineering Conference & Show*, Chicago, IL, March 14–17, 1993.

F

Faris, G. W., Jusinski, L. E., and Hickman, A. P., *High Resolution Stimulated Brillouin Gain Spectroscopy in Glasses and Crystals*, Lawrence Livermore National Laboratory, Livermore, CA, UCRL-CR-103295-92 (1993). Submitted to *J. Opt. Soc. Am. B*.

Friedman, A., *LLNL HIF Project Status and Plans*, Lawrence Livermore National Laboratory, Livermore, CA, UCRL-MI-113588 (1993). Prepared for Office of Fusion Energy, DOE, March 16, 1993.

Friedman, A., *LLNL HIF Project Perspective Presented at LLNL IFE Workshop*, Lawrence Livermore National Laboratory, Livermore, CA, UCRL-MI-113828 (1993). Prepared for *LLNL IFE Workshop*, Livermore, CA, March 31– April 1, 1993.

Friedman, A., and Bangerter, R. O., *Inertial Fusion Energy (IFE) Using Heavy Ion Drivers*, Lawrence Livermore National Laboratory, Livermore, CA, UCRL-JC-111595 (1993). Submitted to *Physics News in 1992*.

Friedman, A., Barnard, J. J., Chen, Y-J., Caporaso, G. J., Callahan, D. A., Deford, J. F., Fawley, W. N., Grote, D. P., and Haber, I., *Simulation of Heavy Ion Fusion Beams*, Lawrence Livermore National Laboratory, Livermore, CA, UCRL-JC-110193 (1993).

Prepared for the *IAEA Technical Committee Meeting on Advances in Simulation and Modeling of Thermonuclear Plasmas*, Montreal, Canada, June 15–18, 1992.

Friedman A., Barnard, J. J., Sharp, W. M., Newton, M. A., Caporaso, G. J., and Yu, S. S., *Development Paths for Recirculating Induction Accelerators*, Lawrence Livermore National Laboratory, Livermore, CA, UCRL-MI-114212 (1993). Prepared for *Integrated Test Facility Study Meeting*, LLNL, Livermore, CA, April 23, 1993.

Friedman, A., Callahan, D. A., Langdon, A. B., Haber, I., Grote, D. P., and Lund, S. M., *What We've Learned from 3-D and R, Z Intense Beam Simulations Using the WARP Code*, Lawrence Livermore National Laboratory, Livermore, CA, UCRL-JC-113283 and UCRL-MI-113283 (1993). Prepared for *International Symposium on Heavy Ion Inertial Fusion*, Frascati, Italy, May 25–28, 1993.

G

Glinsky, M. E., Kruer, W. L., Hammer, J. H., and Tabak, M., *Simple Model of Supra-Thermal Electron Transport*, Lawrence Livermore National Laboratory, Livermore, CA, UCRL-MI-111436 (1993). Prepared for *Second Topical Meeting, Short Wavelength V: Physics with Intense Laser Pulses*, San Diego, CA, March 29–31, 1993.

Grote, D. P., Friedman, A., and Haber, I., *Three Dimensional PIC Simulation of Heavy Ion Fusion Beams: Recent Improvements to and Applications of WARP*, Lawrence Livermore National Laboratory, Livermore, CA, UCRL-JC-112508 (1993). Prepared for *1993 Particle Accelerator Conference*, Washington, DC, May 17–21, 1993.

H

Haan, S. W., *Design of Targets for the National Ignition Facility*, Lawrence Livermore National Laboratory, Livermore, CA, UCRL-JC-113480 ABS (1993). Prepared for *1993 Topical Conference*, Monterey, CA, April 25–29, 1993.

Hammel, B. A., Griswold, D., Remington, B. A., Perry, T., Landen, O. L., Kilkenny, J. D., and Pasha, R. A., *X-Ray, Radiographic Measurements of Radiation Driven Shock and Interface Motion in Solid Density Material*, Lawrence Livermore National Laboratory, Livermore, CA, UCRL-JC-111933 (1993). Submitted to *Appl. Phys. Lett.*

Hammel, B. A., Keane, C. J., Ress, D. R., Landen, O. L., Kilkenny, J. D., Bell, P., Pasha, R., and Wallace, R. J., *X-Ray Imaging and Spectroscopic Measurements of Implosions*, Lawrence Livermore National Laboratory, Livermore, CA, UCRL-JC-109892 (1993). Prepared for *Fourteenth International Conference on Plasma Physics and Controlled Nuclear Fusion Research*, Wurzburg, Germany, September 30–October 7, 1992.

Hammel, B. A., Keane, C. J., Lee, R. W., Kilkenny, J. D., Kania, D. R., and Pasha, R., *X-Ray Spectroscopic Measurements of High Densities and Temperatures from Indirectly Driven, ICF Capsules*, Lawrence Livermore National Laboratory, Livermore, CA, UCRL-JC-111184 (1993); *Phys. Rev. Lett.* **70**, 9 (1993).

Hammer, J., Glinsky, M., Wilks, S., Tabak, M., Kruer, W., and Woodworth, J., *Short Pulse Lasers for Generation of Fields Exceeding 100 Mg*, Lawrence Livermore National Laboratory, Livermore, CA, UCRL-JC-111540 (1993). Prepared for *Sixth International Conference on Megagauss Magnetic Field Generation & Related Topics*, Albuquerque, NM, November 8–11, 1992.

Hinkel-Lipsker, D. E., Williams, E. A., and Berger, R. L., *Temporal Evolution of Stimulated Brillouin Backscatter*, Lawrence Livermore National Laboratory, Livermore, CA, UCRL-JC-113925 ABS (1993). Prepared for *23rd Annual Anomalous Absorption Conference*, Wintergreen, VA, June 21–25, 1993.

Ho, D. D-M., and Crandall, K. R., *Dependence of Quadrupole Pole Tip Fields on Beam Parameters and Design of Nondispersive Optics for Final-Focusing Systems for High-Current Heavy-Ion Beams*, Lawrence Livermore National Laboratory, Livermore, CA, UCRL-JC-109998 Rev. 1 (1993). Prepared for *1993 Particle Accelerator Conference*, Washington, DC, May 17–21, 1993.

Ho, D. D-M., Lindl, J. D., and Tabak, M., *Radiation Converter Physics and a Methodology for Obtaining the Upper Limit for Gain for Heavy-Ion Fusion*, Lawrence Livermore National Laboratory, Livermore, CA, UCRL-MI-111176 (1993). Prepared for *International Symposium on Heavy Ion Inertial Fusion*, Frascati, Italy, May 25–28, 1993.

Holdener, F. R., Platt, E. A., Gelinas, R. J., Frank, D. N., Erlandson, A. C., Jancaitis, K. S., Larson, D. W., and Sinz, K. H., *Calculations of Dynamic Stresses in the Envelopes of Pulsed Xe Flashlamps*, Lawrence Livermore National Laboratory, Livermore, CA, UCRL-JC-110021 (1993). Prepared for *SPIE 1992 Symposium on Optical Applied Science and Engineering*, San Diego, CA, July 19–24, 1992.

House, P. A., *HYLIFE-II Reactor Chamber Mechanical Design Update*, Lawrence Livermore National Laboratory, Livermore, CA, UCRL-ID-109429 (1993).

I

Izumitani, T., and Payne, S. A., *Luminescence of Sm^{2+}-Doped Fluoride Glasses*, Lawrence Livermore National Laboratory, Livermore, CA, UCRL-JC-110879 (1993); *J. Luminescence*, **54** (1993).

K

Kaiser, T., Lasinski, B., Langdon, A., Cohen, B., Berger, R., and Williams, E., *Stabilization of Filament by Beam Smoothing Using Spectral Dispersion and Frequency Splitting*, Lawrence Livermore National Laboratory, Livermore, CA, UCRL-JC-114601 ABS (1993). Prepared for *American Physical Society Division of Plasma Physics*, St Louis, MO, November 1–5, 1993.

Kauffman, R. L., Montgomery, D. S., Lebreton, J. P., Bocher, J. L., Suter, L. J., and Babonneau, D., *X-Ray Production from Thin Au Foils on Octal*, Lawrence Livermore National Laboratory, Livermore, CA, UCRL-JC-113943 ABS (1993). Prepared for *23rd Annual Anomalous Absorption Conference*, Wintergreen, VA, June 21–25, 1993.

Keane, C. J., Dittrich, T. R., Levedahl, W. K., Lee, R. W., Hammel, B. A., Scott, H. A., Langer, S. H., and Suter, L. J., *Spectroscopy Based Mix Diagnostics for High Growth Factor Nova Implosion Experiments*, Lawrence Livermore National Laboratory, Livermore, CA, UCRL-JC-113921 ABS (1993). Prepared for *23rd Annual Anomalous Absorption Conference*, Wintergreen, VA, June 21–25, 1993.

Keane, C. J., Hammel, B. A., Kania, D. R., and Osterheld, A. L., *Diagnosis of Electron Temperature and Density in High Temperature Plasmas Using L-Shell Xenon Emission Spectroscopy*, Lawrence Livermore National Laboratory, Livermore, CA, UCRL-JC-112993 (1993). Submitted to *Phys. Rev. Lett.*

Keane, C. J., Hammel, B. A., Lee, R. W., Kilkenny, J. D., Kania, D. R., Osterheld, A. L., Suter, L. J., Mancini, R. C., and Hooper, C. F., *X-Ray Spectroscopy of High Energy Density Inertial Confinement Fusion Plasmas*, Lawrence Livermore National Laboratory, Livermore, CA, UCRL-JC-113160 (1993). Submitted to *Phys. Fluids B*.

Kilkenny, J. D., Munro, D. H., Remington, B. A., Glendinning, S. G., Haan, S. W., Weber, S., Wallace, R. J., Knauer, J., and Verdon, C., *Experimental Determination of the Hydrodynamic Instability Growth Rates in Indirect and Direct Drive ICF*, Lawrence Livermore National Laboratory, Livermore, CA, UCRL-MI-110277 Rev. 1 (1993). Prepared for *22nd European Conference on Laser Matter Interaction*, Paris, France, May 10–14, 1993.

Klem, D. E., Darrow, D., Lane, S., and Perry, M. D., *Interaction of Intense Femtosecond Laser Pulses with Solid Targets*, Lawrence Livermore National Laboratory, Livermore, CA, UCRL-JC-112630 (1993). Prepared for *Second Topical Meeting, Short Wavelength V: Physics with Intense Laser Pulses*, San Diego, CA, March 29–31, 1993.

Klem, D. E., Darrow, D., Perry, M. D., and Lane, S., *Absorption and X-Ray Measurements from Ultra Intense Laser Plasma Interactions*, Lawrence Livermore National Laboratory, Livermore, CA, UCRL-JC-112950 (1993). Prepared for

SPIE Optical Engineering/Laser Conference '93, Los Angeles, CA, January 16–23, 1993.

Koch, J. A., MacGowan, B. J., Mrowka, S., Matthews, D. L., Da Silva, L. B., Underwood, J. H., and Batson, P. J., *Selenium X-Ray Laser Line Profile Measurements*, Lawrence Livermore National Laboratory, Livermore, CA, UCRL-JC-110974 (1991). Prepared for *Third International Colloquium on X-Ray Lasers*, Schliersee, Germany, May 18–22, 1992.

Koch, J. A., MacGowan, B. J., London, R. A., Matthews, D. L., Da Silva, L. B., Lee, R. W., Mrowka, S., Underwood, J. H., and Batson, P. J., *Experimental Measurements of Selenium X-Ray Laser Spectral Line Profiles*, Lawrence Livermore National Laboratory, Livermore, CA, UCRL-JC-113290 (1993). Prepared for *Lasers '92*, Houston, TX, December 6–11, 1992.

Kolber, T., Rozmus, W., Estabrook, K., Baldis, H. A., and Tikhonchuk, V. T., *Brillouin Scattering from Fluctuations Produced by Stimulated Raman Scattering*, Lawrence Livermore National Laboratory, Livermore, CA, UCRL-JC-112700 (1993). Prepared for *SPIE Optical Engineering/Laser Conference '93*, Los Angeles, CA, January 16–23, 1993.

Kozlowski, M. R., Chow, R., and Thomas, I. M., *Optical Coatings for High Power Laser Applications*, Lawrence Livermore National Laboratory, Livermore, CA, UCRL-JC-111796 (1993), *Handbook of Laser Science and Technology: Supplemental 2: Optical Method*.

Kozlowski, M. R., Deford, J. F., and Staggs, M. C., *Laser Damage Susceptibility of Nodular Defects in Dielectric Mirror Coatings: AFM Measurements and Electric Field Modeling*, Lawrence Livermore National Laboratory, Livermore, CA, UCRL-JC-112981 (1993). Prepared for *Second International Conference on Laser Ablation*, Knoxville, TN, April 19–22, 1993.

Kruer, W. L., and Wilks, S. C., *Kinetic Simulations of Ultra Intense Laser Plasma Interactions*, Lawrence Livermore National Laboratory, Livermore, CA, UCRL-JC-110953 (1993). Prepared for *1992 International Conference on Plasma Physics*, Innsbruck, Austria, June 29–July 3, 1992.

Kruer, W. L., and Wilks, S. C., *Introduction to Ultra Intense Laser Plasma Interactions*, Lawrence Livermore National Laboratory, Livermore, CA, UCRL-JC-112676 (1993). Submitted to *Advances in Plasma Physics*.

L

Langer, S., *Effects of Radiation Transport on Line Ratios Used As Temperature and Density Diagnostic*, Lawrence Livermore National Laboratory, Livermore, CA, UCRL-JC-110695 (1993). Prepared for *22nd Annual Anomalous Absorption Conference*, Wintergreen, VA, July 12–17, 1992.

Langer, S. H., and Ze, F., *Comparison of LASNEX Modeling to SXRC Data on Spot Spreading in Conversion Efficiency Experiments*, Lawrence Livermore National Laboratory, Livermore, CA, UCRL-JC-113920 ABS (1993). Prepared for *23rd Annual Anomalous Absorption Conference*, Wintergreen, VA, June 21–25, 1993.

Lasinski, B. F., Kaiser, T. B., Kruer, W. L., Cohen, B. I., Berger, R. L., Langdon, A. B., Still, C. H., Wilks, S. C., and Williams, E. A., *Effect of Beam Smoothing on Filamentation*, Lawrence Livermore National Laboratory, Livermore, CA, UCRL-JC-110759 ABS Rev. 1 (1993). Prepared for *23rd Annual Anomalous Absorption Conference*, Wintergreen, VA, June 21–25, 1993.

Lasinski, B. F., Kaiser, T. B., Kruer, W. L., Cohen, B. I., Berger, R. L., Langdon, A. B., Wilks, S. C., and Williams, E. A., *Filamentation in Current and Future Experiments*, Lawrence Livermore National Laboratory, Livermore, CA, UCRL-JC-113477 ABS (1993). Prepared for *'93 Topical Conference, Physics of Radiatively Driven ICF Targets*, Monterey, CA, April 26–29, 1993.

Lasinski, B. F., Kaiser, T. B., Kruer, W. L., Cohen, B. I., Berger, R. L., Langdon, A. B., Still, C. H., Wilks, S. C., and Williams, E. A., *Effect of Beam Smoothing on Filamentation*, Lawrence Livermore National Laboratory, Livermore, CA, UCRL-MI-110759 Rev. 2 (1993). Prepared for *23rd Annual Anomalous Absorption Conference*, Wintergreen, VA, June 21–25, 1993.

Lee, E. D., *Waste Disposal of HYLIFE-II Structure: Issues and Assessment*, Lawrence Livermore National Laboratory, Livermore, CA, UCRL-ID-111598 (1993).

Lee, E. D., *Waste Disposal Assessment of HYLIFE-II Structure*, Lawrence Livermore National Laboratory, Livermore, CA, UCRL-JC-111598 (1993). Submitted to *Fusion Technology*.

Letts, S. A., Collins, G., McEachern, R., Cook, R., Fearon, E., and Welch, P., *Effect of Process Parameters on the Surface Finish of Plasma Polymers*, Lawrence Livermore National Laboratory, Livermore, CA, UCRL-JC-112379 and UCRL-MI-112379 (1993). Prepared for *American Chemical Society National Meeting*, Denver, CO, March 29–April 3, 1993.

Logan, B. G., *Potential Economics of Multi-Unit IFE Plants for Hydrogen Fuel Production*, Lawrence Livermore National Laboratory, Livermore, CA, UCRL-JC-114082 ABS (1993). Prepared for *IEEE 15th Symposium on Fusion Engineering*, Hyannis Port, MS, October 11–15, 1993.

London, R. A., Trebes, J. E., and Jacobsen, C. J., *Role of X-Ray Induced Damage in Biological Micro-Imaging*, Lawrence Livermore National Laboratory, Livermore, CA, UCRL-JC-109590 (1993). Prepared for*SPIE Optical Engineering Laser Conference '93*, Los Angeles, CA, January 16–23, 1993.

M

MacGowan, B. J., *X-Ray Lasers as Sources for X-Ray Microscopy*, Lawrence Livermore National Laboratory, Livermore, CA, UCRL-JC-111802 (1993). Prepared for *SPIE 1992 Technical Conference on Soft X-Ray Microscopy*, San Diego, CA, July 19–24, 1992.

MacGowan, B. J., *Advances in VUV and X-Ray Sources*, Lawrence Livermore National Laboratory, Livermore, CA, UCRL-MI-113486 (1993). Prepared for *OSA Topical Conference on Short Wavelength Coherent Radiation Generation*, San Diego, CA, March 30, 1993.

MacGowan, B. J., *Development of Robust Multilayer Optics for Use in High-Peak-Power, Radiation Environments*, Lawrence Livermore National Laboratory, Livermore, CA, UCRL-MI-113814 (1993). Prepared for *1993 MRS Spring Meeting*, April 12–16, 1993, San Francisco, CA.

MacGowan, B. J., Mrowka, S., Eder, D. C., Da Silva, L. B., Barbee, T. W., Koch, J. A., Pan, L. S., Turner, J. A., and Underwood, J. H., *Investigation of Damage to Multilayer Optics in X-Ray Laser Cavities: W/C, WRe/C, W/C, Stainless Steel/C and Cr$_3$C$_2$/C Mirrors*, Lawrence Livermore National Laboratory, Livermore, CA, UCRL-JC-112299 (1993). Submitted to *J. X-Ray Sci. & Tech.*

MacGowan, B. J., Mrowka, S., Eder, D. C., Da Silva, L. B., Barbee, T. W., Koch, J. A., and Underwood, J. H., *Problems in the Implementations of X-Ray Optics with X-Ray Lasers*, Lawrence Livermore National Laboratory, Livermore, CA, UCRL-JC-111376 REP (1991). Prepared for *Third International Colloquium on X-Ray Lasers*, Schliersee, Germany, May 18–22, 1992.

Matthews, D., *Livermore X-Ray Laser Program*, Lawrence Livermore National Laboratory, Livermore, CA, UCRL-JC-110706 (1991). Prepared for *Third International Colloquium on X-Ray Lasers*, Schliersee, Germany, May 18–22, 1992.

Matthews, D. L., Balhorn, R., Hackel, L., Eder, D., Da Silva, L. B., Koch, J., Libby, S., London R., and MacGowan, B., *Development of Compact X-Ray Lasers and Their Applications*, Lawrence Livermore National Laboratory, Livermore, CA, UCRL-JC-109573 ABS Rev. 1 (1993). Prepared for *1993 IEEE International Conference on Plasma Science*, Vancouver, British Columbia, Canada, June 7–9, 1993.

Mattingly, S., and Moir, R., *Method to Prevent Ejecta from Damaging the Compact Torus Accelerator Driver of an Inertial Fusion Energy Power Plant*, Lawrence Livermore National Laboratory, Livermore, CA, UCRL-ID-112569 1993).

McEwan, T. E., *Micropower Ultra Wideband, Radar*, Lawrence Livermore National Laboratory, Livermore, CA, UCRL-JC-113207 (1993). Submitted to *R&D Magazine*.

McEwan, T. E., and Kilkenny, J. D., *Single Shot Transient Digitizer*, Lawrence Livermore National Laboratory, Livermore, CA, UCRL-JC-113208 (1993). Submitted to *R&D Magazine*.

Moir, R. W., *HYLIFE-II: A Recent Design Study of a Heavy-Ion Driven Inertial Fusion Energy (IFE) Power Plant*, Lawrence Livermore National Laboratory, Livermore, CA, UCRL-JC-113504 ABS (1993). Prepared for *International Symposium on Heavy Ion Inertial Fusion*, Frascati, Italy, May 25–28, 1993.

Montgomery, D. S., Baldis, H. A., Berger, R. L., Afeyan, B. B., Moody, J. D., Estabrook, K. G., Lasinski, B. F., Williams, E. A., and Wilks, S. C., *Modification of SRS by Beam Smoothing in Large Scale Length Plasmas*, Lawrence Livermore National Laboratory, Livermore, CA, UCRL-JC-113944 ABS (1993). Prepared for *23rd Annual Anomalous Absorption Conference*, Wintergreen, VA, June 21–25, 1993.

More, R. M., *Relativistic Semiclassical Atomic Transition Rates*, Lawrence Livermore National Laboratory, Livermore, CA, UCRL-JC-113719 (1993). Submitted to *J. Quantitative Spectroscopy & Radiative Transfer*.

N

Newton, M. A., *Longitudinal Control and Voltage Correction*, Lawrence Livermore National Laboratory, Livermore, CA, UCRL-MI-114033 (1993). Prepared for ILSE Accelerator Construction Project Review, Berkeley, CA, May 4–6, 1993.

Newton, M. A., Cravey, W. R., Ollis, C. W., Kirbie, H. C., and Hawkins, S. A., *Development of FET Switched Induction Accelerator Cells for Heavy-Ion Fusion Recirculators*, Lawrence Livermore National Laboratory, Livermore, CA, UCRL-JC-112375 (1993). Prepared for *1993 Particle Accelerator Conference*, Washington, DC, May 17–21, 1993.

Newton, M. A., and Kirbie, H. C., *Technology Development for Recirculating Heavy Ion Accelerators*, Lawrence Livermore National Laboratory, Livermore, CA, UCRL-JC-113282 (1993). Prepared for *International Symposium on Heavy Ion Inertial Fusion*, Frascati, Italy, May 25–28, 1993.

Newton, M. A., and Kirbie, H. C., *Technology Development for Recirculating Heavy-Ion Accelerators*, Lawrence Livermore National Laboratory, Livermore, CA, UCRL-MI-113282 (1993). Prepared for *1993 Particle Accelerator Conference*, Washington, DC, May 17–21, 1993.

P

Payne, A. N., *System Modeling for the Longitudinal Beam Dynamics Control Problem in Heavy-Ion Induction Accelerators*, Lawrence Livermore National Laboratory, Livermore, CA, UCRL-JC-112378 (1993). Prepared for *1993 Particle Accelerator Conference*, Washington, DC, May 17–21, 1993.

Payne, S. A., *Physics and Performance of Novel Diode-Pumped Solid-State Lasers*, Lawrence Livermore National Laboratory, Livermore, CA, UCRL-MI-114534 (1993). Prepared for *Laser Optics '93*, St. Petersburg, Russia, June 21–25, 1993.

Payne, S. A., Chai, B. H. T., Smith, L. K., DeLoach, L. D., Kway, W. L., Lutts, G., Peale, R., Zhang, X. X., and Wilke, G. D., *New High Cross Section Laser Crystal: Neodymium-Doped Strontium Fluorovanadate*, Lawrence Livermore National Laboratory, Livermore, CA, UCRL-MI-113610 (1993). Prepared for *CLEO '93*, Baltimore, MD, May 2–7, 1993.

Payne, S. A., and Krupke, W. F., *Design and Development of New Laser Materials*, Lawrence Livermore National Laboratory, Livermore, CA, UCRL-JC-113928 ABS (1993). Prepared for *ICL '93*, Storrs, CT, August 9–13, 1993.

Pennington, D. M., Henesian, M. A., Thompson, C. E., Powell, H. T., Dixit, S. N., Webb, M. S., and Weiland, T. L., *Third Harmonic Frequency Conversion and Beam Smoothing with Bandwidth on the Nova Lasers,* Lawrence Livermore National Laboratory, Livermore, CA, UCRL-MI-113934 (1993). Prepared for *CLEO '93*, Baltimore, MD, May 2–7, 1993.

Perry, M. D., and Crane, J. K., *Polarization Effects in High Order Sum and Difference Frequency Generation,* Lawrence Livermore National Laboratory, Livermore, CA, UCRL-JC-112631 (1993). Submitted to *Phys. Rev. Lett.*

Powell, H. T., *Beam Smoothing Development for Nova and the NIF*, Lawrence Livermore National Laboratory, Livermore, CA, UCRL-MI-113237 Rev. 1 (1993). Prepared for Centre D'etudes, Limeil-Valenton, France, May 17, 1993.

Powers L., Berger R., Hinkel-Lipsker, D., Harte, J., Estabrook, K., Lasinski B., Munro, D., Procassini R., and Rambo, P., *Modeling of Large Scale Length Plasma Designs for Measuring Stimulated Brillouin Scattering on Nova*, Lawrence Livermore National Laboratory, Livermore, CA, UCRL-JC-113739 ABS (1993). Prepared for *23rd Annual Anomalous Absorption Conference*, Wintergreen, VA, June 21–25, 1993.

Powers L., Suter, L., Hauer, A., Ress, D., and Amendt, P., *Modeling of Capsule Symmetry Measurements in Nova Hohlraums*, Lawrence Livermore National Laboratory, Livermore, CA, UCRL-MI-112990 (1993). Prepared for *22nd European Conference on Laser Matter Interaction*, Paris, France, May 10–14, 1993.

R

Remington, B. and Dimonte, G., *Comprehensive Program for Investigating Hydrodynamic Mix*, Lawrence Livermore National Laboratory, Livermore, CA, UCRL-MI-113933 (1993). Prepared for U.S. DOE, Germantown, MD, May 5, 1993.

Ress, D., Da Silva, L. B., Procassini, R., Lehr, D., Mrowka, S., London R., and Trebes, J. E., *A Soft X-Ray Moire Deflectometer for Laser Plasma Density Measurements*, Lawrence Livermore National Laboratory, Livermore, CA, UCRL-MI-114219 (1993). Prepared for *22nd European Conference on Laser Matter Interaction*, Paris, France, May 10–14, 1993.

Ress, D., Lerche, R. A., Bradley, D. K., Bell, P. M., Ellis, R. J., and Lane, S. M., *Coded Aperture Imaging at the Nova Laser Facility*, Lawrence Livermore National Laboratory, Livermore, CA, UCRL-MI-114218 (1993). Prepared for *22nd European Conference on Laser Matter Interaction*, Paris, France, May 10–14, 1993.

Rotter, M., D., Erlandson, A. C., and McCracken, R. W., *Analytic Model for Calculating Pump Induced Wavefront Distortions in Laser Slabs*, Lawrence Livermore National Laboratory, Livermore, CA, UCRL-JC-111193 (1993). Prepared for *Society for Optical and Quantum Electronics*, McLean, VA

S

Sharp, W. M., Barnard, J. J., and Yu, S. S., *Steering Algorithms for a Heavy Ion Recirculating Accelerator*, Lawrence Livermore National Laboratory, Livermore, CA, UCRL-JC-110868 (1993). Prepared for *Ninth International Conference on High-Power Particle Beams*, Washington, DC, May 25–29, 1992.

Sharp, W. M., Callahan, D. A., Fessenden, T. J., Langdon, A. B., and Barnard, J. J., *Correction of Longitudinal Errors in Accelerators for Heavy-Ion Fusion*, Lawrence Livermore National Laboratory, Livermore, CA, UCRL-MI-112377 (1993). Prepared for *1993 Particle Accelerator Conference*, Washington, DC, May 17–21, 1993.

Smith, L. K., Payne, S. A., Kway, W. L., Deloach, L. D., Tassano, J. B., and Krupke, W. F., *Optical and Physical Properties of the LiSrAlF$_6$:Cr Laser Crystal*, Lawrence Livermore National Laboratory, Livermore, CA, UCRL-JC-111851 (1993). Prepared for OSA *Advanced Solid-State Lasers Eighth Topical Meeting*, New Orleans, LA, February 1–3, 1993.

Suter, L. J., Kauffman, R. L., and Cray, M., (LANL) *X-Ray Conversion in Preformed Plasmas*, Lawrence Livermore National Laboratory, Livermore, CA, UCRL-JC-107601 (1993). Prepared for *21st European Conference on Laser Interaction with Matter*, Warsaw, Poland, October 21–25, 1991.

Suter, L. J., Powers, L. V., Hauer A. A., Ress, D. B., and Amendt, P. A., *Analysis of Nova Hohlraum Symmetry Experiments*, Lawrence Livermore National Laboratory, Livermore, CA, UCRL-JC-113922 ABS (1993). Prepared for *23rd Annual Anomalous Absorption Conference*, Wintergreen, VA, June 21–25, 1993.

Swatloski, T. L., *Graphical User Interface for AMOS and POISSON*, Lawrence Livermore National Laboratory, Livermore, CA, UCRL-MI-112263 (1993). Prepared for *CAP '93*, Pleasanton, CA, February 22–26, 1993.

T

Thomas, I. M., *Optical Coating Fabrication*, Lawrence Livermore National Laboratory, Livermore, CA, UCRL-JC-111948 (1993). Submitted to *Sol-Gel Optics*.

Tietbohl, G. L., and Patel, C. S., *Seismic Upgrade of the Nova Capacitor Bank*, Lawrence Livermore National Laboratory, Livermore, CA, UCRL-ID-113500 (1993).

Trebes, J., *Spatial Coherence of Soft X-Ray Lasers*, Lawrence Livermore National Laboratory, Livermore, CA, UCRL-JC-111392 (1991). Prepared for *Third International Colloquium on X-Ray Lasers*, Schliersee, Germany, May 18–22, 1992.

W

Webb, M. S., *Temperature Sensitivity of KDP for Phase-Matched Frequency Conversion of 1 µm Laser Light*, Lawrence Livermore National Laboratory, Livermore, CA, UCRL-JC-113170 (1993). Submitted to *IEEE J. Quantum Electron.*

Wilcox, R. B., Behrendt, W., Van Wonterghem, B. M., Speck, D. R., and Browning, D. F., *Fusion Pulse Generator System Design Using Waveguide Optics*, Lawrence Livermore National Laboratory, Livermore, CA, UCRL-JC-113746 ABS (1993). Prepared for OSA *Annual Meeting/ILS '93*, Toronto, Ontario, Canada, October 3–8, 1993.

Wilks, S. C., *Simulations of Ultra-Intense Laser Plasma Interactions*, Lawrence Livermore National Laboratory, Livermore, CA, UCRL-JC-112253 (1993). Submitted to *Phys. Fluids*.

Wilks, S. C., Berger, R. L., Lasinski, B. F., Langdon, A. B., Kruer, W. L., Montgomery, D., Cohen, B. I., and Williams, E. A., *Three-Dimensional Filamentation and Whole Beam Self-Focusing of Laser Light Including Nonlinear Hydrodynamics*, Lawrence Livermore National Laboratory, Livermore, CA, UCRL-JC-113926 ABS (1993). Prepared for *23rd Annual Anomalous Absorption Conference*, Wintergreen, VA, June 21–25, 1993.

Wilks, S. C., Kruer, W. L., and Mori, W. B., *Kinetic Simulations of Ultra-Intense Laser Plasma Interactions and a Novel Method of Generating Odd Harmonics*, Lawrence Livermore National Laboratory, Livermore, CA, UCRL-JC-113163 (1993). Prepared for *SPIE Optical Engineering/Laser Conference '93*, Los Angeles, CA, January 16–23, 1993.

Wilks, S. C., Kruer, W. L., and Mori, W. B., *Relativistic Filamentation and Absorption of Ultra-High Intensity Laser Light Near the Critical Surface*, Lawrence Livermore National Laboratory, Livermore, CA, UCRL-JC-113924 ABS (1993). Prepared for *23rd Annual Anomalous Absorption Conference*, Wintergreen, VA, June 21–25, 1993.

Wilks, S. C., and Kruer, W. L., *Ultra-Intense, Short Pulse Laser-Plasma Interactions in the Presence of a Critical Surface*. Lawrence Livermore National Laboratory, Livermore, CA, UCRL-MI-113708 (1993). Prepared for *'93 Short Wavelength V: Physics W/Intense Laser Pulses, 2nd Topical Mtg.*, March 29–April 1, 1993, San Diego, CA.

END

DATE
FILMED
12/20/93